

# Important Notice

This copy may be used only for the purposes of research and private study, and any use of the copy for a purpose other than research or private study may require the authorization of the copyright owner of the work in question. Responsibility regarding questions of copyright that may arise in the use of this copy is assumed by the recipient.

THE UNIVERSITY OF CALGARY

Near-Surface Seismic Characterization using  
Three-Component Buried Geophones

by

Dan Cieslewicz

A THESIS

SUBMITTED TO THE FACULTY OF GRADUATE STUDIES  
IN PARTIAL FULFILLMENT OF THE REQUIREMENTS FOR THE  
DEGREE OF MASTER OF SCIENCE

DEPARTMENT OF GEOLOGY AND GEOPHYSICS

CALGARY, ALBERTA

JANUARY, 1999

© Dan Cieslewicz 1999

THE UNIVERSITY OF CALGARY  
FACULTY OF GRADUATE STUDIES

The undersigned certify that they have read, and recommended to the Faculty of Graduate Studies for acceptance, a thesis entitled “Near-Surface Seismic Characterization using Three-Component Buried Geophones” submitted by Dan Cieslewicz in partial fulfillment of the requirements for the degree of Master of Science.

---

Supervisor, Dr. Don C. Lawton, Department of Geology and Geophysics

---

Dr. Larry R. Lines, Department of Geology and Geophysics

---

Dr. Gary F. Margrave, Department of Geology and Geophysics

---

Dr. Michael Slawinski, Department of Mechanical Engineering

---

Date

### **Abstract**

Two seismic field experiments were performed to determine whether shear wave attenuation in the near surface is responsible for the significant converted-wave bandwidth reduction observed in most multi-component land surveys. The experiments consisted of three-component geophones buried to depths of about 6, 12 and 18m that recorded data during the shooting of a 2-D seismic line. A control geophone was also placed on the surface. The geophones did not detect any systematic difference in the bandwidth of converted-wave reflections between the different geophone depths and the surface. It is concluded that the majority of attenuation in the converted wave occurs below a depth of 18 meters. The buried geophone data were also used to determine the depth of the water table using interval  $V_p/V_s$  ratios, to demonstrate that the near-surface impedance gradient amplifies ascending reflections, and to indirectly infer the occurrence of a receiver ghost. A basic interpretation is also presented.

### **Acknowledgements**

I am indebted to many people who provided assistance through the various phases of this research. On the acquisition side, I thank our sponsor who provided access and resources that made the Chin Coulee experiment possible, and Eric Gallant who performed most of the associated field operations. Mr. Gallant also modified 63 geophones for the Blackfoot III experiment so that they could be retrieved afterwards. The field surveying expertise of Brian Hoffe helped resolve some geometry issues with regard to the Blackfoot data. I thank the CREWES staff for their support especially during the processing and analysis stages, including Henry Bland, Colin Potter, Han-Xing Lu and Darren Foltinek. Enlightening conversations from other graduate students, including Jitendra Gulati and Tricia Nichols, enhanced my understanding of certain issues unique to buried geophone data. Dr. Gary Margrave provided invaluable theoretical and practical input, and helpful suggestions, for which I am grateful. I am also grateful to the sponsors of CREWES for their support in this research. I also thank my supervisor Don Lawton, for the guidance, direction and input he provided throughout the duration of this thesis.

## TABLE OF CONTENTS

|  |           |
|--|-----------|
| Approval Page .....  | ii        |
| Abstract .....   | iii       |
| Acknowledgements .....   | iv        |
| Table of Contents .....  | v         |
| List of Figures.....   | vii       |
| List of Tables.....  | viii      |
| <br>   |           |
| <b>CHAPTER 1: INTRODUCTION.....</b>                            | <b>1</b>  |
| <b>1.1. Methods and Objectives.....</b>                        | <b>2</b>  |
| 1.1.1. Attenuation Investigation .....                         | 3         |
| 1.1.2. Vertical Interval Velocities.....                       | 3         |
| 1.1.3. Seismic Repeatability .....                             | 3         |
| 1.1.4. Interpretation .....                                    | 4         |
| 1.1.5. Numerical Modeling of Receiver Notching .....           | 4         |
| <b>1.2. Techniques and Software.....</b>                       | <b>5</b>  |
| <b>1.3. Literature Review .....</b>                            | <b>5</b>  |
| <br>   |           |
| <b>CHAPTER 2: CHIN COULEE BURIED GEOPHONE EXPERIMENT .....</b> | <b>7</b>  |
| <b>2.1. Geometry and Acquisition .....</b>                     | <b>7</b>  |
| <b>2.2. Processing .....</b>                                   | <b>8</b>  |
| <b>2.3. Traveltime Analysis .....</b>                          | <b>9</b>  |
| <b>2.4. Frequency Analysis.....</b>                            | <b>10</b> |
| 2.4.1. Raw Data .....  | 10        |
| 2.4.2. Bandpass Filtered Data.....                             | 14        |
| 2.4.3. f-k Filtered Data .....                                 | 14        |
| <b>2.5. Mode leakage and receiver re-orientation.....</b>      | <b>16</b> |
| <b>2.6. Vertical Interval Velocities .....</b>                 | <b>17</b> |
| <br>   |           |
| <b>CHAPTER 3: BLACKFOOT III BURIED GEOPHONE EXPERIMENT ...</b> | <b>23</b> |
| <b>3.1. Introduction.....</b>                                  | <b>23</b> |
| <b>3.2. Location .....</b>                                     | <b>23</b> |
| <b>3.3. Geometry and Acquisition .....</b>                     | <b>24</b> |
| <b>3.4. Processing .....</b>                                   | <b>26</b> |
| 3.4.1. Vertical Channel.....                                   | 26        |
| 3.4.2. Horizontal Channels.....                                | 29        |
| <b>3.4.2.1. P-S Asymptotic Binning.....</b>                    | <b>30</b> |
| <b>3.4.2.2. Mode Leakage and Receiver Re-orientation .....</b> | <b>31</b> |
| <b>3.4.2.3. Calculation of Receiver Statics .....</b>          | <b>33</b> |
| <b>3.4.2.4. Radial Channel Processed Sections .....</b>        | <b>36</b> |
| <b>3.5. Frequency Analysis.....</b>                            | <b>37</b> |
| 3.5.1. Vertical Channel.....                                   | 38        |
| 3.5.2. Radial Channel .....                                    | 40        |
| <b>3.6. Vertical Interval Velocities .....</b>                 | <b>42</b> |
| 3.6.1. P-Wave Velocities.....                                  | 42        |
| 3.6.2. S-Wave Velocities .....                                 | 45        |

|   |           |
|---|-----------|
|   | 6         |
| 3.6.3. <i>V<sub>p</sub>/V<sub>s</sub></i> Analysis .....              | 49        |
| <b>3.7. Similarity of Processed Sections .....</b>                    | <b>50</b> |
| 3.7.1. Trace Differences .....  | 50        |
| 3.7.2. Cross-correlations.....  | 52        |
| <b>3.7.2.1. Vertical Channel.....</b>                                 | <b>52</b> |
| <b>3.7.2.2. Radial Channel.....</b>                                   | <b>55</b> |
| 3.7.3. Mean Square Difference.....                                    | 57        |
| 3.7.4. Synopsis.....  | 59        |
| <br>  |           |
| <b>CHAPTER 4: NUMERICAL MODELING OF RECEIVER NOTCHING .</b>           | <b>60</b> |
| <b>4.1. Receiver Notch Theory .....</b>                               | <b>60</b> |
| <b>4.2. Simulations .....</b>   | <b>61</b> |
| 4.2.1. Design of the Model Near Surface .....                         | 61        |
| 4.2.2. Construction of Model Source Wavelet .....                     | 61        |
| 4.2.3. Numerical Simulation of Propagating Wavelet.....               | 62        |
| <b>4.2.3.1. Example .....</b>   | <b>63</b> |
| 4.2.4. Receiver Notching.....   | 65        |
| <b>4.2.4.1. Comparison to Blackfoot III Data.....</b>                 | <b>69</b> |
| 4.2.5. Wavelet Interference Effects on Amplitude .....                | 72        |
| 4.2.6. Near-Surface Impedance Effects on Amplitude.....               | 73        |
| <b>4.2.6.1. Comparison to Blackfoot III Data.....</b>                 | <b>74</b> |
| <br>  |           |
| <b>CHAPTER 5: BLACKFOOT III INTERPRETATION .....</b>                  | <b>77</b> |
| 5.1. Geology and Depositional Environment of the Mannville Group..... | 77        |
| 5.2. Generation of Synthetic Seismograms from Well Log Data.....      | 81        |
| 5.3. Log Splicing.....  | 82        |
| 5.4. Channel and Regional Synthetic Ties .....                        | 82        |
| <br>  |           |
| <b>CHAPTER 6: CONCLUSIONS AND RECOMMENDATIONS .....</b>               | <b>86</b> |
| <br>  |           |
| <b>CHAPTER 7: REFERENCES .....</b>                                    | <b>90</b> |

## LIST OF FIGURES

|  |    |
|--|----|
| Figure 1.1. Frequency spectra hydrophone data.....   | 5  |
| Figure 2.1. Location of Chin Coulee buried geophone experiment .....                       | 7  |
| Figure 2.2. Group 2, raw data.....   | 11 |
| Figure 2.3. Group 1 high-passed common receiver gathers .....                              | 12 |
| Figure 2.4. Frequency spectra of raw data.....   | 13 |
| Figure 2.5. Frequency spectra of high-passed data.....                                     | 15 |
| Figure 2.6. Performance of f-k filter on radial channel data .....                         | 16 |
| Figure 2.7. Frequency spectra of f-k data.....   | 17 |
| Figure 2.8. Compressional-wave reflections for all depths.....                             | 18 |
| Figure 2.9. Correlograms for the 18m to surface vertical channel.....                      | 19 |
| Figure 2.10. Lag times of cross-correlation maximum values .....                           | 20 |
| Figure 2.11. <i>P</i> - and <i>S</i> -wave interval velocities and $V_p/V_s$ .....         | 21 |
| Figure 3.1. Location of the Blackfoot III buried geophone experiment.....                  | 23 |
| Figure 3.2. Blackfoot III buried geophone experiment survey geometry.....                  | 24 |
| Figure 3.3. Geophone fitted with a sand spike and aircraft cable .....                     | 25 |
| Figure 3.4. Actual buried geophone depths below surface .....                              | 26 |
| Figure 3.5. Vertical and radial channel fold.....  | 27 |
| Figure 3.6. Surface and 6m geophone <i>P-P</i> processed sections. ....                    | 28 |
| Figure 3.7. 12 and 18m geophone <i>P-P</i> processed sections .....                        | 29 |
| Figure 3.8. Pre-rotated common receiver gathers for a buried geophone .....                | 32 |
| Figure 3.9. Rotated common receiver gathers for a buried geophone.....                     | 33 |
| Figure 3.10. Near-surface <i>S</i> - and <i>P</i> -wave thickness.....                     | 34 |
| Figure 3.11. Receiver hand statics.....  | 35 |
| Figure 3.12. Surface and 6m geophone <i>P-S</i> processed sections.....                    | 36 |
| Figure 3.13. 12m and 18m geophone <i>P-S</i> processed sections.....                       | 37 |
| Figure 3.14. Frequency analysis of <i>P-P</i> reflections.....                             | 39 |
| Figure 3.15. Frequency analysis of <i>P-S</i> reflections. ....                            | 41 |
| Figure 3.16. <i>P</i> -wave interval velocities between buried and surface geophones. .... | 43 |
| Figure 3.17. Receiver elevations above sea level.....                                      | 44 |
| Figure 3.18. Elevation difference between adjacent geophone stations.....                  | 45 |
| Figure 3.19. Near-surface <i>P</i> -wave velocity model. ....                              | 46 |
| Figure 3.20. Near-surface shear wave velocities for buried-to-buried intervals .....       | 47 |
| Figure 3.21. Near-surface shear wave velocities for surface-to-buried intervals. ....      | 48 |
| Figure 3.22. Vertical interval $V_p/V_s$ for surface to buried intervals.....              | 49 |
| Figure 3.23. Trace difference of 6m and 12m geophone <i>P-P</i> sections .....             | 51 |
| Figure 3.24. Trace difference of 0m and 6m geophone <i>P-S</i> sections.....               | 52 |
| Figure 3.25. <i>P-P</i> section cross-correlation analysis .....                           | 54 |
| Figure 3.26. Average cross-correlation values of the <i>P-P</i> sections.....              | 54 |
| Figure 3.27. <i>P-S</i> section correlation analysis .....                                 | 56 |
| Figure 3.28. Average peak cross-correlation values of the <i>P-S</i> sections.....         | 56 |
| Figure 3.29. <i>P-P</i> section comparison using mean square difference.....               | 58 |
| Figure 3.30. <i>P-S</i> section comparison using mean square difference.....               | 59 |
| Figure 4.1. Time and frequency domain plots of a 30Hz Ricker wavelet.....                  | 62 |

|  |    |
|--|----|
| Figure 4.2. Simulated incident, reflected and total wave fields (time domain).....                     | 64 |
| Figure 4.3. Simulated incident, reflected and total wave fields (depth domain).....                    | 65 |
| Figure 4.4. Receiver notching for a $V=900\text{m/s}$ medium .....                                     | 66 |
| Figure 4.5. Receiver notching for a $V_0=300\text{m/s}$ , $V_{18}=3100\text{m/s}$ linear $V(z)$ .....  | 67 |
| Figure 4.6. Receiver notching for a $V_0=300\text{m/s}$ , $V_{18}=2200\text{m/s}$ linear $V(z)$ .....  | 68 |
| Figure 4.7. Receiver notching for a $V_0=300\text{m/s}$ , $V_{18}=900\text{m/s}$ linear $V(z)$ . ..... | 68 |
| Figure 4.8. Receiver notching for a $V_0=150\text{m/s}$ , $V_{18}=400\text{m/s}$ linear $V(z)$ . ..... | 69 |
| Figure 4.9. Frequency spectra of $P$ - $S$ reflections.....  | 71 |
| Figure 4.10. Frequency spectra of $P$ - $P$ reflections .....  | 72 |
| Figure 4.11. Total wavefield maximum amplitude for four velocity gradients .....                       | 73 |
| Figure 4.12. Actual and modeled amplitudes for $P$ -wave reflections .....                             | 75 |
| Figure 4.13. Actual and modeled amplitudes for $S$ -wave reflections.....                              | 76 |
| Figure 5.1. Location of well logs used to interpret the Blackfoot III line .....                       | 78 |
| Figure 5.2. Stratigraphic cross-section of the Mannville Group .....                                   | 79 |
| Figure 5.3. Channel and regional $P$ - $P$ synthetic ties .....  | 83 |
| Figure 5.4. Channel and regional $P$ - $S$ synthetic ties.....   | 84 |

## LIST OF TABLES

|  |    |
|--|----|
| Table 2.1. Chin Coulee buried geophone depths.....                                     | 8  |
| Table 2.2. Processing steps for the Chin Coulee buried geophone data.....              | 9  |
| Table 3.1. Processing steps for the Blackfoot III buried geophone $P$ - $P$ data. .... | 27 |
| Table 3.2. Processing steps for the Blackfoot III buried geophone $P$ - $S$ data. .... | 30 |

## CHAPTER 1

### INTRODUCTION

A significant issue in multi-component seismology is that the bandwidth of converted-wave\* reflections is usually much narrower than compressional-wave reflections. The narrower bandwidth causes converted-wave seismic sections to have poorer vertical resolution than conventional compressional-wave sections. Given the added acquisition and processing costs associated with multi-component surveys, and the usefulness of the technique as a powerful lithology discriminator, any feasible method of improving the bandwidth of the converted wave would be of great interest.

Compressional- and converted-wave reflections are physically identical on the descending raypath, but on the ascending raypath, converted waves travel as shear energy while compressional-wave reflections remain compressional energy. The narrower bandwidth observed in converted-wave reflections therefore implies that converted waves experience greater attenuation on the ascending raypath, while they are travelling as shear wave energy. There are a number of reasons why this should be so. At a fundamental level, because shear waves travel at roughly half the velocity of compressional waves, they complete about twice as many cycles as compressional waves of the same frequency going an equivalent distance. As attenuation is a measure of energy loss per cycle, this results in inherently greater attenuation for shear waves, assuming  $Q_s=Q_p$ . However, laboratory measurements (Toksöz *et al.*, 1978) indicate that brine- and water-saturated rock is generally more attenuative to shear waves than to compressional waves (*i.e.*,  $Q_s < Q_p$ ), so shear waves may be expected to attenuate more quickly than compressional waves than can be accounted for by their slower velocity alone.

The available evidence from vertical seismic profile (VSP) data demonstrates that the converted- and compressional-wave reflections have approximately the same bandwidth in bedrock (e.g. Geis *et al.*, 1990). This results in converted-wave VSP sections having superior temporal resolution than compressional wave VSP sections, as

---

\*For the purposes of discussion here, the term "converted wave" refers to a compressional wave that has reflected as a shear wave, also denoted as 'P-S'.

shear waves have a shorter wavelength than compressional waves of the same frequency owing to their lower velocity. The converted-wave attenuation observed in surface data, then, must occur at some point after the converted wave leaves the bedrock and before it reaches the surface. As an important difference between a VSP and a surface survey is the influence of the near-surface layer for the upwards path, significant shear-wave attenuation may be occurring in the near surface. Laboratory measurements indicate that unconsolidated overburden can be very attenuative to shear waves (Kudo and Shima, 1970), so near-surface shear-wave attenuation provides a possible explanation for the comparatively poor bandwidth seen in converted-wave seismic data recorded at the surface.

This thesis describes and analyzes results from two experiments designed to test the hypothesis that the relative reduction in bandwidth seen in converted-wave reflections with respect to compressional-wave reflections is due to significant shear-wave attenuation in the near-surface layer. The data were also used to better characterize the seismic velocity and impedance of the near surface, and investigate receiver notching. These results will help to improve our understanding of how the important but often underappreciated near-surface layer affects multi-component seismic data.

### **1.1. Methods and Objectives**

Data for this thesis is from two buried geophone experiments that were conducted separately. Each experiment was composed of groups of multi-component geophones buried to depths of about 6, 12 and 18 meters, plus one on the surface. The first experiment was from Chin Coulee in southern Alberta (Figure 2.1), and was composed of three such buried geophone groups. It was essentially a trial run for the second, Blackfoot III experiment, located about 45 kilometers southeast of Calgary, Alberta (Figure 3.1), which contained 21 buried geophone groups. The lessons learned (such as the recovery of buried geophones) and the analysis techniques developed on the Chin Coulee data set were applied to the Blackfoot III data, though some adaptation was necessary to handle the much greater volume of data. The Blackfoot III experiment enabled high fold compressional- and converted-wave sections to be produced for each geophone depth, which allowed for a fair assessment of the viability of the buried geophone method.

### 1.1.1. Attenuation Investigation

Near-surface attenuation was studied by burying 3-component geophones to different depths in the overburden layer, and examining the frequency content of upgoing reflections. By avoiding a portion of the near surface, a buried geophone might yield data which is less attenuated than data recorded at the ground surface, and hence have a broader bandwidth. If attenuation is detected, the frequency spectra between geophones of different depths can be used to estimate the shear wave attenuation constant  $Q_s$  for the near-surface layer. If  $Q_s$  is known, then it is possible to design inverse  $Q_s$  filters that could recover at least part of the lost bandwidth for the surface geophone data. If successful, the inverse  $Q_s$  method of improving bandwidth would be more realistic in practice, as it does not require a geophone to be buried at each receiver station, but only at selected locations to estimate approximate near-surface  $Q_s$  values along the seismic line.

### 1.1.2. Vertical Interval Velocities

It has been previously demonstrated through refraction studies (Lawton, 1990) that overburden sediments have a very high  $V_p/V_s$  below the water table, due to the relative insensitivity of shear wave velocity to pore fluid content. In this thesis, data from the buried three-component geophones confirmed this directly by determining the vertical interval  $P$ -wave and  $S$ -wave velocities to an unprecedented resolution. A new technique employing cross-correlations was developed for this purpose. The large number of buried geophones in the Blackfoot III survey also made it possible to determine high resolution lateral variations in  $V_p/V_s$  along the receiver line; there is no published precedent for a study of this kind, so the results revealed the “high frequency” variations in near-surface  $V_p/V_s$  that were previously unknown.

### 1.1.3. Seismic Repeatability

The inherent redundancy in the Blackfoot III experiment was used to investigate seismic repeatability. Repeatability is an important issue in time-lapse seismic studies, as it is crucial to distinguish differences due to the changing seismic properties of the reservoir from differences due to non-reservoir related effects. Because the Blackfoot III geophones recorded simultaneously, their data should be the same except for differences due to geophone burial. Statistical techniques of trace differencing, cross-correlations,

and mean square difference, that are normally used for time-lapse studies, were employed to determine how similar (or repeatable) the processed sections were to each other. From this it was determined if and how seismic data is affected by geophone burial.

#### 1.1.4. Interpretation

A brief interpretation of the Blackfoot III data was made, which was assisted greatly by the availability of full sonic and density logs from a well that tied to the center of the buried geophone receiver line. A log from a nearby off-channel well enabled an interpretation of regional formations, which resulted in a confident interpretation of the channel margins.

#### 1.1.5. Numerical Modeling of Receiver Notching and Reflection Amplitudes

Numerical simulations were used to investigate receiver notching and near-surface reflection amplitudes, to determine if these might be a factor in data recorded by buried geophones. The simulations were designed for meaningful comparisons to the Blackfoot III buried geophone data.

Receiver notching (or ghosting) occurs when an ascending reflection interferes destructively with its multiple from the surface. The interference causes the frequency spectrum of the recorded data to have one or more pronounced gaps or notches at discrete frequencies, which is common in marine surveys (Figure 1.1). This causes distortions in the shape of the recorded wavelet, which can lead to difficulties in seismic interpretation in cases where reflection character is important.

In most land surveys, receiver notching does not occur because geophones are normally planted directly on the surface or in shallow holes, where the incident and reflected wavelets interfere constructively at all frequencies. Data from buried geophones, however, may be affected by receiver notching. Apart from affecting frequency content, receiver notching will also influence reflection amplitudes.

Reflection amplitudes are also influenced by an effect that is entirely independent of wavelet interference. Wave amplitude increases when passing into a material of decreased seismic impedance; as the near surface normally has a sharply decreasing impedance, a wave ascending through it will therefore undergo an increase in amplitude.

As this phenomenon is pertinent to data recorded by geophones buried in the near surface, this was also investigated.

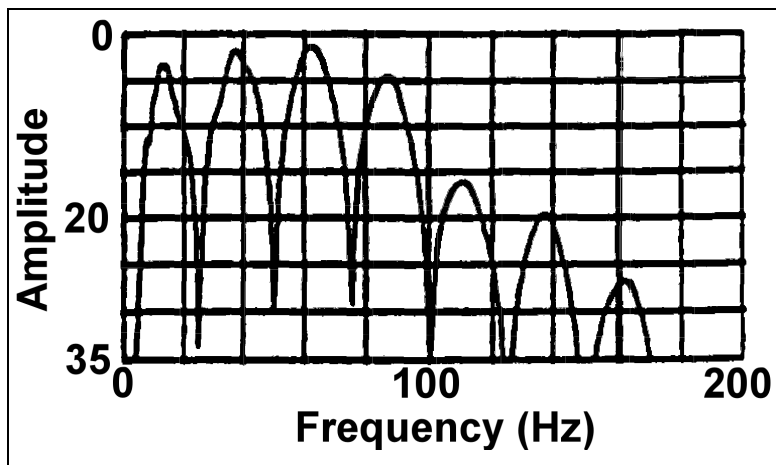


Figure 1.1. Frequency spectra of raw hydrophone data from a marine seismic survey. The pronounced notches are due to the incident primary reflection interfering with its multiple from the water surface (from Sheriff and Geldart, 1995).

## 1.2. Techniques and Software

All data processing and analysis was performed on a Sun/Sparc workstation in a Unix environment. The commercial software package ProMax was used for seismic data processing, data display, and certain common processing techniques such as f-k filtering. Owing to its greater flexibility, the more advanced data analysis and research techniques were performed in the Matlab programming environment. Matlab provided an ideal platform for the creation of many specialized computer programs, written for this thesis, that were used to analyze and model the various subtleties of data from buried geophones. Matlab also allowed access to several in-house development programs that greatly facilitated this research. Where necessary, Matlab and ProMax interfaced indirectly through ASCII and SEG-Y format data.

## 1.3. Literature Review

There are few published results from buried geophone experiments. Houghton (1940) compared reflection character and amplitude of seismic reflections from geophones buried in holes as deep as 104 meters. He also calculated interval velocities

based on seismic delay times between geophones of different depths. Though inconclusive about the reflection character, he noted a clear inverse relation between reflection amplitude and the seismic impedance of the material in which the geophone was planted. He did not attempt a frequency analysis, probably because he worked entirely with analogue data.

Rice *et al.* (1991) observed significant *P*- and *S*-wave attenuation in the near surface from sites in Texas and Utah. Planting the geophones at the bottom of holes up to 6.5 meters in depth greatly improved the bandwidth and quality of the compressional- and shear-wave (*S-S*) seismic sections. Much of the overburden in the experiment areas consisted of very attenuative dry, unconsolidated sand dunes, clay, and pebbles. They concluded that the majority of seismic attenuation occurs in the top two meters or so of the near surface. Given that Rice *et al.* calculated quality factors as low as  $Q_p=0.3$  for the materials in the experiment locations, even burying geophones to a 0.3m depth should be expected to improve bandwidth. The overburden materials also attenuated compressional and shear waves about equally, whereas it appears that *S*-waves are attenuated more than *P*-waves in the overburden of Alberta, which is composed chiefly of glacial till.

Pullin *et al.* (1987) buried single-channel geophones to a 10m depth to avoid the attenuative surface muskeg layer in northern Alberta. Data from the buried phones showed markedly improved bandwidth and smaller static shifts than data from surface geophones in the same area. The geophones of a subsequent 3-D survey were buried at a 13m depth, and the data contained frequencies up to 220Hz, which, together with effective processing, resulted in a high spatial and temporal resolution of the target.

Meunier and Huguet (1998) experimented with buried geophones to improve seismic repeatability for the time-lapse monitoring of a gas storage reservoir in France. A line of permanently buried geophones was anticipated to have better coupling and coupling consistency than surface geophones. Preliminary tests found that geophones buried to depths of 0.3 to 0.7m recorded lower reflection amplitudes due to increasing impedance with depth, and a pronounced notch due to receiver ghosting. The notch faded at depths over 0.7m. Data from geophones buried at 0.8m showed improved repeatability over surface phones owing to improved S/N, though the authors offered a caution over the use of this technique because of the unexpected effects of geophone burial.

## CHAPTER 2

### CHIN COULEE BURIED GEOPHONE EXPERIMENT

The Chin Coulee buried geophone experiment was conducted in May, 1997, as a small add-on to a 3C-2D seismic line shot in southern Alberta (Figure 2.1). Topographic relief in the area was very low (variation <5 meters) and surficial geology was mainly recessional moraine composed of unsorted silt, sand and gravel (Westgate, 1963).



Figure 2.1. Location of Chin Coulee buried geophone experiment.

#### 2.1. Geometry and Acquisition

The source was 4 kilograms of dynamite detonated at a depth of 18 meters, with a nominal shot interval of 40 meters. The receiver interval for the line was 20 meters, with a maximum source-receiver offset of 1300 meters.

The experiment was performed at three separate locations on the line, designated as group 1, located near the eastern end of the line, group 2 in the center, and group 3 near the western end. The groups were placed at receiver stations of the 2D seismic line, and were about 10 kilometers apart, and so had no common shot points. At each location, a drill rig augured three adjacent vertical holes to different depths, as detailed in Table 2.1 (for completeness, the surface geophone location is also included). Hole excavation was facilitated by injecting water into the hole while auguring.

|                | <b>Depth 1</b> | <b>Depth 2<br/>(m)</b> | <b>Depth 3<br/>(m)</b> | <b>Depth 4<br/>(m)</b> |
|----------------|----------------|------------------------|------------------------|------------------------|
| <b>Group 1</b> | 0              | 6                      | 12                     | 18                     |
| <b>Group 2</b> | 0              | 6                      | 10                     | 18                     |
| <b>Group 3</b> | 0              | 5                      | 11                     | 17                     |

Table 2.1. Chin Coulee buried geophone depths.

The receivers used were OYO Geospace three-component geophones. The geophones were first placed on a planting pole, aligned visually so that the radial channel paralleled the 2-D line, and then lowered down the hole. Several planting poles had to be linked together before the phones reached the bottom. Pole-planters generally encountered 1 to 3m of thick mud before achieving a reasonably firm plant at the bottom of the hole, which was attained by both planters leaning their full weight on the poles. As anticipated, these geophones could not be recovered. Hole locations and depths were marked with stakes. The surface geophones were hand planted in a 15-cm deep hole, leveled and aligned, and covered to reduce wind noise.

The seismic recorder activated the buried phones when the receiver location became part of the active spread. Three seconds of data were collected at a sample rate of 2ms, and stored by the contractor as a separate line. The data were sifted off and delivered at a later date.

## **2.2. Processing**

The entire dataset consisted of 36 common receiver gathers (3 groups with 4 receivers per group, and 3 channels per receiver), each containing an average of 65 traces. For display purposes, pad traces and variable trace spacing are used, as field operations

required that some shot stations had to be skipped. Usually fold was maintained by halving the shot interval around these areas. Important processing steps are outlined in Table 2.2.

|   |
|---|
| <b>SEG-Y import</b>   |
| <b>Assign geometry</b>  |
| <b>Reverse polarity of trailing shots</b> (radial channel only)                 |
| <b>Pad traces, 40 meter interval</b>  |
| <b>Spatial resample to 40 meter interval</b> (for f-k filter only)              |
| <b>Bandpass <i>or</i> f-k filter</b>  |
| <b>Automatic gain control <i>or</i> scalar gain</b> (for display purposes only) |

Table 2.2. Processing steps for the Chin Coulee buried geophone data.

### 2.3. Traveltime Analysis

Figure 2.2 shows the raw data for all channels of group 2. Only a single scalar gain was used for all traces, so relative amplitudes within each gather and between gathers have been preserved. Surface waves are clearly prominent at all receiver depths, and their amplitude decays with geophone depth. Amplitudes of reflections and refractions can also be seen to decrease with greater geophone depth, which is a phenomenon due to the near-surface impedance gradient discussed in Chapter 4.

To reduce ground roll and enhance reflections, the gathers were passed through a 10-20Hz Ormsby highpass filter followed by a 500ms AGC. Results for all components in group 1 are displayed in Figure 2.3 (the rectangular trace windows plotted on the gathers are discussed in the next section). On all vertical channels, high-frequency events between 500 and 1100ms displaying hyperbolic moveout are  $P$ - $P$  reflections corresponding approximately to the Bow Island to Elk Point formations. The  $P$ - $P$  reflections have a similar appearance at all geophone depths.  $P$ -wave reflections can be observed to arrive progressively later between the deepest and surface geophones (vertical interval velocities based on this time delay are discussed in Chapter 2.6). Similar observations were made for the data from groups 2 and 3.

In Figure 2.3, radial channel, the hyperbolic low-frequency events at mid- to far-offsets from about 900 to 2000ms are converted-wave reflections corresponding approximately to the Second White Specs to Shunda formations. There is, overall, more converted-wave energy on the radial channel than on the transverse channel. For this reason, all converted-wave analysis was performed using the radial channels. As with the compressional-wave reflections, the converted-wave reflections appear very similar for geophones placed at different depths.

## **2.4. Frequency Analysis**

Any necessary bandpass or f-k filtering was performed in ProMax. The data were then exported as SEG-Y format, and imported to Matlab for frequency analysis. The frequency analysis was performed using software described by Margrave (1999), as it permitted a high degree of versatility in the selection of analysis windows.

### 2.4.1. Raw Data

Regions in the common receiver gathers that are relatively uncontaminated by ground roll and refractions occur between times of 700 and 1600ms at mid- to far-offsets. It was these areas of the receiver gathers that were chosen for frequency analyses, as they contained relatively noise-free reflections. Analysis windows for the raw data are shown in Figure 2.3 (gray rectangles). The window times correspond approximately to reflections from the Mannville to Elk Point formations. These occurred between 700 and 1100ms for the *P-P* reflections, and about 1000 to 1600ms for *P-S* reflections. Data from group 3 contained broad no-shoot zones through areas expected to contain *P-S* reflections uncontaminated with coherent noise, so only a narrow strip of far-offset traces was analyzed for the radial channel of these gathers.

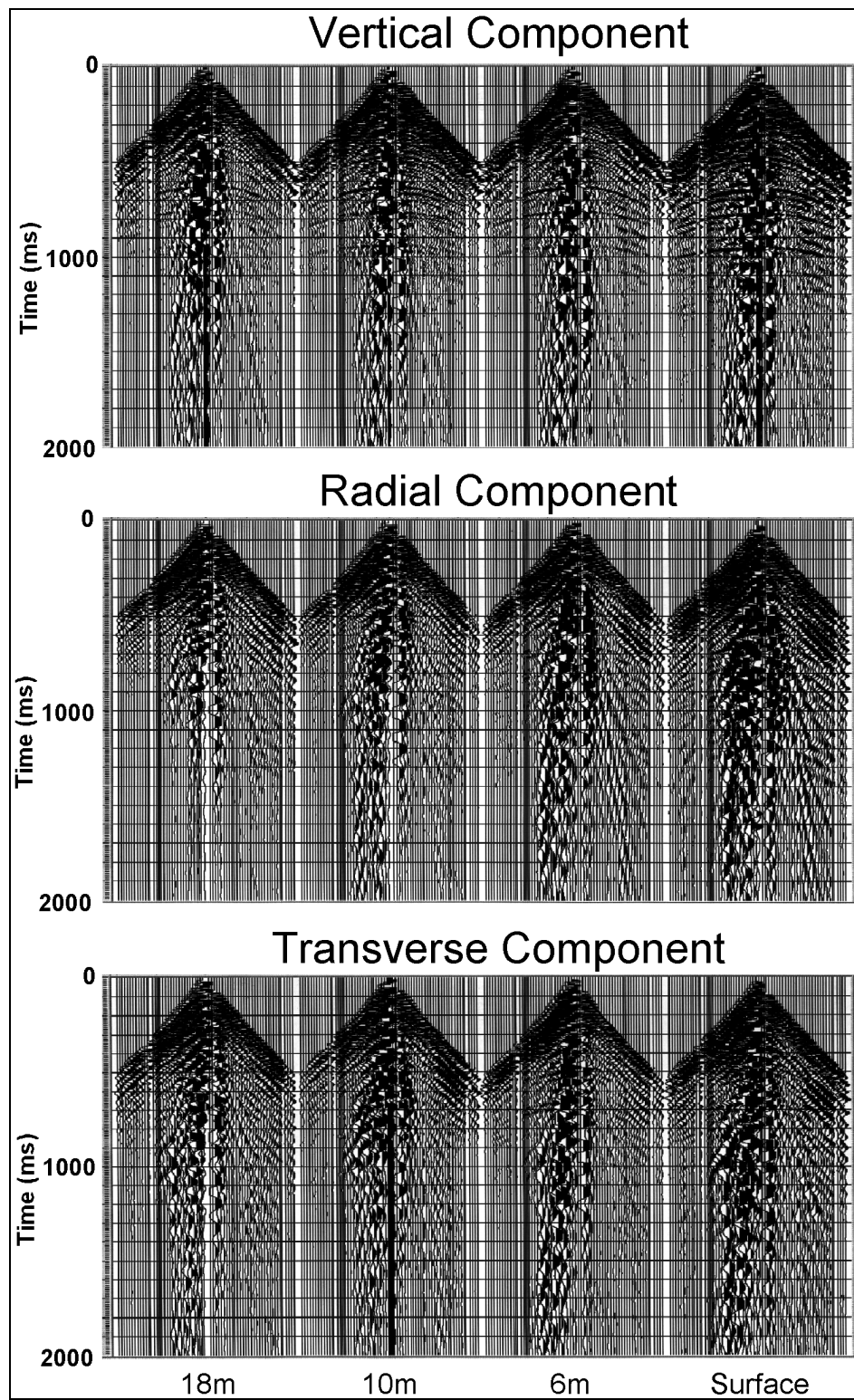


Figure 2.2. Group 2, raw traces, all components and depths.

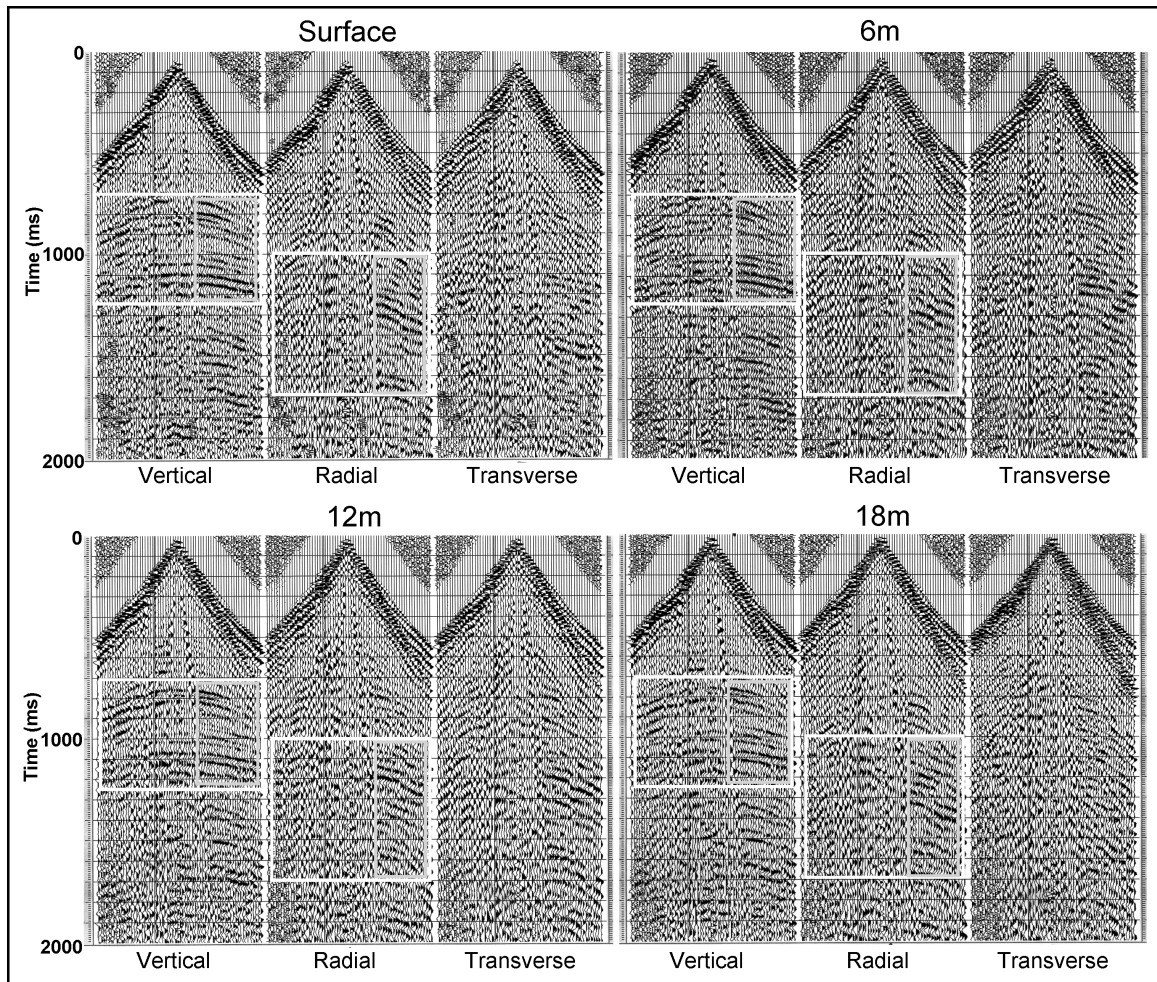


Figure 2.3. Group 1 receiver gathers, all channels. Data have been filtered to suppress ground roll and gained with a 500ms AGC. Rectangles represent frequency analysis windows (see text for details).

Results of the frequency analysis of these time windows for the raw receiver gathers for groups 1 and 2 are shown in Figure 2.4. The frequency spectra for the vertical and radial channels at all geophone depths are plotted on a vertical scale representing decibels down from maximum amplitude.

The  $P$ - $P$  reflections have a signal width between about 10 and 45Hz, with strongest amplitudes between 15 and 30Hz (Figure 2.4 (a),(c)). There is a notching pattern that is fairly consistent between the  $P$ - $P$  reflections in each group, but not between groups. These notches are possibly due to near-surface reverberations (source ghosting). As expected, there is no evident trend of additional loss of high frequency signal between the deepest and surface geophones.

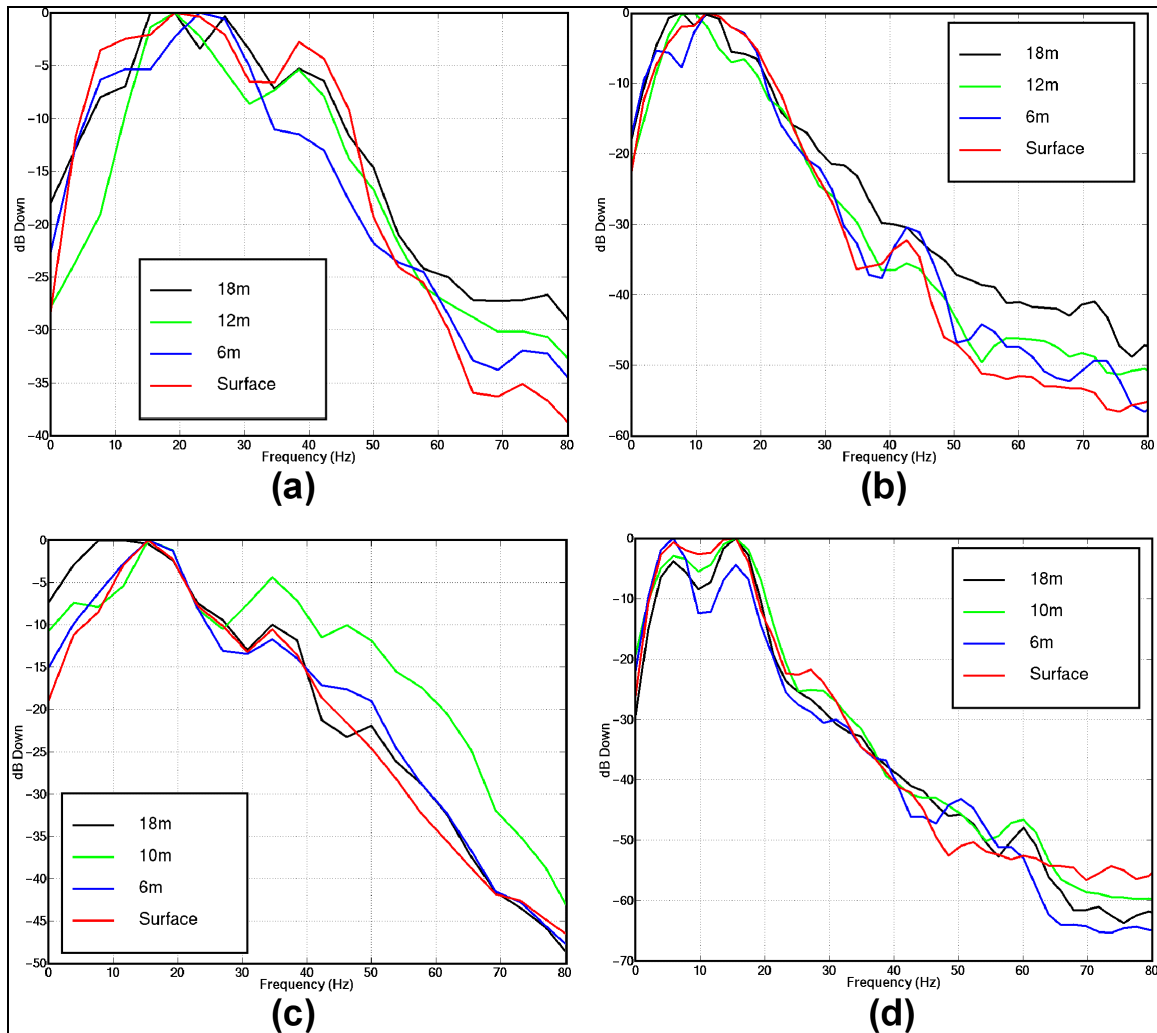


Figure 2.4. Raw data frequency analysis: (a) group 1 vertical channel, (b) group 1 radial channel, (c) group 2 vertical channel, (d) group 2 radial channel.

The amplitude spectra of the raw  $P$ - $S$  reflections, (Figure 2.4 (b),(d)), have a much narrower bandwidth than the  $P$ - $P$  reflections, as has been observed for most multi-component surface seismic data (e.g., Zhang *et al.*, 1994). The  $P$ - $S$  reflections are, therefore, at all depths, more attenuated than the  $P$ - $P$  reflections. There are two fairly consistent peaks at 5 to 7Hz and 12 to 16Hz in the spectra. The lower peak is due to some ground roll noise captured in the analysis window; the higher frequency peak is from  $P$ - $S$  reflections. As with the  $P$ - $P$  reflections, no apparent difference in bandwidth for geophones at different depths is evident.

#### 2.4.2. Bandpass Filtered Data

The data were passed through a 10-20Hz Ormsby highpass filter to reduce the ground roll noise observed in the frequency spectra of the raw radial data. The windows selected for frequency analysis were expanded to include all offsets for vertical channel data (the white rectangles in Figure 2.3), but remained at mid- to far-offsets for the radial channels (the gray rectangles). Results for groups 1 and 2 are plotted in Figure 2.5. As with the vertical channel raw data, the high-passed data do not indicate *P-P* reflection attenuation between the deepest geophone depth and the surface. The high-passed radial channel data show that *P-S* reflections are confined mostly to the 10 to 22Hz range. With the ground roll suppressed, the data are normalized to the maximum amplitude of the *P-S* reflections (as opposed to the ground roll), and no differential attenuation is evident between the different depths. Similar observations were made for the frequency analysis of group 3.

Additional testing using filters of different passbands showed no significant variation in shear-wave bandwidth between the different depths.

#### 2.4.3. f-k Filtered Data

To reduce coherent noise, the data were passed through an f-k filter polygon designed to reject ground roll and refracted arrivals. The f-k filter had dimensions of 2000ms  $\times$  45 traces, with a value of 95% used for time ramp flattening, offset ramp flattening and f-k filter windowing. The filter passed frequencies between 6 and 70Hz, and absolute velocities greater than 2900m/s. Figure 2.6 shows the f-k filter pass, reject and input data for the radial channel of the group 1, 6m depth geophone. Though the converted-wave reflections are barely discernible in the raw data in Figure 2.6(c), the filter effectively removes the surface waves as shown in Figure 2.6(b), allowing the converted-wave reflections to emerge clearly (Figure 2.6(c)). Similar results were obtained for the vertical channel data. The window for frequency analysis on the vertical channel included all offsets (the white rectangles in Figure 2.3), as reflections were observed to be fairly strong across the entire gather. The analysis window for the radial channels again remained confined to mid- to far-offsets (the gray rectangles), due to the absence of signal at near offsets. This lack of signal near the center of the radial receiver

gathers was due to the lower amplitude of  $P$ - $S$  mode conversions at small angles of incidence.

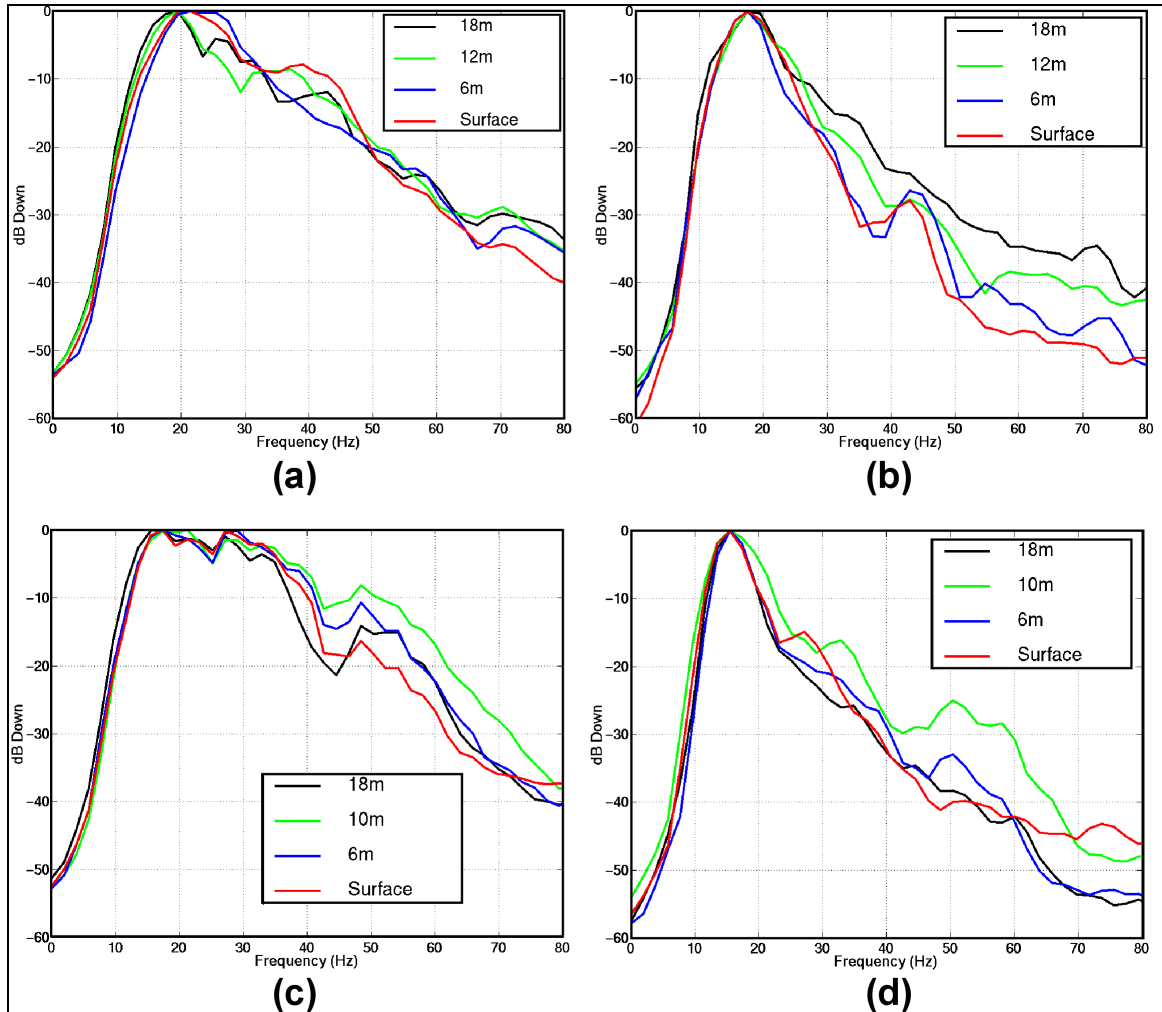


Figure 2.5. Frequency spectra of 10-20Hz high-passed  $P$ - $P$  and  $P$ - $S$  reflections: (a) group 1 vertical channel, (b) group 1 radial channel, (c) group 2 vertical channel, (d) group 2 radial channel.

The frequency spectra of the  $f$ - $k$  filtered gathers are displayed in Figure 2.7. As before,  $P$ - $P$  reflections have a comparable bandwidth at all depths, with no evidence of differential attenuation between the deepest and shallowest geophones. The radial channels show that the  $P$ - $S$  reflections have a narrow 10-20Hz bandwidth, and again there is no evidence of shear-wave attenuation.

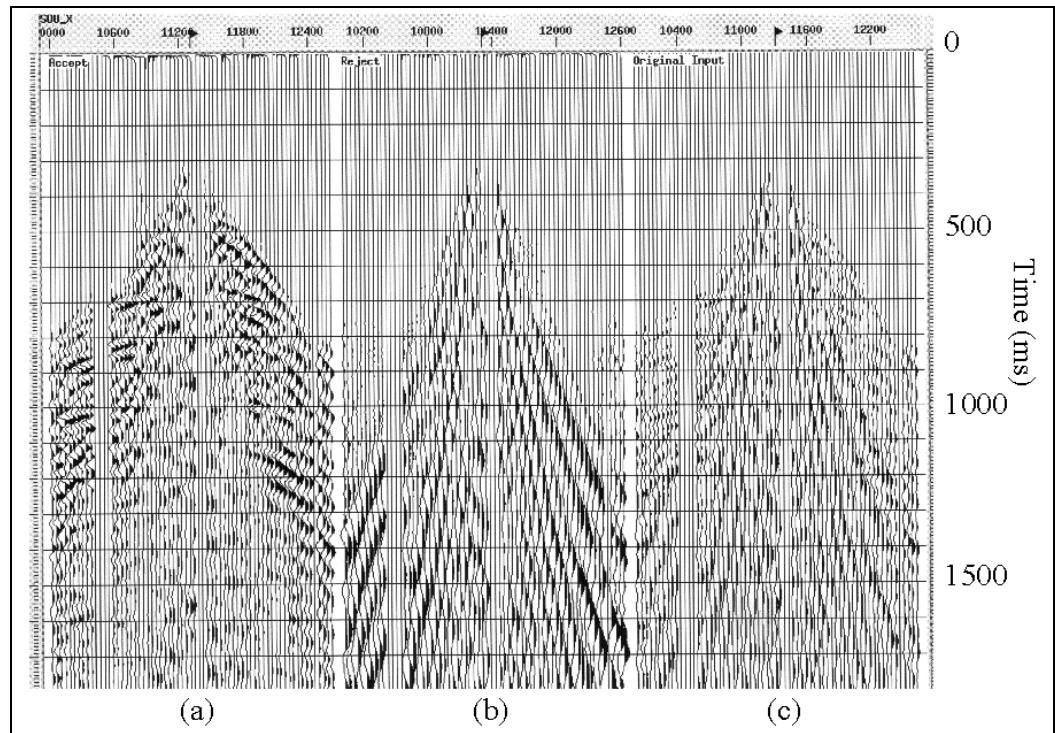


Figure 2.6. Performance of f-k filter on radial channel data. (a) Pass, (b) reject and (c) original input.

## 2.5. Mode leakage and receiver re-orientation

The radial and transverse channels are relatively uncontaminated by  $P$ - $P$  mode leakage. There is moderate  $P$ - $P$  leakage on the radial channels at the 6 and 10m depth geophones of group 2, but these can be observed not to interfere with later  $P$ - $S$  events. For reasons not completely clear, there is generally more  $P$ - $P$  mode leakage on the transverse channel than the radial channel. Various component rotations were attempted, but were found, at best, to only nominally increase the amplitude of the converted-wave reflections on the radial channel. This indicates that the geophones did not rotate greatly from their desired orientation as they were lowered down the holes.

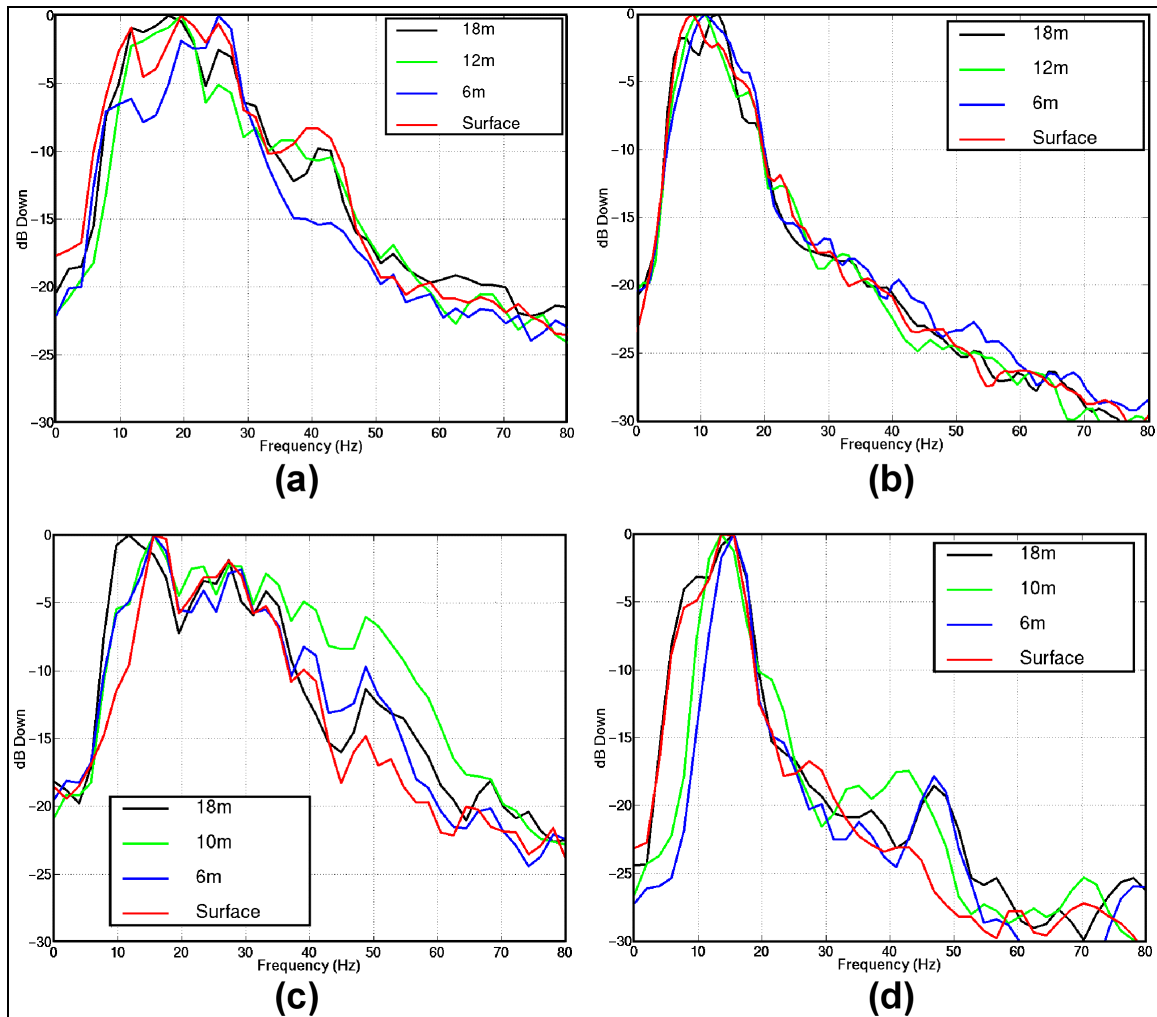


Figure 2.7. Frequency spectra of f-k filtered  $P$ - $P$  and  $P$ - $S$  reflections: (a) group 1 vertical channel, (b) group 1 radial channel, (c) group 2 vertical channel, (d) group 2 radial channel.

## 2.6. Vertical Interval Velocities

With this experiment, it is possible to directly calculate the  $P$ - and  $S$ -wave interval velocity of the overburden between any two buried geophones in the same group, with the assumption that the reflection ascends vertically through the near-surface. The ascending reflections reach successively shallower geophones at progressively later times. Since the depths of the geophones are known, and the reflection arrival times are recorded in the traces, the interval velocities can be calculated directly. Figure 2.8 is a demonstration of a package of  $P$ - $P$  reflections arriving at progressively later times for shallower geophones; the gray lines correlate the same events across the different traces. It can be seen that

time lags increase for shallower geophone intervals. Given that the geophones are equally spaced, this is a direct demonstration of a sharp decrease in  $P$ -wave velocity through the top 18m of overburden.

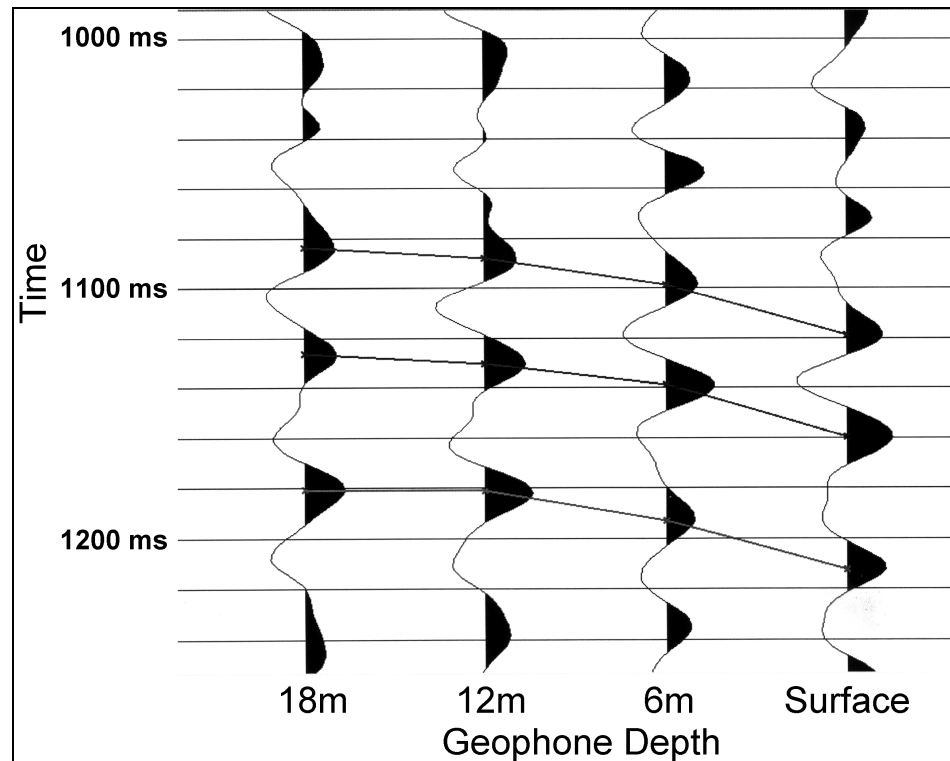


Figure 2.8. Compressional-wave reflections (correlated with the gray lines) arrive later for shallower geophones.

Though the reflection time lags can be read directly off the traces of Figure 2.8, they were calculated more precisely by cross-correlating the traces over time windows that contained numerous strong, clear reflections. The time of the cross-correlation function maximum represents the average lag time of several reflections, not just of one particular event. This averaging property of cross-correlation improves time lag accuracy by suppressing random noise between traces. Further accuracy is achieved by taking advantage of the redundancy of the experiment, and calculating a reflection time lag between the geophones for every shot. The cross-correlation technique is applied to  $f$ - $k$  filtered data, because the  $f$ - $k$  filter suppresses coherent noise (refractions and ground roll) that tends to correlate between traces.

Figure 2.9 shows the output correlograms from cross-correlating the receiver gathers from the 18m and surface geophone vertical channels from group 1. The time window for cross-correlation is outlined by the white rectangles in Figure 2.3. Higher amplitudes of the cross-correlation function indicate better correlation, both within each correlogram and between correlograms. There is a fairly consistent alignment of peak values at a lag time of 34 ms, indicating that peak cross-correlation values are from coherent reflections. Correlation values are highest for mid- to far-offsets, and lower near the center of the gather. The center of the gather was largely contaminated with ground roll prior to f-k filtering, as seen in Figure 2.2, which caused this poor correlation.

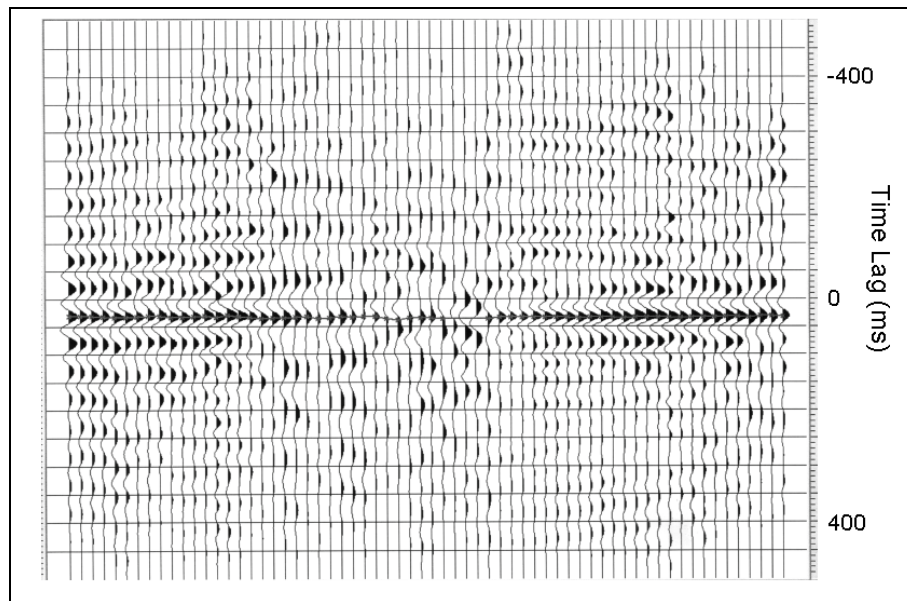


Figure 2.9. Correlograms for the 18m to surface vertical channel common receiver gather cross-correlation. The average time of the peak values is used to calculate the velocity of the interval between the two receivers.

Lag times were determined in ProMax by selecting the correlogram peaks with a horizon picking tool, which “snaps” to the exact time of all the peaks (as shown by the gray line on Figure 2.9). Where there was poor correlation, the picks were deleted manually. The horizon was then saved to the database, and later exported as ASCII data. A computer program read the ASCII file and calculated the average time of the picks. This average lag time was used to calculate the interval velocity. Several receiver gathers correlated poorly at all offsets, which prevented an interval velocity calculation.

Figure 2.10 shows the time lag at which maximum correlation occurred for selected geophone intervals of group 1. The 18m to surface lag is a test of the robustness of the technique, because the three interval lag times between 18m and surface should sum to the total lag time from 18m to surface. The difference between the sum of the average interval lag times and the total lag time (excluding traces from the center of the gather) is only 0.9ms, indicating that interval times are being determined with high precision.

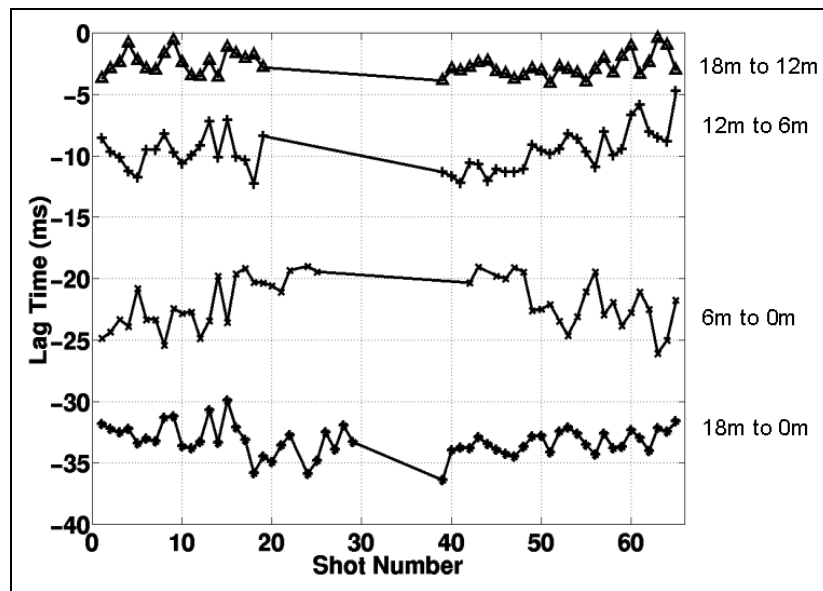


Figure 2.10. Lag times of vertical channel cross-correlation maximum values, for selected geophone intervals of group 1.

The above plot clearly demonstrates the dramatic *P*-wave velocity change over the top 18m of the near-surface layer. The average time lag between the 18m and 12m depth is 2.5 ms, resulting in a *P*-wave interval velocity of about 2400m/s. The 12m to 6m interval has a time lag of about 10.5 ms, giving an interval velocity of 570m/s, and the 6m to surface interval has a time lag of about 19.5 ms, giving an interval velocity of about 310m/s. The large drop in velocity between the two lowest intervals is probably due to the water table. Lawton (1990) found similar results for a refraction survey near Jumping Pound, Alberta.

Figure 2.11 shows schematically the *P* and *S*-wave velocities between every interval for which it could be confidently calculated, for all three groups. Where both *P*

and  $S$ -wave velocities have been determined,  $V_p/V_s$  for that interval is given in the right-hand column.

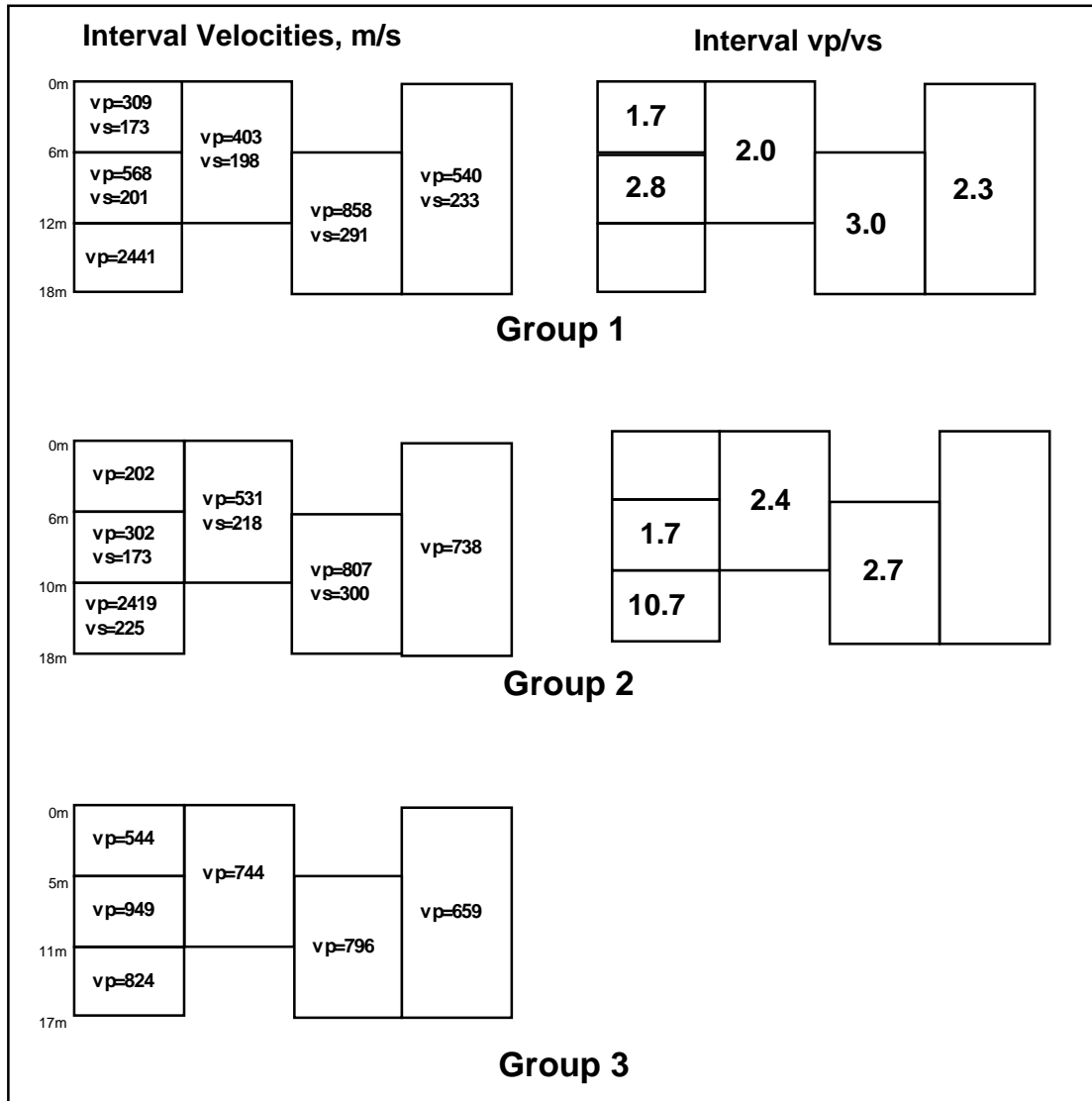


Figure 2.11.  $P$ - and  $S$ -wave interval velocities and  $V_p/V_s$  for the Chin Coulee buried geophone experiment.

The results show that  $S$ -wave velocity falls in the 150-300m/s range, expected for unconsolidated sediment, and increases slightly with depth. The comparison of the lowest to middle interval of group 2 demonstrates that shear-wave velocity is not affected by the water table, while  $P$ -wave velocity is far greater below the water table than above. Again these results are similar to those obtained by a refraction survey (Lawton, 1990),

and expected, as it is known that *S*-wave velocities are not affected by pore fluid content to the extent that *P*-wave velocities are. This great difference between *P*-wave and *S*-wave velocities in saturated overburden results in an extreme  $V_p/V_s$  of 10.7 for the 18 to 10m interval of group 2. Probably due to lack of good reflections, interval velocities of group 3 are inconsistent and no water table is indicated.

The large values of  $V_p/V_s$  imply that *S*-waves in saturated overburden have a wavelength about a tenth that of *P*-waves of the same frequency. As attenuation for a wave is proportional to the number of cycles it completes, shear waves would be expected to attenuate much faster in a saturated overburden layer than compressional waves of the same frequency, assuming an approximately equivalent attenuation constant for each mode. A thick but mostly saturated overburden layer should account for the much greater attenuation observed in the converted wave than the compressional-wave reflection.

A three-layer weathering layer model was obtained from the company that processed data from the 2-D seismic line. This model was based on a multi-layer *P*-wave refraction analysis. Layer 1 represents "unsaturated overburden", has a *P*-wave velocity of 610m/s, layer 2 is "saturated overburden" with a velocity of 2184m/s, and layer 3 is considered to be bedrock, with a velocity of 2827m/s. The model agrees with observations from vertical interval times in broad terms only, for groups 1 and 2. Both the model and the vertical interval velocities from the buried geophones indicate a water table depth of 10m for group 2. The model indicates an absence of saturated overburden for group 1, whereas *P*-wave interval velocities suggest the presence of a water table between 12 and 18 meters.

## CHAPTER 3

### BLACKFOOT III BURIED GEOPHONE EXPERIMENT

#### 3.1. Introduction

The Blackfoot III buried geophone experiment is essentially a much larger version of the Chin Coulee experiment (Chapter 2). The survey was designed to make it possible to produce compressional- and converted-wave sections from receiver lines at depths of 0, 6, 12 and 18m below the surface. This means that, in addition to the pre-stack data analysis techniques developed for the Chin Coulee data, the stacked data can also be analyzed to determine the effects of geophone burial on the quality of the final seismic images.

#### 3.2. Location

The Blackfoot field is located in Township 23, Range 23W4, in Alberta, Canada (Figure 3.1). It produces oil from porous, channel-fill sediments of the Lower Cretaceous Glauconite Member of the Mannville formation. The surficial geology is composed of Pleistocene and Recent glaciolacustrine and lacustrine silts and clays (Shetsen, 1987) at the location of the buried geophones.

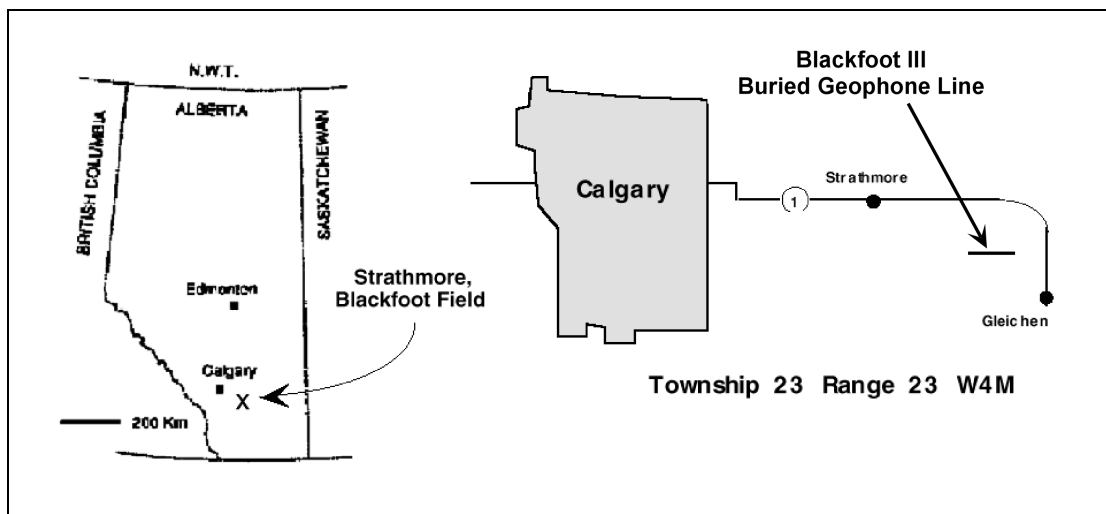


Figure 3.1. Location of the Blackfoot III buried geophone experiment (from Gallant *et al.*, 1995).

### 3.3. Geometry and Acquisition

The shot line was three kilometers long and oriented nearly east-west (Figure 3.2). The source was 4 kg of dynamite detonated at 18m depth, at a nominal shot spacing of 20m. The receivers were OYO three-component geophones. The buried geophones were specially modified for the experiment (Figure 3.3). First, 15-cm sand spikes were affixed to the bottom of the geophones, then they were threaded with 3/16" aircraft cable looped through holes drilled through the plastic casing and sand spike. The sand spikes, because they protrude from the bottom, were intended to prevent the geophones from turning sideways in the hole during emplacement and extraction, which would prevent mode leakage and possible damage to the geophone. The aircraft cable enabled the geophones to be winched out of the hole after the survey.

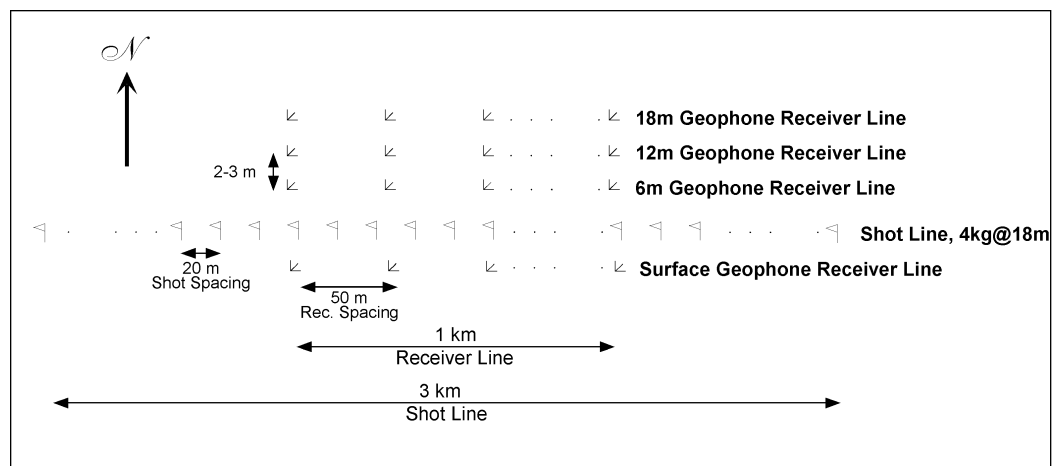


Figure 3.2. Blackfoot III buried geophone experiment survey geometry.

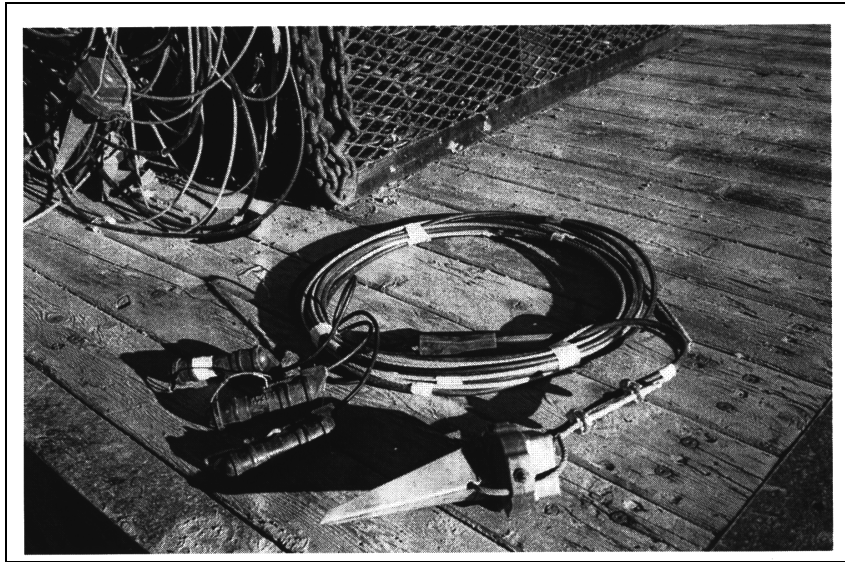


Figure 3.3. Geophone fitted with a sand spike and aircraft cable.

Twenty-one buried geophone stations occupied the central kilometer of the shot line, at a spacing of 50 meters. At each station, a shot hole rig augured three holes to approximately 6, 12 and 18m depth. The modified geophones were affixed to the end of a wooden planting pole and lowered down each hole. Pole planters encountered varying amounts of thick mud before obtaining a firm plant. In many cases, the geophones could not be placed at the desired depth due to borehole infilling and obstructions, or because the augur could not drill a deep enough hole due to bedrock or boulders. At three stations, the 18m phone could not even be placed as deeply as the 12m phone. For simplicity, each geophone level will be referred to as 6m, 12m and 18m, even though not every geophone attained the desired depth. Figure 3.4 shows the actual geophone depths for each station.

Geophones were also hand-planted, leveled and aligned on the surface. The geophones were live for all shots, and recorded six seconds of data at a 1ms sample rate.

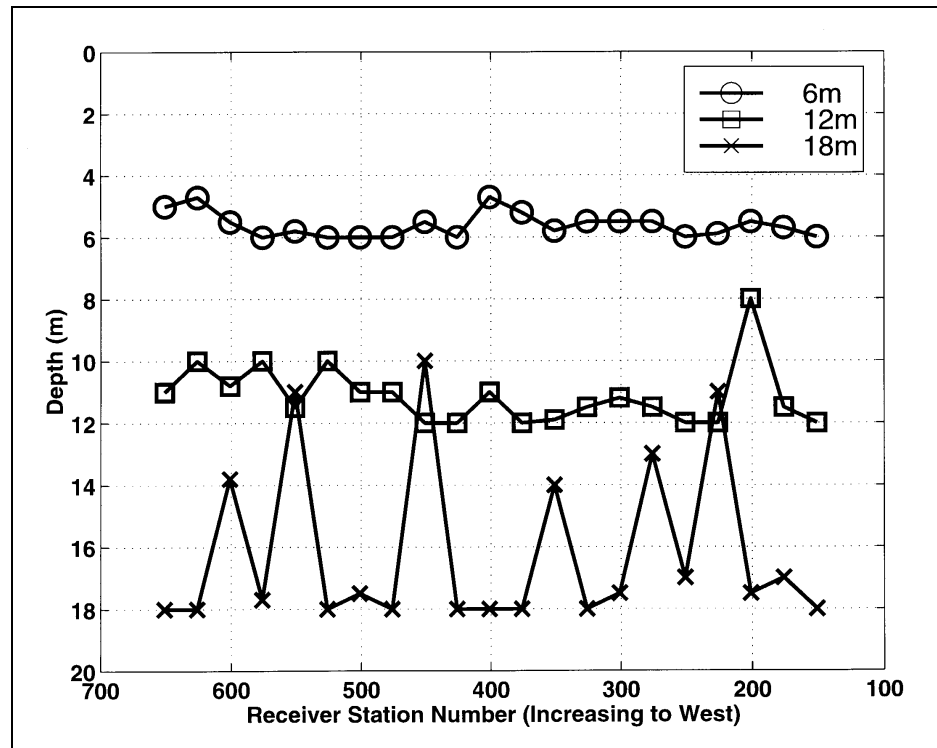


Figure 3.4. Actual buried geophone depths below surface. Geophones could not always be placed at the desired depth due to borehole obstructions.

### 3.4. Processing

All data for the Blackfoot III buried geophone experiment were processed in ProMax. The survey geometry resulted in a maximum fold of 65 (Figure 3.5(a)) for the vertical channel sections, and 76 for the radial channel sections (Figure 3.5(b)). The first 2.5 seconds of data were processed, which contained the zone of interest, and was sufficient to tie in the longest synthetic traces for interpretation (Chapter 5).

#### 3.4.1. Vertical Channel

The vertical channel data were binned to a 25m CDP spacing, and processed to preserve the relative amplitudes within each section. The processing flow was identical for surface and buried receiver data, with the exception that the buried geophone data required receiver kills. An independent residual statics calculation was made for each geophone level, as receiver statics would obviously be different. The main processing steps for the vertical channel data appear in Table 3.1.

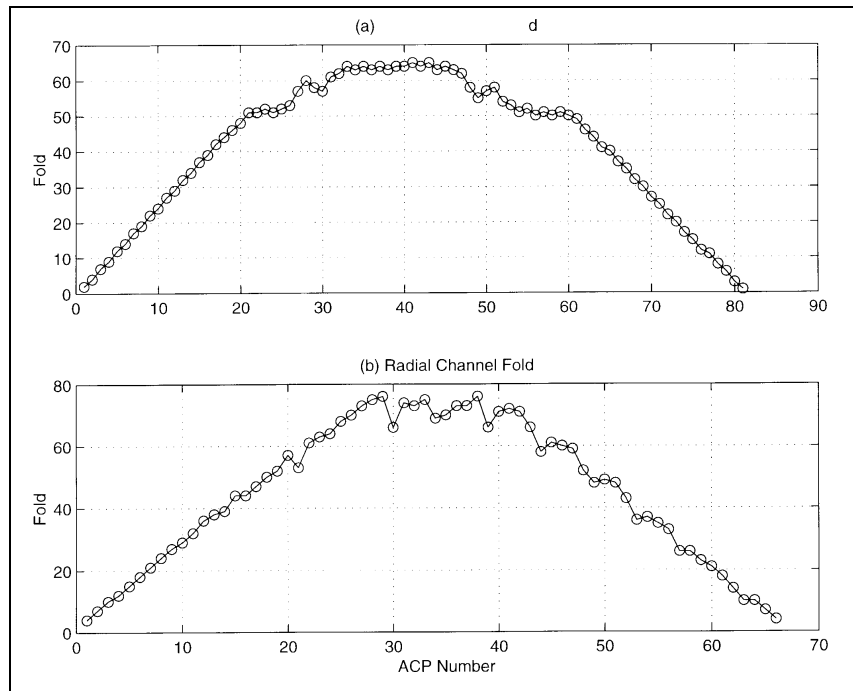


Figure 3.5. (a) Vertical channel fold. (b) Radial channel fold.

|  |
|--|
| <b>1. Assign geometry</b>  |
| <b>2. Surface-consistent deconvolution</b>   |
| <b>3. True amplitude recovery:</b> <i>4db/sec gain and correct for geometric spreading</i> |
| <b>4. Time-variant spectral whitening:</b> <i>Balance frequencies between 6 and 130Hz</i>  |
| <b>5. Elevation statics:</b> <i>Calculated using elevations and uphole shot times</i>      |
| <b>6. Velocity analysis</b>  |
| <b>7. Residual statics:</b> <i>Apply correlation autostatics</i>                           |
| <b>8. NMO correction:</b> <i>No stretch mute</i>   |
| <b>9. Top mute</b>   |
| <b>10. Time-variant scaling</b>  |
| <b>11. CDP stack:</b> <i>15% Alpha-trim mean</i>   |
| <b>12. Bandpass filter:</b> <i>8-12-100-120Hz zero phase Ormsby</i>                        |
| <b>13. Trace equalization</b>  |
| <b>14. Migration:</b> <i>Phase shift time migration at 90% stacking velocities</i>         |

Table 3.1. Main processing steps for the buried geophone vertical channel data.

The fully processed sections for the vertical channel data are shown in Figures 3.6 and 3.7. The quality of data from the four different depths is similar.

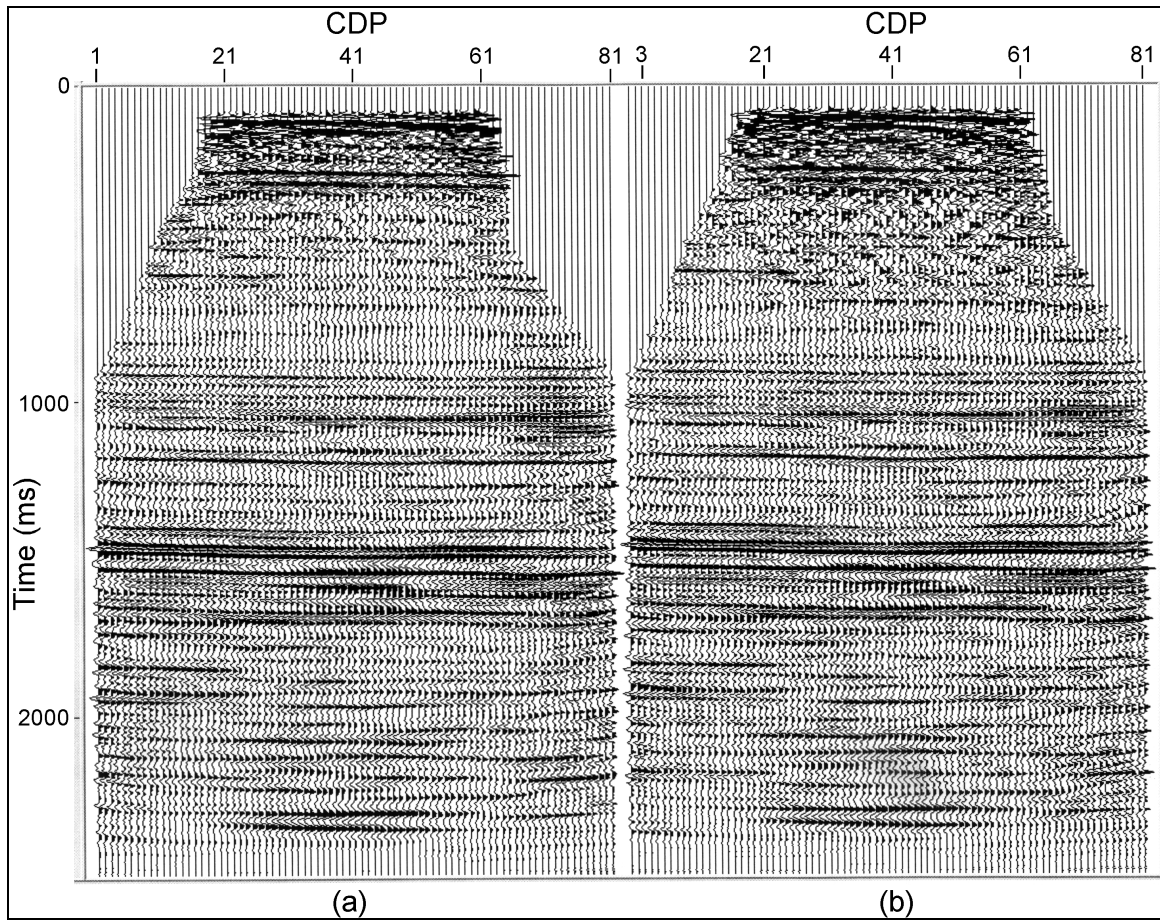


Figure 3.6. Fully processed vertical channel data from (a) surface geophones, (b) 6 meter depth geophones.

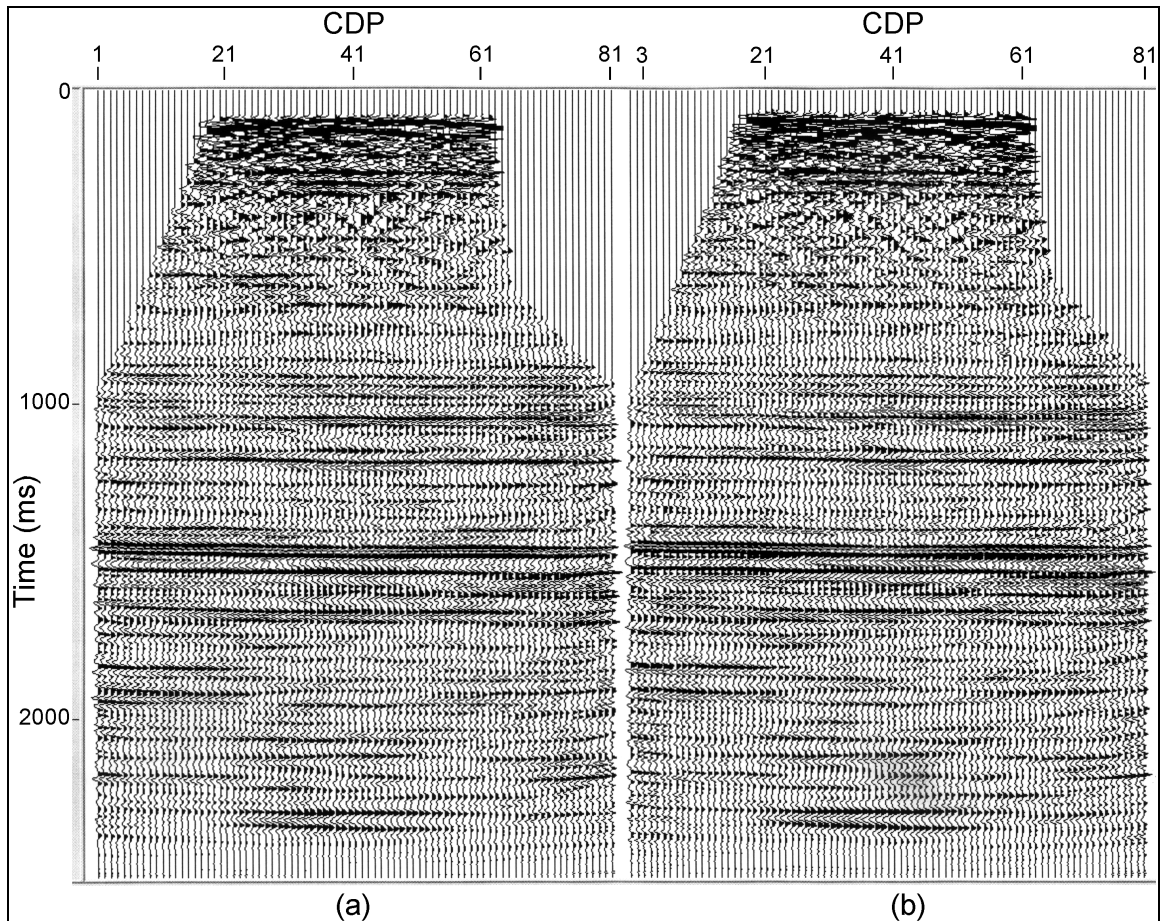


Figure 3.7. Fully processed vertical channel data from (a) 12 meter depth geophones, (b) 18 meter depth geophones.

### 3.4.2. Horizontal Channels

In general, the  $P$ - $S$  data from all geophone depths had lower signal-to-noise ratios, reduced bandwidth and larger receiver statics compared to the compressional-wave data. These observations are usual for multi-component seismic surveys (e.g. Zhang *et al.*, 1994). The buried geophones were affected by additional problems of polarity reversals and mode leakage, which were not observed in the surface seismic data. These are acquisition-related problems caused by a tendency for geophones to twist out of alignment with the shot line and tilt away from vertical during planting, respectively resulting in converted-wave reflections on the transverse channel and compressional-wave reflections on one or both of the horizontal channels. In many instances, converted-

wave reflections had approximately equal amplitude on both the radial and transverse channels.

Because of these and other factors, the horizontal channel data required several additional processing steps and specialized processing techniques that were not required for the vertical channel data. Descriptions of these special considerations follow in the next sections. Important processing steps for the horizontal channel are listed in Table 3.2.

|   |
|---|
| <b>1. Assign geometry</b>   |
| <b>2. Bin data by ACP:</b> <i>Traces binned assuming <math>V_p/V_s=1.9</math>; bin size=25m</i>   |
| <b>3. True amplitude recovery:</b> <i>4db/sec gain and correct for geometric spreading</i>  |
| <b>4. Surface-consistent deconvolution</b>  |
| <b>5. Polarity correction:</b> <i>Flip polarity of trailing spread</i>  |
| <b>6. Trace math or receiver re-orientation:</b> <i>Sum radial and transverse channels, or apply horizontal channel re-orientation (buried phones only)</i> |
| <b>7. Time-variant spectral whitening:</b> <i>Balance frequencies between 6 and 80Hz</i>  |
| <b>8. Elevation statics:</b> <i>Calculated using elevations and uphole shot times</i>   |
| <b>9. Velocity analysis</b>   |
| <b>10. Receiver hand statics</b>  |
| <b>11. Receiver event alignment</b>   |
| <b>12. Residual statics:</b> <i>Correlation autostatics</i>   |
| <b>13. NMO correction:</b> <i>No stretch mute</i>   |
| <b>14. Top mute</b>   |
| <b>15. Bottom mute</b>  |
| <b>16. Time-variant scaling</b>   |
| <b>17. ACP stack:</b> <i>15% alpha-trim mean</i>  |
| <b>18. Bandpass filter:</b> <i>6-10-60-70Hz zero phase Ormsby</i>   |
| <b>19. Trace equalization</b>   |
| <b>20. Migration:</b> <i>Phase shift time migration at 110% stacking velocities</i>   |

Table 3.2. Major processing steps for Blackfoot III buried geophone *P-S* data.

#### 3.4.2.1. *P-S Asymptotic Binning*

The trace binning strategy differs between vertical and radial-channel data, because the source-receiver midpoint does not in general represent the point of mode conversion. Instead, the conversion point asymptotically approaches the point  $x_c=x\gamma/(1+\gamma)$  at greater depth, where  $x$  is the total source-receiver offset and  $\gamma$  is  $V_p/V_s$

(Fromm *et al.*, 1985). The variable  $x_c$  is referred to as the asymptotic conversion point (ACP), and is about two-thirds closer to the receiver than the source for a  $V_p/V_s$  of 2.0. This binning method is a good approximation of the true depth-variant common conversion point. The data for the buried geophones were binned to a 25m ACP spacing, assuming a  $V_p/V_s$  of 1.9. This value was chosen based on interval  $V_p/V_s$  values for an earlier 3D survey acquired in the Blackfoot area (Yang *et al.*, 1996).

#### 3.4.2.2. *Mode Leakage and Receiver Re-orientation*

Some degree of mode leakage was observed in about half of the buried geophone data. The types of mode leakage encountered were compressional-wave reflections on the radial channel and converted-wave reflections on the vertical channel. This is a problem that affects signal-to-noise ratios in converted-wave sections.

Some success at reducing mode leakage was met using receiver re-orientation. Since three-component geophones record particle motion in all three dimensions, the orientation of the x, y and z axes is somewhat arbitrary, and does not necessarily have to correspond to the vertical, radial, and transverse components of the geophone. The data can be transferred to new co-ordinate axes using vector projections (DiSiena *et al.*, 1984; Alford, 1986). The resulting traces represent what would have been recorded had the receiver been in the new orientation. This is a crucial step in 3C-3D data processing, as converted-wave amplitude is greatest on a horizontal detector that is parallel (radial) to the source-receiver azimuth (e.g. Simin *et al.*, 1996). This is not the case for most shots in a 3C-3D survey, so the horizontal traces are re-oriented.

In the buried geophone experiment, the true orientation of buried geophones is unknown, and so was determined indirectly through a three-component first break analysis. This is a ProMax tool that worked on the premise that the 5 to 8 milliseconds of data following first breaks are compressional wave refractions arriving at near vertical incidence, and rotated the vertical and radial component traces so as to maximize the first break energy on the vertical channel. Compressional-wave reflections that arrive later are assumed to have the same sense of particle displacement as the compressional-wave refractions, and also would be maximized on the vertical channel. Shear waves have an orthogonal sense of displacement to the compressional waves, so this rotation maximized

converted-wave reflections on the horizontal channels. The radial and transverse channels were then rotated until the remaining first break energy was maximized on the radial channel. Any energy that cannot be projected onto either the vertical or radial channel is left on the transverse channel.

Figures 3.8 and 3.9 demonstrate the results of 3-component rotation on data from the 18m depth geophone of receiver station 151. The data have been filtered with a 15-25-110-130Hz bandpass filter followed by a 500ms AGC. Figures 3.8 (a), (b) and (c) are the pre-rotated vertical, transverse and radial channel common receiver gathers respectively. The gray lines highlight a  $P$ - $P$  reflection on the vertical channel receiver gather. These lines are copied onto the radial and transverse channels, and show that the  $P$ - $P$  reflection also appears on these horizontal channels. This is a mode-leaked event. After three-component rotation (Figure 3.9), converted-wave energy is concentrated on the radial channel.

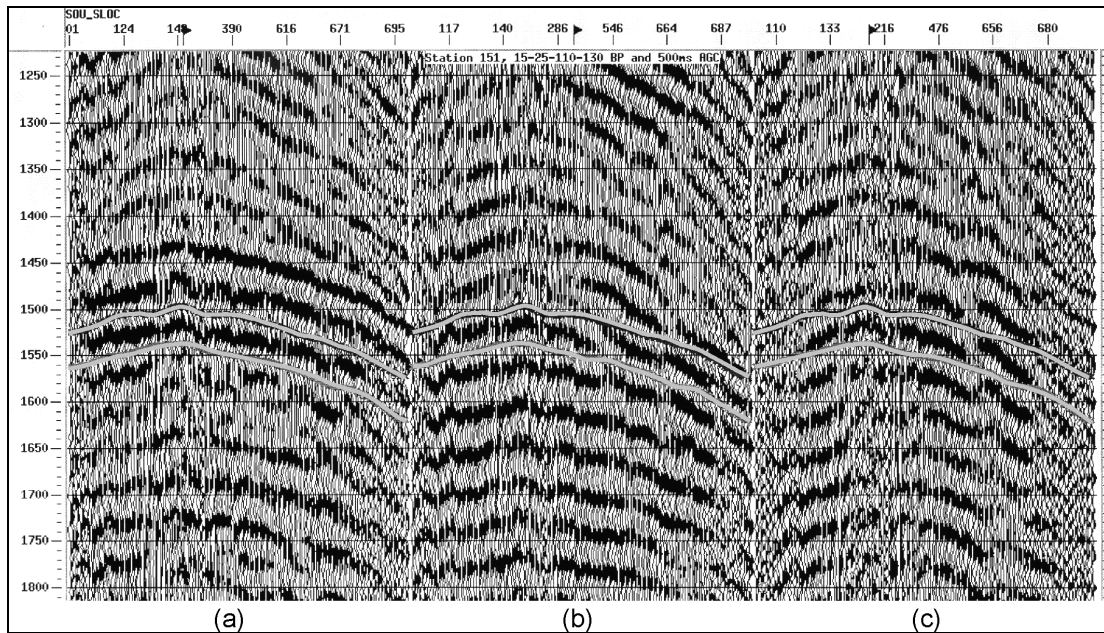


Figure 3.8. Pre-rotated common receiver gathers for a buried geophone. (a) Vertical channel; (b) transverse channel, (c) radial channel. A  $P$ - $P$  reflection, between the gray lines on the vertical channel, also appears on the radial and transverse channels. This is mode leakage.

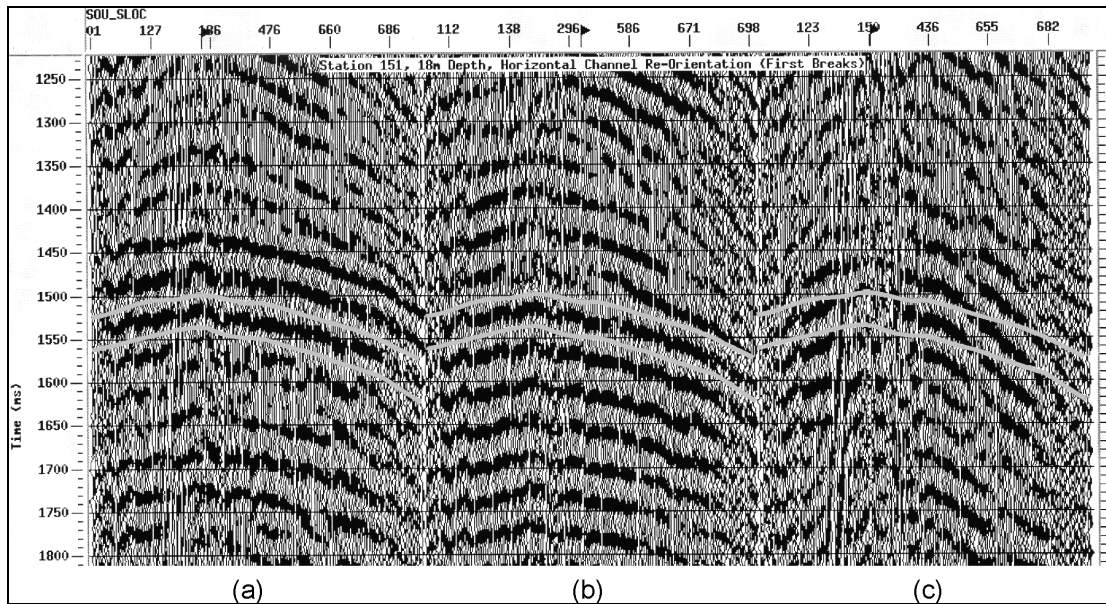


Figure 3.9. Same as Figure 3.8 after three-component receiver re-orientation. Mode leakage has been effectively removed, and converted-wave reflections appear clearly on the radial channel.

The receiver re-orientation tool reduced mode leakage on only a few buried geophones; normally it was found to have a nominal or even detrimental effect on the data. The tool also tended to reverse the polarity of many traces, making it necessary to correct the polarity manually, which was a time-consuming process. Where the automatic re-orientation did succeed, the rotated traces were included in the processing flow.

In cases that converted waves appeared on both radial and transverse channels even after automatic receiver re-orientation was tried, the traces were simply summed to produce a single “horizontal channel” trace for processing. Previous work in the area had not detected any shear wave splitting, so summing the horizontal components should not degrade converted-wave reflections.

#### 3.4.2.3. *Calculation of Receiver Statics*

Receiver statics are of key importance in processing converted-wave data. Typically, the near-surface layer is much thicker for shear waves than compressional waves as shear wave velocities are relatively unaffected by the water table (Figure 3.10). Consequently, shear wave statics are almost always larger than compressional wave statics, sometimes by over an order of magnitude (Lawton and Harrison, 1992). This

means that, in converted-wave processing, receiver statics are usually larger than shot statics and the two correlate poorly. Many static correction tools (such as elevation statics) in current commercial seismic data processing software assume that the shot and receiver statics are about the same magnitude and correlate to some degree, and so derive a poor static solution for the converted wave. Furthermore, receiver statics may be larger than the dominant period of the converted-wave reflections, resulting in serious cycle-skip errors when calculated by residual static algorithms.

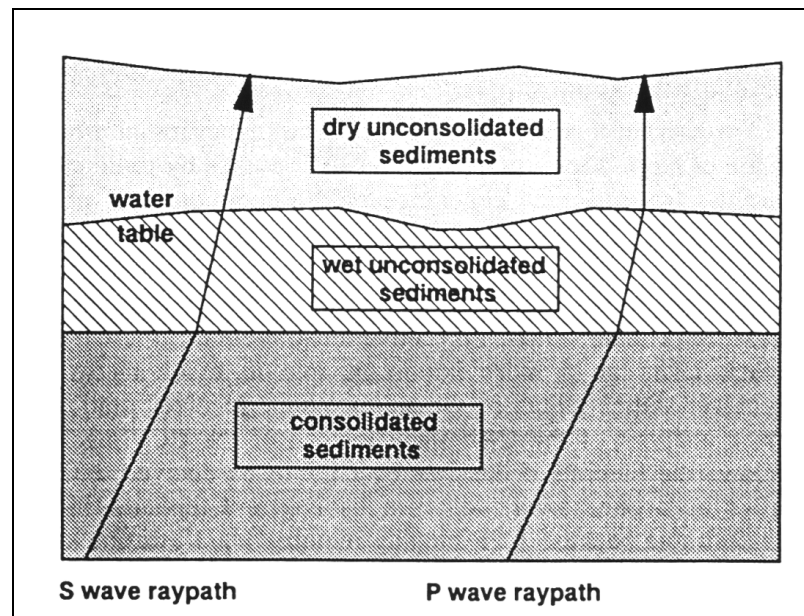


Figure 3.10. The near-surface layer is thicker for  $S$ -waves than  $P$ -waves because  $S$ -waves are relatively unaffected by the water table (from Cary and Eaton, 1993).

In order to make conventional static tools effective for converted-wave data, receiver statics must first be resolved independently from shot statics using a separate method. Assuming that the majority of the static for a given trace is receiver static (much greater than the shot, structure and residual NMO statics combined), then an initial receiver static estimation can be made by aligning reflections on common receiver stacks (Cary and Eaton, 1993).

Figure 3.11(a) shows common receiver stacked traces for the 12m radial channel data. Each trace has a fold of 144. Reflector continuity is poor (arrow), due to large receiver statics. Continuity improves after a reflection peak is aligned with hand statics

(Figure 3.11(b)). First, a peak (or trough) of the same reflection is picked across all the traces with the horizon picking tool. Then the average time of all the picks is subtracted from each individual pick, and applied to the traces as a static shift. Another iteration was sometimes required for the optimal hand static solution.

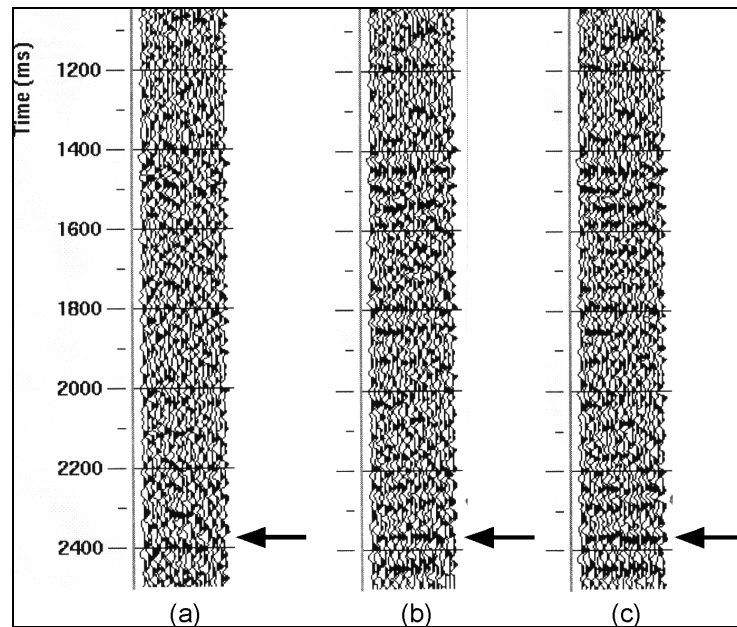


Figure 3.11. (a) Raw radial channel common receiver stack of the 12m depth geophones. (b) Hand statics improves reflector continuity (arrow). (c) Improved overall continuity results when event alignment follows hand statics.

Hand statics are limited in that they tend to best align one particular reflection. Reflections elsewhere may not be aligned optimally, due to noise at the location of the horizon pick. The ideal static would align not just a single reflection at a discrete time, but all the reflections across a large time window. This was done using the event alignment tool. This tool worked by first stacking together a user-defined number of traces from the hand-aligned receiver stack to create a model trace. Then it correlated the model trace against each trace in the section over a user-defined time window. The time of maximum correlation of each trace with the model trace was applied as a static correction. Figure 3.11(c) shows the receiver stacked traces after event alignment for reflections between 200 and 2400ms. Reflected events exhibit improved continuity compared to hand statics alone (Figure 3.11(b)).

At this point, receiver statics were resolved sufficiently to produce a brute stack, after which residual statics were calculated, followed by phase shift migration.

#### 3.4.2.4. *Radial Channel Processed Sections*

The fully processed *P-S* sections for all geophone depths appear in Figures 3.12 and 3.13. The surface data have the highest data quality for reasons discussed in the previous sections.

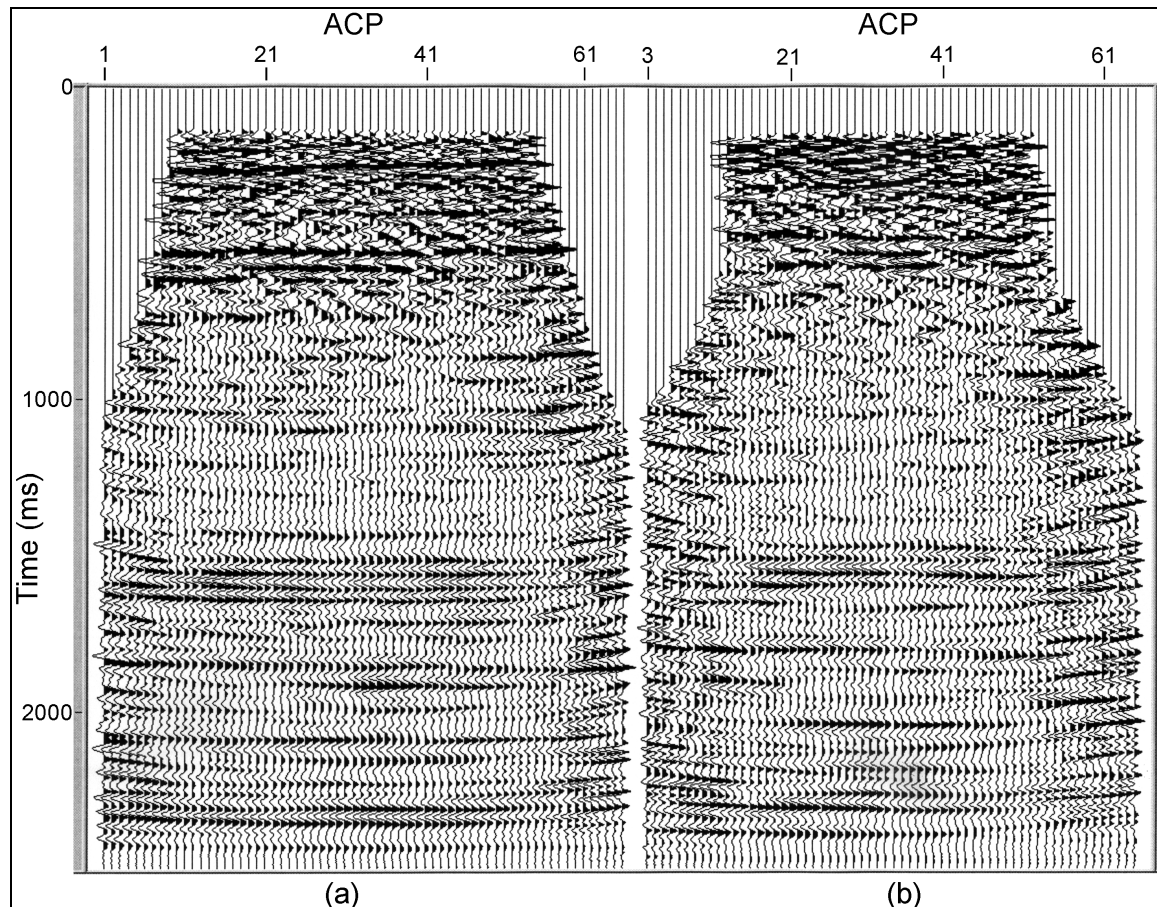


Figure 3.12. Fully processed radial channel data from (a) surface geophones, (b) 6 meter depth geophones.

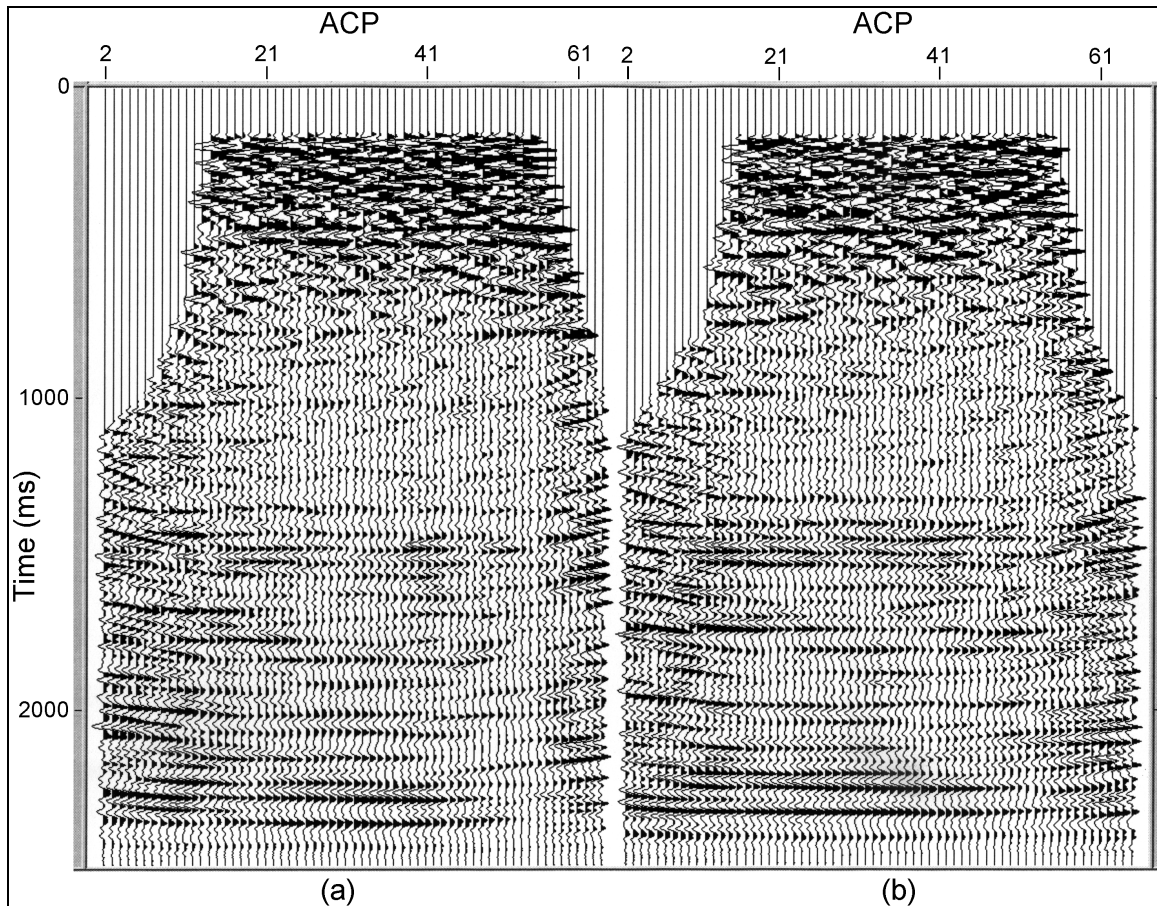


Figure 3.13. Fully processed radial channel data from (a) 12 meter depth geophones, (b) 18 meter depth geophones.

### 3.5. Frequency Analysis

If the near surface is attenuating the signal measurably, it is possible that this attenuation varies along the receiver line. Margrave (1995), for example, found  $P$ - $P$  signal bandwidth changed along the profile of a nearby 2-D survey. It is also possible that the shallower geophones will have a more attenuated signal than deeper geophones, particularly for the converted wave, for reasons mentioned in the introduction.

Prior to frequency analysis, the signal was enhanced by passing the data through an  $f$ - $k$  filter that suppressed ground roll, refractions and incoherent noise. Pad (*i.e.* zero-value) traces were first inserted into the receiver gathered data to keep trace spacing at an even 20 meters, as there were some skipped and skidded shots in the survey, and  $f$ - $k$  filtering works best when spatial sampling is constant or nearly so. For the vertical data,

the filter operator had dimensions  $500\text{ms} \times 50$  traces, with a value of 95% used for time ramp flattening and offset ramp flattening, and a 90% flattening prior to f-k filter windowing. The f-k polygon filter accepted frequencies between 6 and 95Hz, and absolute velocities higher than 2300m/s. The radial data filter parameters were similar, with the exceptions that operator dimensions were  $750\text{ms} \times 100$  traces, and that the f-k polygon accepted frequencies between 2.78Hz and 55.9Hz and absolute velocities greater than 3700m/s. These parameters were observed to best isolate the converted-wave signal.

*P-P* reflections between 1 and 2s were found to be strong for the f-k filtered data, except at very near offsets where they have been obscured by ground roll. For the vertical channel frequency analysis, therefore, the full range of offsets was used. *P-S* reflection amplitudes were only strong for mid- to far-offsets owing to weak mode conversion at near offsets, so only offsets greater than 600 meters are used in the *P-S* frequency analysis.

As previously mentioned, signal bandwidth may depend on location along the receiver line *and* receiver depth. The relationship between frequency content, receiver location and receiver depth for all geophones in this experiment was depicted more clearly by plotting the spectra data in three dimensions with contour plotting. For every receiver gather of a given depth, a Matlab computer program calculated a separate frequency spectrum in the appropriate time window. It then inserted the frequency spectra columnwise into a matrix in receiver station order. The columns of the matrix represent location along the receiver line; the rows represent frequencies from zero to Nyquist; and each individual cell contains decibels below maximum amplitude of the frequency spectra. The program then displayed the matrix as a colour contour plot with the appropriate colour bar and axes labels.

### 3.5.1. Vertical Channel

Figures 3.14 (a) through (d) are frequency contour plots of the vertical channel of the 18m, 12m, 6m and surface geophones respectively. The vertical white bars on some of the plots indicate data gaps due to receiver kills.

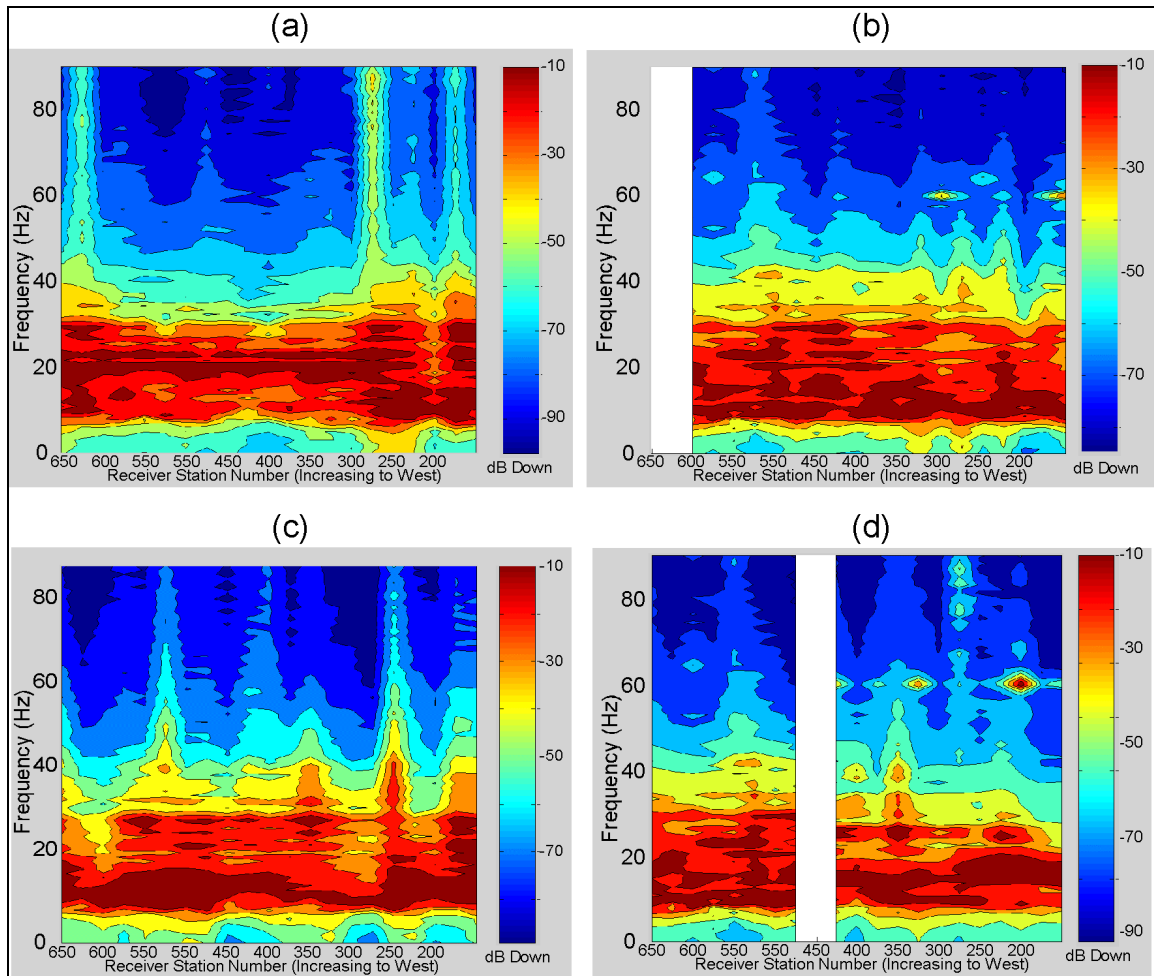


Figure 3.14. Frequency analysis of the vertical channel (a) surface, (b) 6m, (c) 12m and (d) 18m depth geophones. White vertical bars represent data gaps due to receiver kills.

Within each buried receiver line, there exist significant variations in signal bandwidth. For example, in receiver station 326 in Figure 3.14 (b), the amplitude of the signal falls to about 50 decibels below maximum at about 35Hz. The signal of the adjacent receiver gather, station 351, does not decline to 50 decibels below maximum until about 55Hz. Reflection bandwidth decreases again for station 376 to values similar to station 326. Note that this frequency variation occurs over only 100 meters of the receiver line. This pattern of adjacent geophones having significantly different signal bandwidths occurs for all depths, and is responsible for the re-entrant contours seen best at frequencies above 40Hz.

Though the frequency spectra between buried receiver lines are broadly similar, in detail there is no general pattern that holds for all depths. This indicates that the signal bandwidth patterns in the plots are not station consistent, and therefore probably not due to the effect of increasing overburden thickness attenuating the signal.

The likely controlling factor in these data is geophone coupling. As mentioned previously, the surface geophones were planted by hand and the buried geophones were planted with wooden poles. Planting by hand enabled more consistent ground-geophone coupling than can be achieved with planting by pole, because better pressure control is possible when hand-planting. This is probably why the hand-planted surface geophones show relatively less variation in bandwidth than do the buried phones.

Another indication that receiver coupling is the dominant factor in recorded signal bandwidth is the 60Hz contamination that can be seen in the 18m and 6m depth geophone plots in Figures 3.14 (b) and (d). This noise may originate from buried electrical wires and electrically powered machinery at the nearby 09-08 well, and should be fairly consistent between different geophone depths of the same receiver station. However, the 60Hz noise does not correlate between the 18m and 6m contour plots, and is nearly absent in the 12m and surface contour plots.

### 3.5.2. Radial Channel

Figures 3.15 (a) through (d) show contoured plots of the frequency spectra of *P-S* reflections for all geophone depths as recorded on the radial channel. At all depths, the *P-S* reflections have a dominant bandwidth between 8 and 30Hz, and there is very little *P-S* data at higher frequencies. Maximum amplitudes occur between 10 and 15Hz. This is a much narrower bandwidth than the *P-P* reflections, as expected.

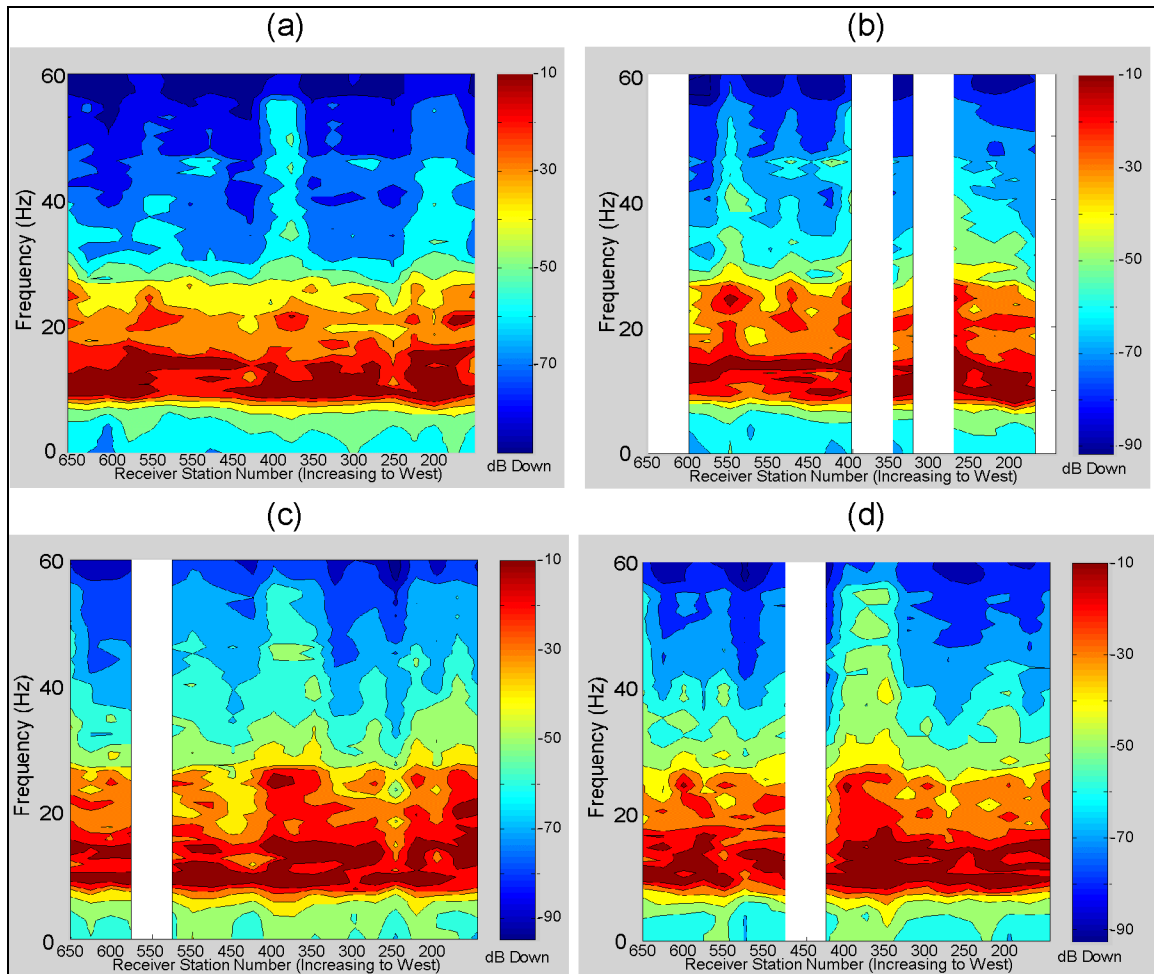


Figure 3.15. Frequency analysis of the radial channel (a) surface, (b) 6m, (c) 12m and (d) 18m depth geophones. White vertical bars represent data gaps due to receiver kills.

As was found for the vertical channel, there are considerable differences in recorded bandwidth within each buried receiver line, and these differences correlate poorly between the different receiver lines. The surface receiver line does not have as great a variation in bandwidth as the buried lines. Again, these observations probably indicate variations in geophone coupling.

There appears to be no systematic improvement of  $P$ - $S$  bandwidth with depth. Any improvement in  $P$ - $S$  bandwidth that might be gained by burying the geophones is compromised by poor geophone coupling.

### 3.6. Vertical Interval Velocities

Interval *P*- and *S*-wave velocities were determined by the reflection cross-correlation method described in Chapter 2.6. Any geophone interval with a vertical separation of less than two meters has been excluded from this analysis, because events arrive too closely in time to provide a reliable determination of velocity.

#### 3.6.1. *P*-Wave Velocities

The time lags determined through trace cross-correlation produced a large range of vertical velocities for approximately two-thirds of the intervals between buried geophones. In certain buried groups, the *P-P* reflection appears to arrive at shallower depths slightly earlier than at greater depths, resulting in negative apparent velocities (the fact that some “18 meter” depth geophones were actually shallower than the 12 meter geophones has been accounted for in these calculations). It is concluded that the geophones may be affected by a “local static”, which is a time delay caused by low-velocity mud surrounding certain geophones but not others.

*P*-wave interval velocities between buried and surface geophones yield more consistent and reasonable results (Figure 3.16). For the western two-thirds of the receiver line, the *P*-wave velocity for the top 18m of overburden is about 1000m/s. Then there is a sharp increase in *P*-wave velocity between stations 301 and 226 to values more typical of consolidated sedimentary rock. This likely indicates a thinning of the overburden layer in this area. Velocities peak to an unphysically large value for station 201, and decline east of this station to values more typical of weathered bedrock.

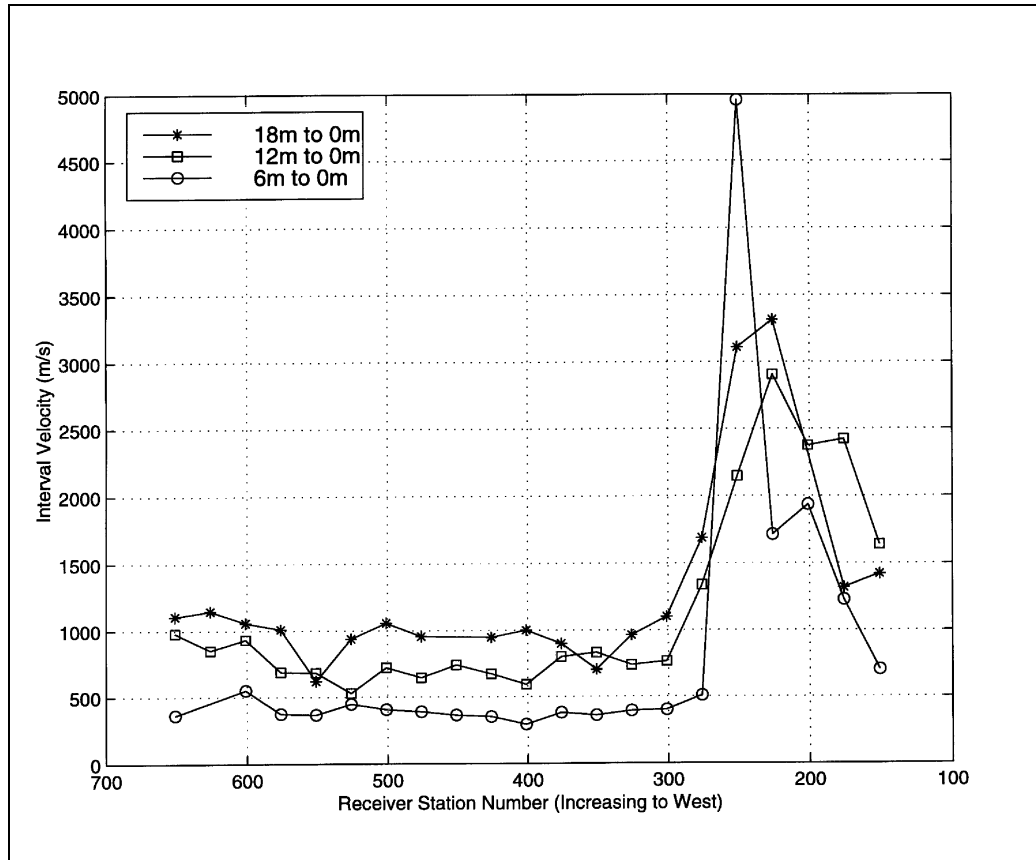


Figure 3.16. *P*-wave interval velocities between buried and surface geophones.

The surface to 12m interval velocities show the same general trend as the surface to 18m interval, but this interval has a lower velocity on average. The western two-thirds of the receiver line has a fairly consistent interval velocity of about 700m/s, followed by an increase to nearly 3000m/s within the eastern third. Past this point, velocities taper to about 1600m/s. Again, this indicates that the eastern third of the line has a thinner overburden layer than the western two-thirds. Velocities between the surface and 6m depth again follow a similar trend, averaging about 400m/s for the western two-thirds and peaking to just under 2000m/s within the eastern third of the receiver line. The anomalous value of 5000m/s for one station is probably not meaningful, and may be due to a “local” static due to low-velocity mud surrounding that geophone as discussed previously.

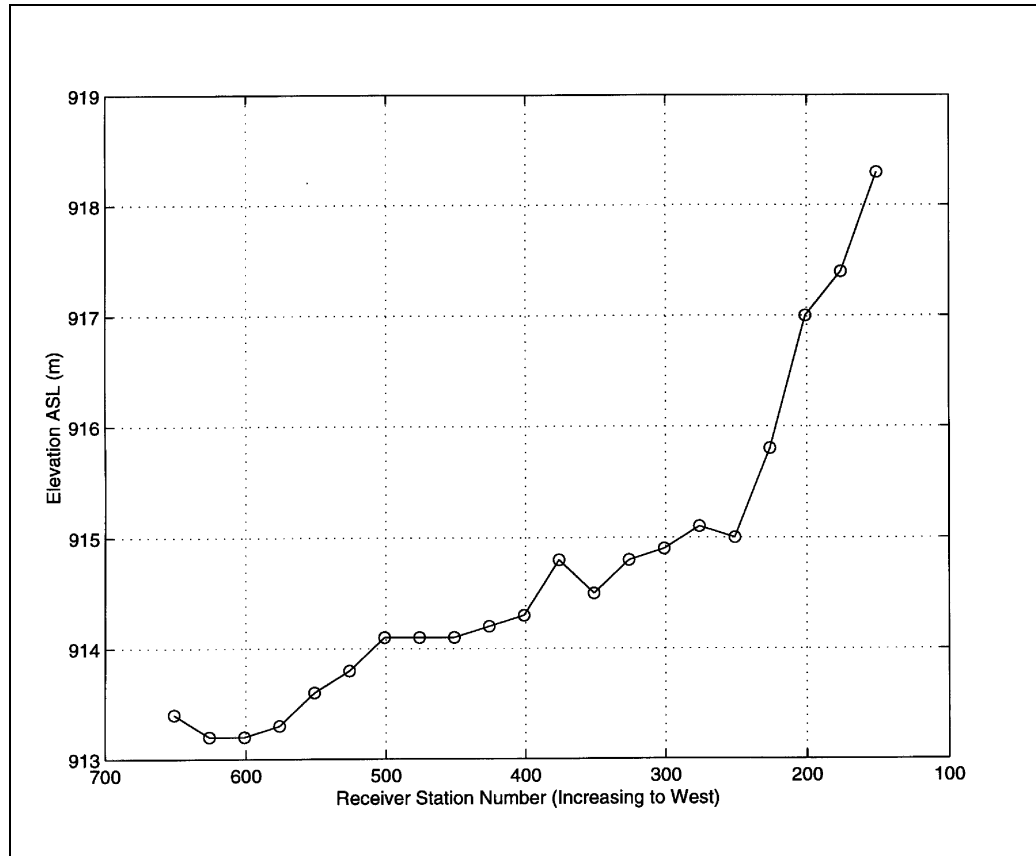


Figure 3.17. Receiver elevations above sea level.

These observations have some correspondence to receiver elevation (Figure 3.17). There is a fairly steady elevation rise of about 0.2 meters per station across the western two-thirds of the receiver line, followed by a much sharper elevation rise for the remainder of the line. The interval velocities peak at the point where the elevation gradient is greatest. This is demonstrated more clearly in Figure 3.18, which shows receiver elevation differences between stations from west to east. The steepest slope corresponds to the points of highest buried-to-surface geophone interval velocities. This implies that the overburden layer is thinnest at the elevation inflection point, and somewhat thicker on either side of this. Figure 3.19 shows an interpreted velocity model of the near surface that is consistent with these observations.

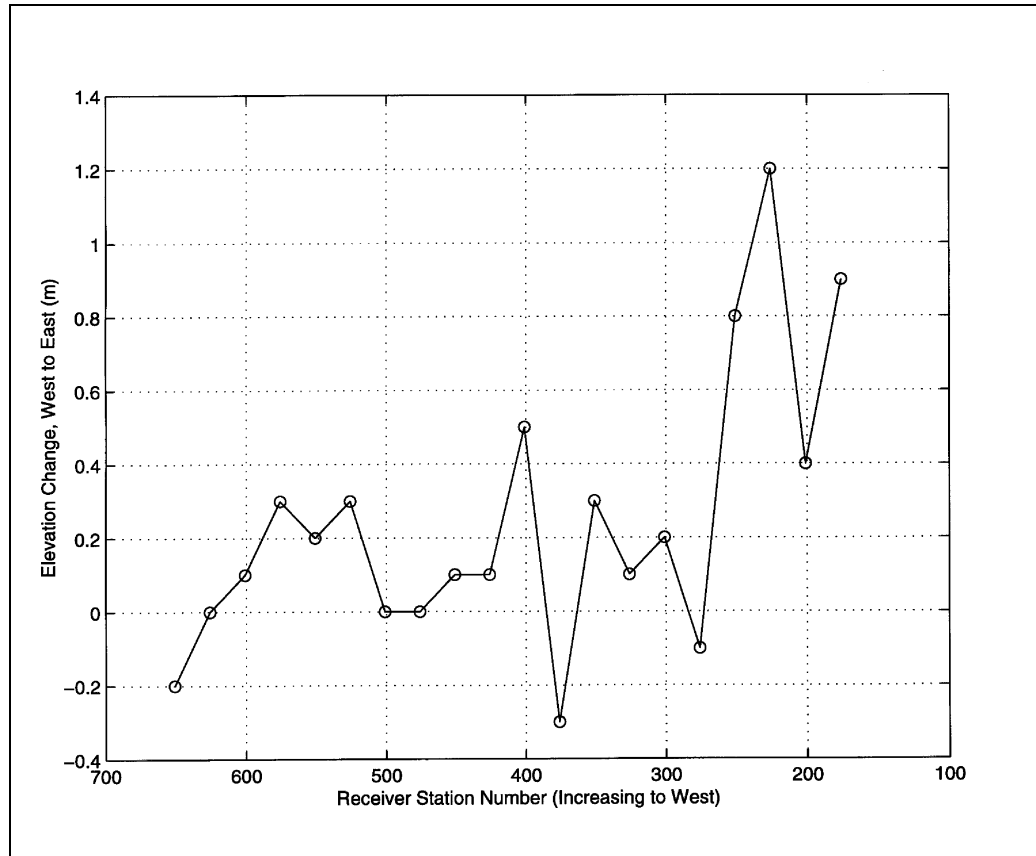


Figure 3.18. Elevation difference between adjacent geophone stations.

### 3.6.2. S-Wave Velocities

As previously mentioned, *P-S* reflections recorded by the buried geophones had very low signal-to-noise ratios. This initially resulted in poor correlation values and inconsistent time lags for converted waves ascending through the near-surface layer. Signal-enhancing f-k filters did not improve correlation values for sufficiently confident shear-wave interval lag times.

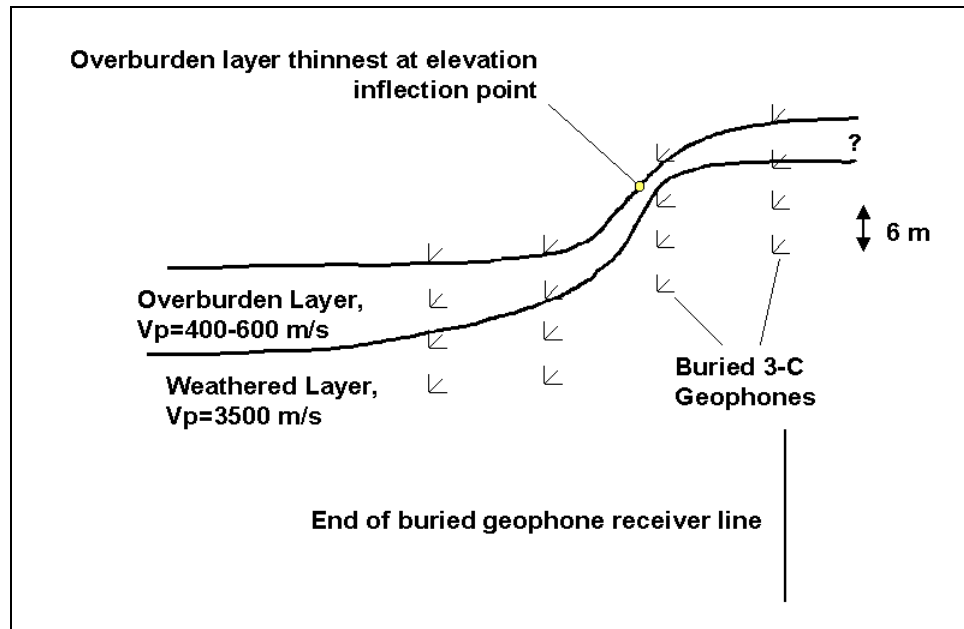


Figure 3.19. Near-surface velocity model based on  $P$ -wave vertical interval velocities.

This problem was resolved by boosting signal-to-noise ratios through trace stacking. Each radial channel receiver gather was corrected for normal moveout with the same  $P$ - $S$  velocity function, with no statics applied. The traces were muted with top and bottom mutes, and then stacked to produce a single stacked trace for each radial receiver. The stacked traces had a maximum fold of 142, which would (optimally) reduce incoherent noise by a factor of nearly 12. An additional advantage to stacking is that it tends to reduce  $P$ -wave energy that has leaked onto the radial channels. This is due to the trailing-spread polarity reversal that has been applied to the traces, which causes  $P$ - $S$  events to reinforce during stacking and  $P$ - $P$  events to cancel.

Interval time lags were calculated by cross-correlating the receiver stacked traces of different geophone depths across a time window of 1300 to 2500ms. This time window contains the zone of interest as well as many other strong  $P$ - $S$  reflections. The resulting peak correlation values are higher with the stacked traces versus the individual traces of the contributing receiver gathers, and more confident  $S$ -wave interval times result.

Figure 3.20 shows the shear wave interval velocities between buried phones. The 12m to 6m shear wave velocities average 185m/s in the western two-thirds of the line,

and decrease to an average of 150m/s for the remainder of the line. The 18m to 12m interval has velocities that are over 150m/s higher on average than the 12m to 6m interval, but its velocities are far more variable. This may indicate a complex surface of the weathering layer at these depths. The 18m to 6m interval, which encompasses the previous two intervals, shows the same general decrease in velocities toward the east as the 12m to 6m interval, but with highly variable velocities as seen in the 18m to 12m interval. Ideally, the 18m to 6m interval velocity should fall about midway between the 18m to 12m and 12m to 6m interval velocities, but this would only be true if the 12m phone was located exactly midway between the 18m and 6m phone, which was rarely the case (Figure 3.4).

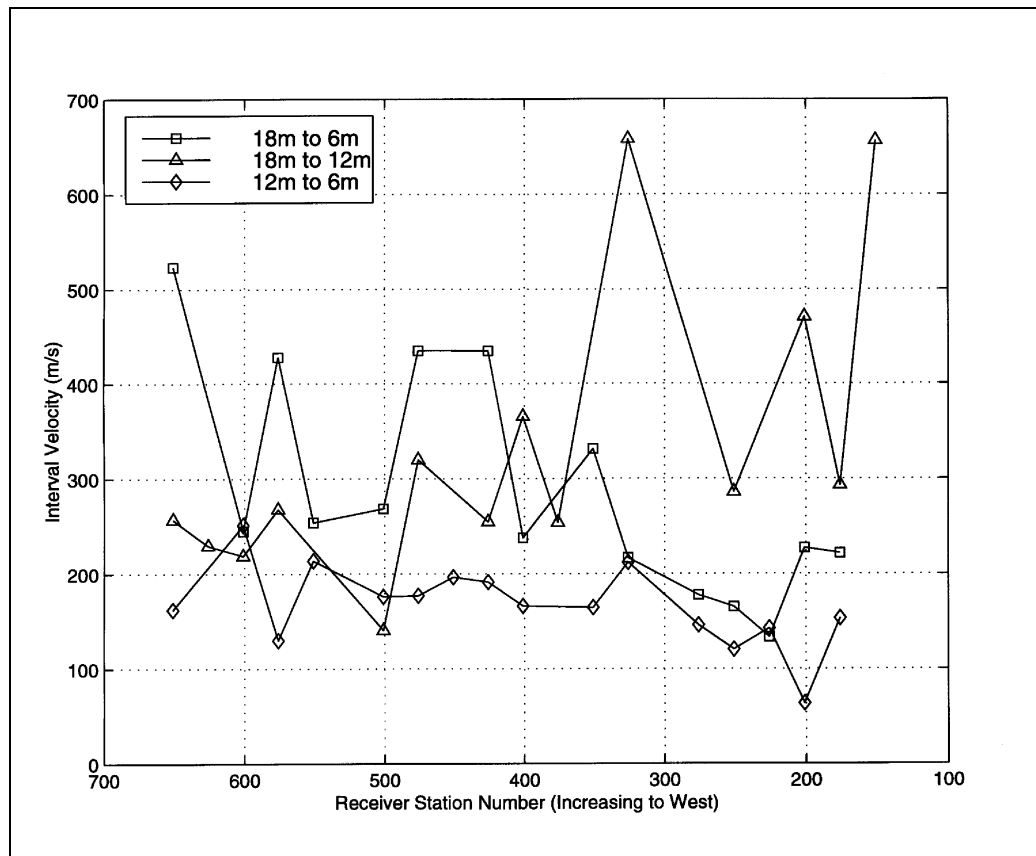


Figure 3.20. Near-surface shear wave velocities for buried-to-buried intervals.

Figure 3.21 shows interval velocities between surface and buried phones. The surface to 18m depth has an average shear-wave velocity of 193m/s. There is a peak in

velocities between stations 501 and 476, and a drop between stations 301 and 176. The surface to 12m interval has an average velocity of about 148m/s, with a general west-to-east decline in velocities until station 201. East of this station, velocities increase rapidly to almost 200m/s. The surface to 6m interval has shear wave velocities that correlate very well to the surface to 12m interval, and are on average about 20m/s lower.

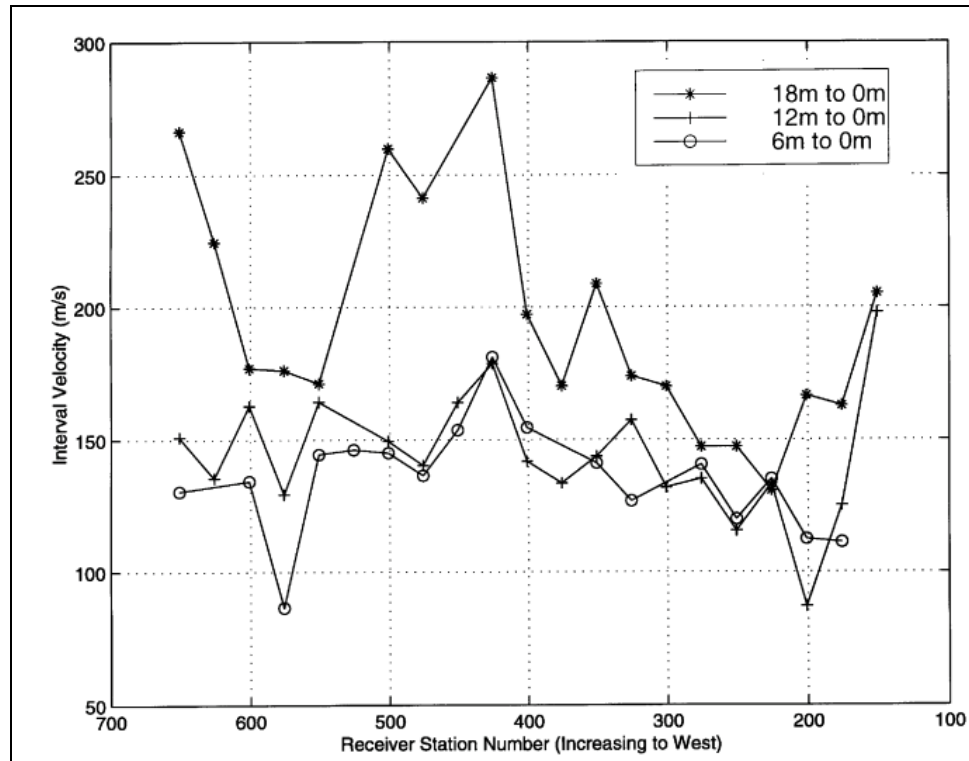


Figure 3.21. Near-surface shear wave velocities for surface-to-buried intervals.

Most of the profiles show a general decrease in shear-wave velocities from west to east across the receiver line, reaching a minimum between stations 201 and 301. East of this area, velocities increase somewhat. The velocity profile has a crude negative correlation with elevation for the western two-thirds of the receiver line. This may be due to a change in overburden sediment types across the receiver line that have different shear-wave velocities, either inherently or due to differential weathering.

### 3.6.3. $V_p/V_s$ Analysis

As expected, the  $P$ - and  $S$ -wave velocity profiles of the near surface do not correlate well. While  $P$ -wave velocities peak dramatically between stations 151 and 301,  $S$ -wave velocities actually decline slightly in this interval.

The resulting  $V_p/V_s$  plots for surface-to-buried geophones (Figure 3.22) show that the  $V_p/V_s$  is fairly constant between stations 151 and 301. The top 6m has an average  $V_p/V_s$  of 2.8 in this region, the top 12m has an average  $V_p/V_s$  of 5.1 and the top 18m of the near-surface layer has a  $V_p/V_s$  of 4.7. The increased  $V_p/V_s$  for the deeper intervals probably indicates that the intervals contain the water table. East of station 301,  $V_p/V_s$  becomes unphysically large; values over 20 have been excluded from the plot. The large  $V_p/V_s$  values between stations 301 and 176 occur due to high  $P$ -wave velocities (Figure 3.16), and not due to a drop in  $S$ -wave velocities.

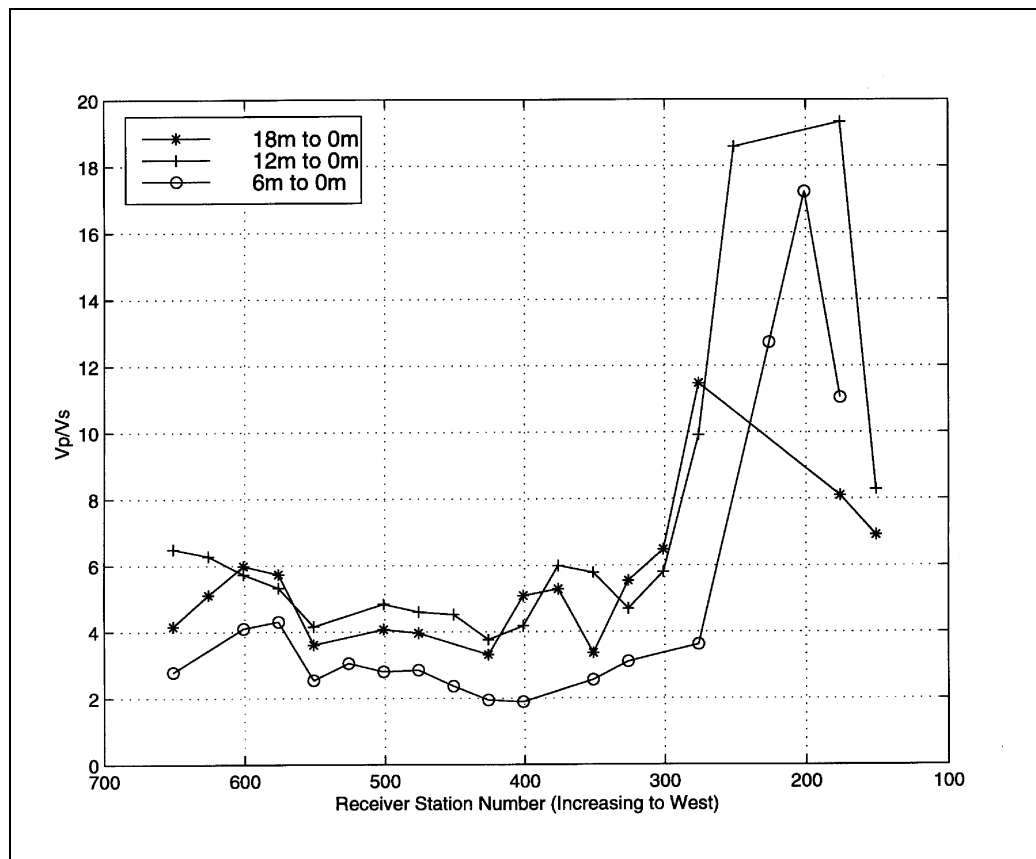


Figure 3.22. Vertical interval  $V_p/V_s$  for surface to buried intervals.

### 3.7. Similarity of Processed Sections

Although the processed sections are visually similar, their similarity can be determined using trace differences, cross-correlations, and mean square difference. The receivers of a given buried geophone station are only a few meters apart, and so record essentially the same wavefield. Since data from the four geophone depths were acquired simultaneously and processed using the same flow, their similarity should be controlled by the effects of burial on recorded signal and random noise.

#### 3.7.1. Trace Differences

A simple and direct way to determine the similarity of two seismic sections is to take their difference; this is the usual procedure in time-lapse seismic studies. Before sections can be subtracted from each other, their reflected data must be aligned as precisely as possible. The completely processed sections had residual static differences of up to 20ms, because reflections arrived at deeper geophones first, and these time differences carried through to the final stack. Trace pairs (*i.e.* the same CDP trace from two different sections) to be subtracted were first cross-correlated across a portion containing strong reflections. The time lag of the peak value of the resulting correlogram was then applied as a trim static to one of the traces, which aligned the reflections precisely. Then the trace from the deeper geophone was subtracted from the trace of the shallower geophone. The procedure was repeated for all traces in the sections to be compared, resulting in a “difference section”.

Figure 3.23 shows the *P-P* data from the 12m stacked section, the 6m stacked section, and their difference as determined by the above method. There is strong signal in the stacked sections, but almost nothing in the difference section, indicating that the reflected data is virtually the same. The linear noise in the difference section may be the branches of off-line diffractions caused by irregularities at the top of the bedrock (the apices of the diffraction hyperbolae do not stack constructively (Larner *et al.*, 1983)). They are present in both input sections, but become more noticeable with the high-amplitude reflections removed. Similar results were found for other stack differences, indicating a high degree of repeatability for the buried geophone experiment.

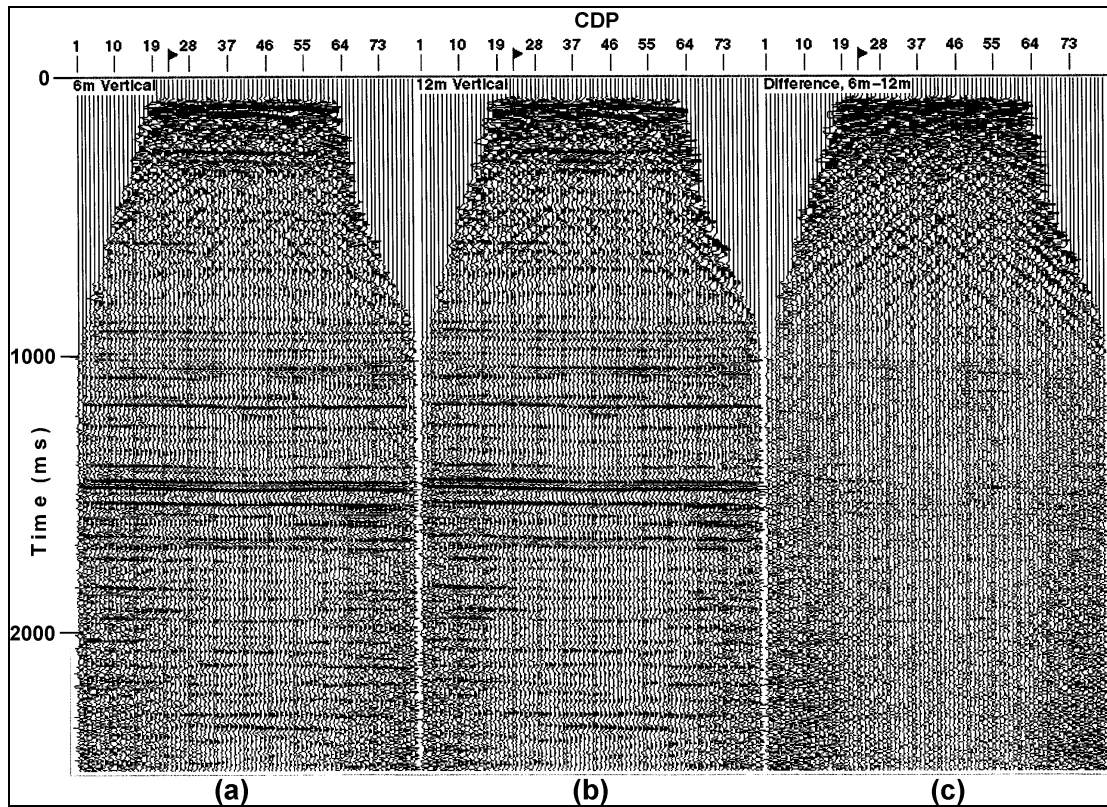


Figure 3.23. The (a) 6 and (b) 12m geophone depth  $P$ - $P$  stacked sections, and (c) their difference, which is mostly random noise.

The identical procedure was applied to the  $P$ - $S$  data. Figure 3.24 shows an example of the surface and 12m  $P$ - $S$  stacked sections, and their difference. The trace subtraction removes most of the signal, leaving essentially random noise in the difference section. This was found for other  $P$ - $S$  difference sections as well. The linear noise at early times did not emerge as strongly on the difference sections of the radial channel data as it did on the vertical channel data. This indicates that the diffracted energy was composed chiefly of compressional waves with a mostly vertical sense of particle displacement, as expected.

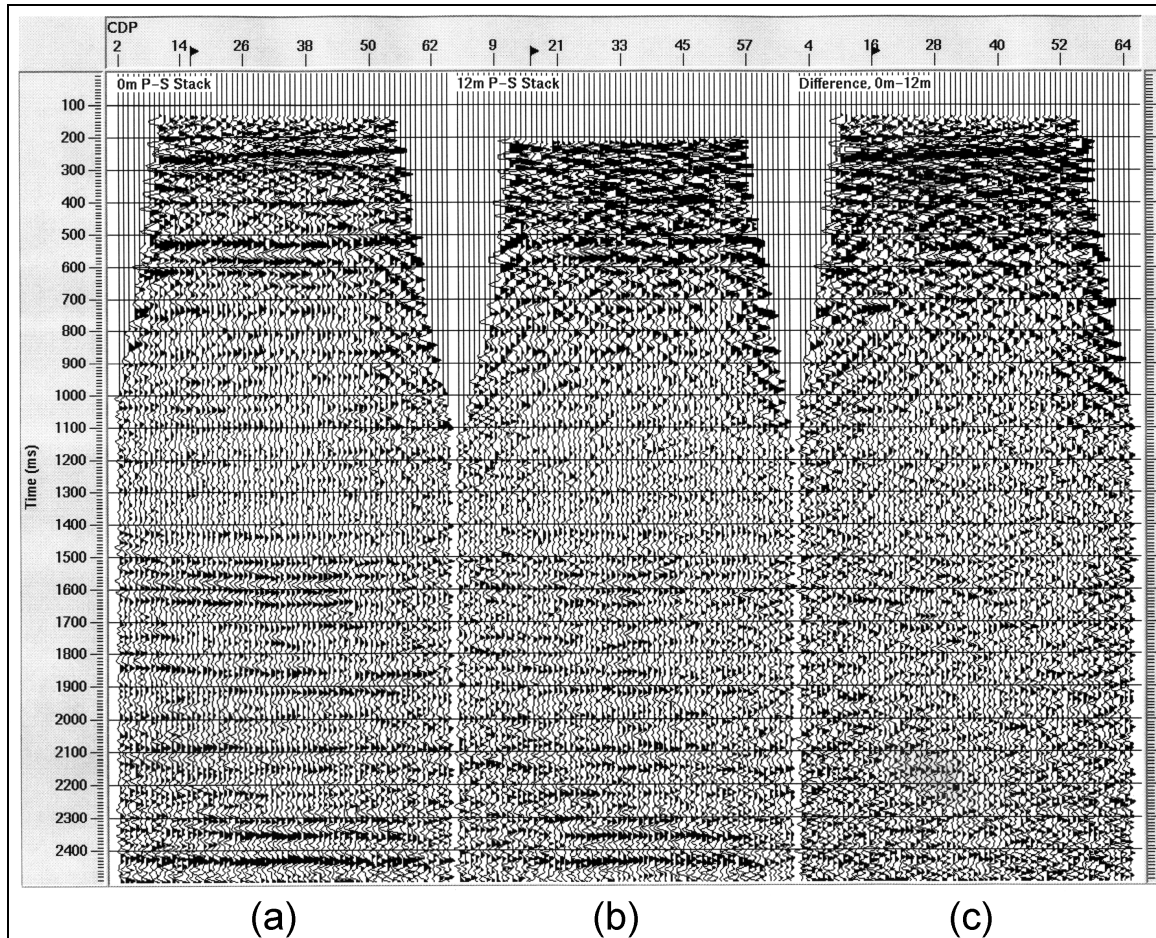


Figure 3.24. The (a) 0 and (b) 12m geophone depth  $P$ - $S$  stacked sections, and (c) their difference.

### 3.7.2. Cross-correlations

Cross-correlation values were calculated with the same Matlab computer function that was used to obtain interval lag times for trace differencing (see previous section). Both stacked and migrated sections were analyzed as it has been previously demonstrated that migration can improve repeatability (*i.e.* correlation) in time-lapse seismic studies (Porter-Hirsche and Hirsche, 1998).

#### 3.7.2.1. Vertical Channel

Cross-correlation values for the  $P$ - $P$  data were calculated in the 900-2000ms time window, as this region contained the zone of interest plus numerous other strong, clear

reflections. Results using other time windows of different sizes were virtually the same, so this window can be viewed as representative of most of the section.

Figure 3.25 shows peak correlation values between all depths of the *P-P* stacked and migrated sections. For clarity, results from the six comparisons are displayed on two separate plots. Overall, the stacked sections (Figures 3.25 (a) and (b)) correlate well to each other, achieving coefficients of over 0.9 in places. Correlation values are much the same for all comparisons, indicating that no two sections are particularly dissimilar. Maximum cross-correlation values are highest at the central, high fold portions of the stacks, taper off slowly towards the edges of the section, and drop off sharply at the very edges. This pattern corresponds to fold (Figure 3.5(a)), which decreases from the center of the stacked sections. The very pronounced decrease in correlation at the edges occurs where the fold drops to below about 12. Since signal-to-noise ratio is proportional to fold, much of the observed correlation patterns in Figure 3.25 can be attributed to non-correlatable random noise in the data.

The migrated sections (Figures 3.25 (c) and (d)) have higher maximum cross-correlation coefficients than the stacked sections, both on average (Figure 3.26) and by peak value. Correlation values are fairly consistent through the central four-fifths of the migrated sections; the stacked sections for the same region show a gradual decrease toward the edges. At the very edges, correlation values taper moderately to a minimum of about 0.7, which is much larger than the comparable value for the stacked sections. The results clearly demonstrate the noise-suppressing effects of migration, which is particularly acute for the low fold regions of a section. Migration not only improves signal-to-noise ratio, but also balances it better throughout the whole section. Figure 3.26 shows that while migration improves absolute similarity between sections, it does not change their relative similarity.

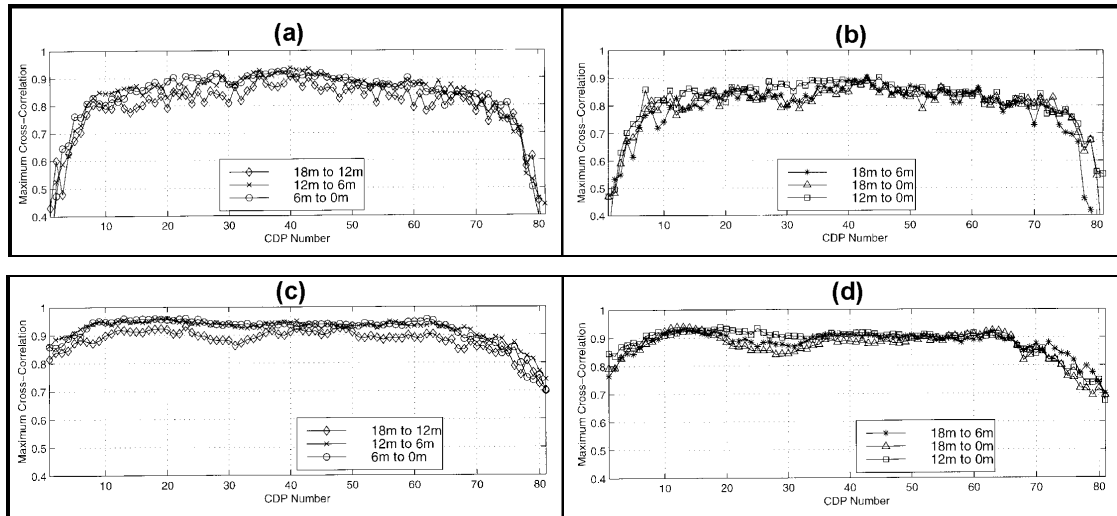


Figure 3.25.  $P$ - $P$  section correlation analysis for the stacked sections [(a) and (b)], and migrated sections [(c) and (d)].

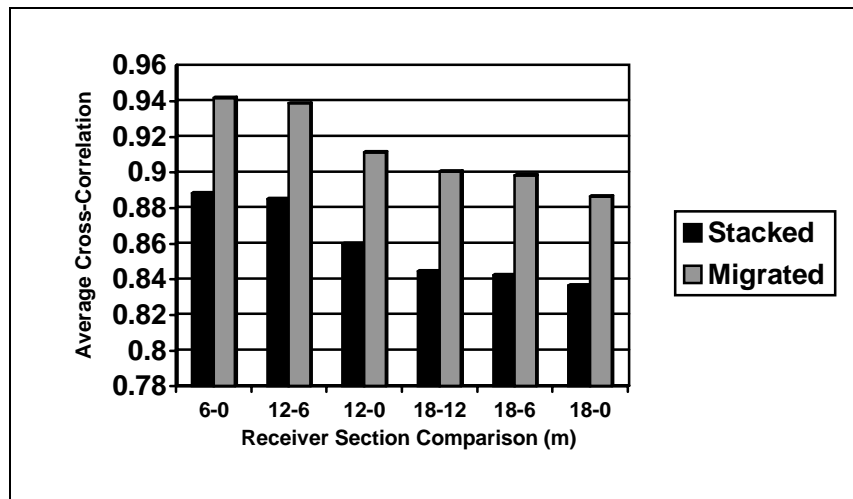


Figure 3.26. Average cross-correlation values of the  $P$ - $P$  stacked and migrated sections for CDPs 15 to 65. Time window is 0.9 to 2.0 seconds.

Figure 3.26 reveals several patterns in section similarity. A relation exists between relative depth of two sections and their similarity; groups separated by 6m have greater similarity than groups separated by 12m, which in turn are more similar than groups separated by 18m. There is also a tendency for shallower sections to be more similar to each other than deeper sections. Thus the 6m and surface sections are more similar than the 6m and 12m sections, which in turn are more similar than the 12m and 18m sections, even though each section is separated by 6m.

Random noise levels are undoubtedly a factor in these results. Reflection amplitudes display a clear relation to depth, as the near surface acts as a natural signal amplifier (Chapter 4). This would result in better signal-to-noise ratios for shallower geophones, which would tend to increase correlation values. Therefore, the deeper sections correlate more poorly than the shallower sections because they contain more random noise. The tendency of sections that are closer spatially to have higher correlation may be due to the similarity of receiver notches in the frequency spectra (Chapter 4), though this is not evident from the frequency spectra of the raw or stacked data.

### 3.7.2.2. *Radial Channel*

A time window of 1000 to 2200ms was used to calculate the radial channel cross-correlation values, which contained abundant *P-S* reflections. Figure 3.27 (a)-(d) shows the peak correlation values for the stacked and migrated sections. Cross-correlation values are much lower for *P-S* reflections than *P-P* reflections (previous section), because the smaller reflection amplitudes result in lower signal-to-noise ratios. Figures 3.27 (a) and (b) show that correlation values peak in the central, high-fold portion of the stacked sections and taper off gradually toward the edges. There is no sudden drop-off as there was for the *P-P* data, indicating more overall consistent (but higher) random noise levels across the sections. The correlation values tend to fluctuate within this general trend, indicating a lower degree of similarity in these sections. The fluctuations become more pronounced after migration (Figures 3.27 (c) and (d)). While some correlation values increase after migration, others have become lower. Migration decreased average correlation values in half the section comparisons (Figure 3.28). This may be due to migration artifacts that correlate poorly between sections, as a consequence of poor signal to noise ratios in the stacked sections.

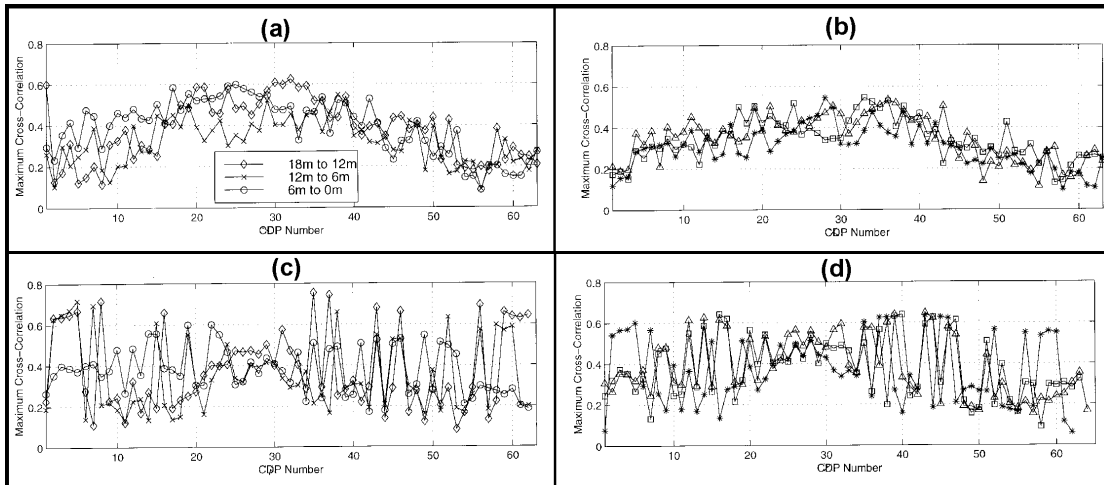


Figure 3.27.  $P$ - $S$  section correlation analysis for the stacked sections [(a) and (b)], and migrated sections [(c) and (d)].

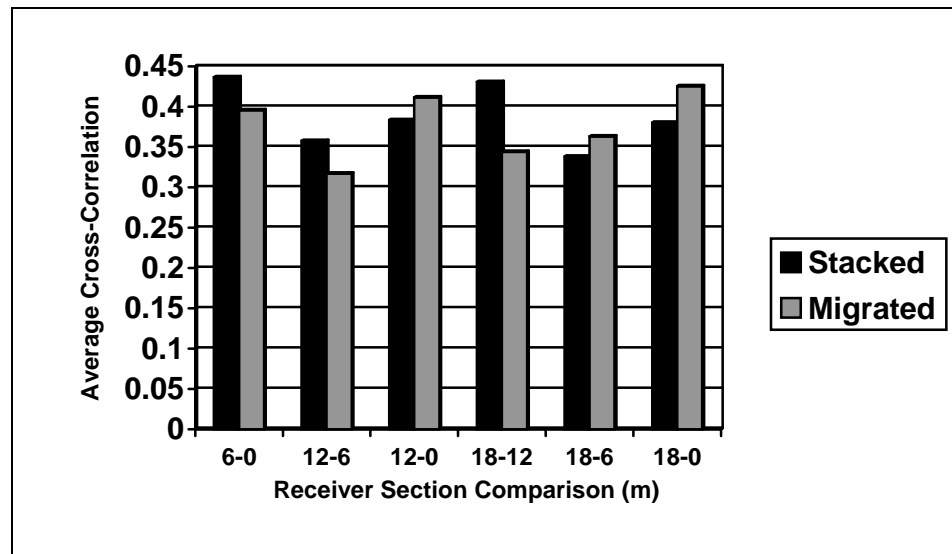


Figure 3.28. Average peak cross-correlation values of the  $P$ - $S$  stacked and migrated sections, for ACPs 10 to 55. Time window is 1.0 to 2.2 seconds.

Results from the  $P$ - $S$  cross-correlation analysis are given in Figure 3.28. Some of the same general trends seen in the  $P$ - $P$  data (Figure 3.26) also appear in the  $P$ - $S$  data. For example, the surface and 6m sections are the most similar, as they were for the  $P$ - $P$  data. Before migration, it can be seen that closer geophone intervals tend to correlate better than intervals that are more widely spaced, and sections from shallower geophones correlate better than sections from deeper ones. After migration these tendencies are not as clear, as both absolute and relative cross-correlation values between sections are not

preserved. The amplitude-depth relation for converted-waves is not as pronounced as it is for compressional waves (Chapter 4), meaning that the near surface does not amplify shear waves as much as it does compressional waves. Signal-to-noise ratios between *P-S* sections therefore do not vary as much as they do between compressional-wave sections. This is why the *P-P* cross-correlation values are related to receiver depth, whereas the relation is not as clear for *P-S* reflections.

### 3.7.3. Mean Square Difference

The mean square difference (MSD) provides a quantitative measure of trace similarity that, unlike cross-correlations, has physical meaning for seismic traces. The sample values of a trace represent varying voltages as recorded by a geophone, as it responds to varying particle velocities. Because energy is proportional to velocity squared, and power is energy per unit time, seismic trace values squared are termed the power of the trace (Sheriff and Geldart, p.286), as each sample represents a constant time unit. The mean square difference of two traces, then, is the same as the power of their difference. In contrast to cross-correlation, traces with a high MSD are less similar than traces with a low MSD; identical traces would have an MSD of zero.

*P-P* stacked and migrated sections were compared in a time window of 0.9 to 2.0 seconds; *P-S* sections were compared over a 1.0 to 2.2 second time window. The mean square difference values were averaged between CDPs 15-65 for the *P-P* data, and ACPs 15-55 for the *P-S* data. Results are shown in Figure 3.29.

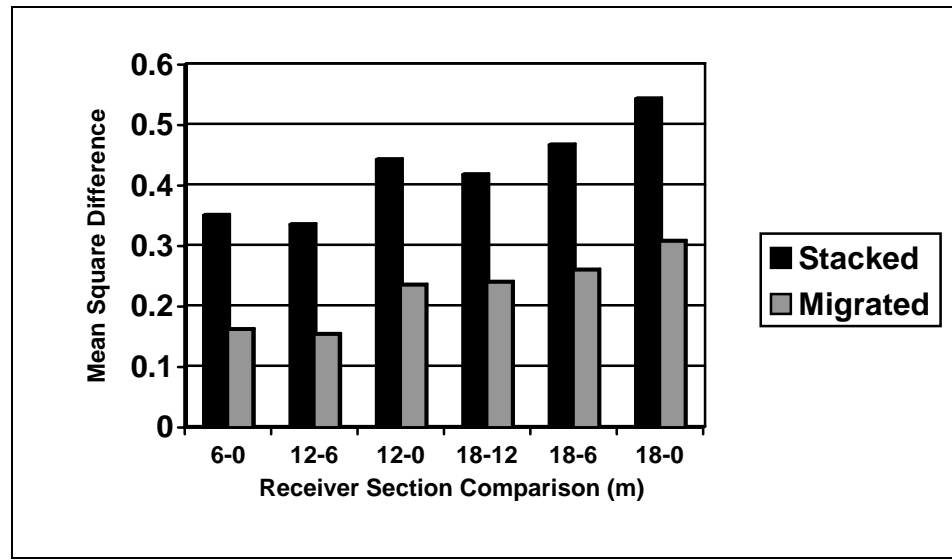


Figure 3.29. *P-P* section comparison using mean square difference.

The *P-P* MSD results were similar to those found by the cross-correlation analysis. *P-P* stacked sections that are relatively closer in depth have a strong tendency to be more similar; stacks separated by 6m are the most similar while the stacks separated by 18 meters, the least. Stacks separated by 12m are of intermediate rank. There is also a tendency for shallower stacks to be more similar to each other than deeper stacks, but this is weak. After migration, the MSD for all intervals has decreased significantly, as a result of improved signal-to-noise ratios. Two intervals that had a close MSD before migration have exchanged rank, but essentially the same observations can be made with regards to similarity of depth and similarity of section.

As anticipated, the *P-S* sections have a much higher MSD (Figure 3.30) than the *P-P* sections, as a result of poorer signal-to-noise for reasons outlined in Chapter 3.4.2. Intervals involving the surface *P-S* have the lowest MSD, particularly after migration. This is expected, as the surface data had much better data quality, which would result in lower residual noise after trace subtraction. No other tendencies are apparent.

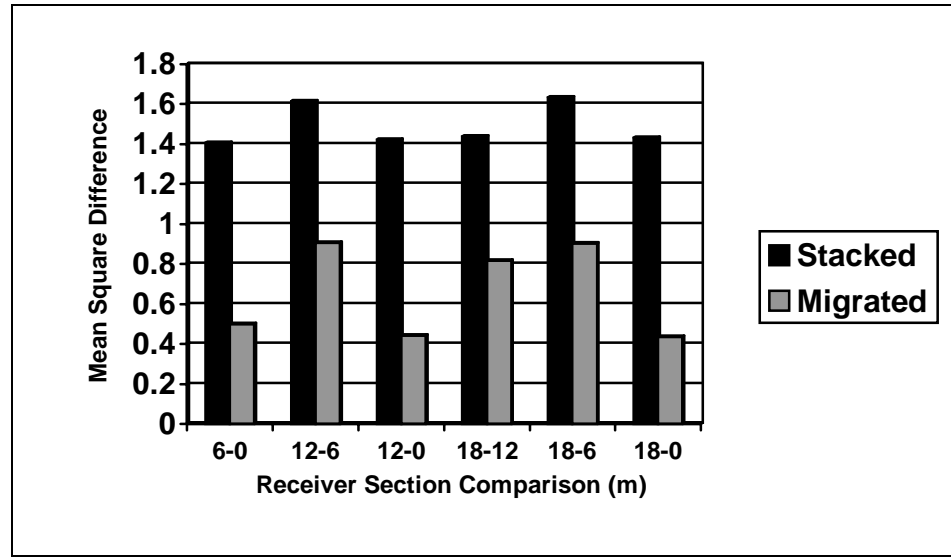


Figure 3.30. *P-S* section comparison using mean square difference.

#### 3.7.4. Synopsis

The cross-correlation and mean square difference analyses indicate that the similarity of *P-P* data is controlled primarily by relative geophone depths and secondarily by absolute geophone depth. That is, sections from closer geophone intervals tend to be more similar than sections that are farther separated, and data from shallower sections tend to be more similar than the deeper sections. The primary control may be due to receiver notching, which can be expected to be more similar for geophones at similar depth. The secondary control may be due to higher raw reflection amplitudes in shallower geophones, which would cause higher signal-to-noise ratios and hence greater similarity for data from shallower geophones.

The surface radial sections are more similar to the buried sections than the buried sections are to each other. This is likely the result of a superior signal-to-noise ratios in the surface data, as it was unaffected by problems of mode leakage and poor geophone coupling. The surface data also benefited from higher absolute reflection amplitudes. No other tendencies are clear. Random noise levels are therefore the chief factor in governing the similarity or repeatability of the *P-S* sections.

**CHAPTER 4**  
**NUMERICAL MODELING OF RECEIVER NOTCHING**  
**AND REFLECTION AMPLITUDES**

This chapter investigates receiver notching and reflection amplitudes that might be expected for buried geophones through simulations of a model wavelet propagating through a linear  $V(z)$  near-surface medium bounded on the upper side by a free surface. Reflection amplitudes due to near-surface impedance gradients are also investigated, with an  $I(z)$  near-surface impedance model, based on a linear  $V(z)$  and  $\rho(z)$ . Results are compared to data from the Blackfoot III buried geophone experiment, where reflection amplitudes from the buried geophones were found to be significantly lower than those recorded by the surface geophones.

**4.1. Receiver Notch Theory**

Wavelet cancellation or notching will occur at the depth where an incident sinusoid of wavelength  $\lambda$  is exactly half a cycle ( $180^\circ$ ) out of phase with its reflection off the surface, as  $\cos(\theta) + \cos(\theta + 180^\circ) = 0$ . The shallowest depth at which this cancellation will occur is  $z = \lambda/4$ ; this is because the sinusoid completes a quarter of a cycle to go from depth  $z$  to the surface, and another quarter cycle after reflecting down to depth  $z$  again. It is then delayed half a cycle with respect to the incident sinusoid, and will cancel it. Harmonics of the incident sinusoid will also cancel at this depth. Given a weathering layer velocity  $V_w$ , it follows that a geophone buried at depth  $z$ , will record a notch at

$$f_n = \frac{V_w}{4z} (2m + 1), \quad m = 0, 1, 2, \dots,$$

where  $f_n$  is the frequency of the notch (along with its odd-number harmonics). For a linear  $V(z)$ , the frequency of the notch is calculated by substituting  $V_w$  with the average velocity between depth  $z$  and surface, which is  $(V(z) + V_0)/2$ , where  $V_0$  is the velocity at  $z=0$ . Though convenient for determining the exact frequency of receiver notches, the formula does not indicate the character of the frequencies between notches, where partial cancellation and anti-notches are expected. Nor does it indicate how a notched spectrum of a typical seismic reflection might look. In this chapter, these further considerations are

addressed through numerical simulations to allow for a meaningful comparison to the field data.

## 4.2. Simulations

All simulations for this study were performed using the Matlab computer programming language.

### 4.2.1. Design of the Model Near Surface

For the simulations, a linear  $V(z)$  model is used to approximate the true near-surface layer. Values chosen for the synthetic models are based on linear gradients between the vertical velocities of the near-surface layer in the Blackfoot area (Chapter 3.6). These models were used to identify general patterns of receiver notching over a range of receiver depths and near-surface velocity gradients. For reflection amplitude simulations, an  $I(z)$  impedance model was derived by multiplying a plausible linear  $\rho(z)$  model with the  $V(z)$  model.

### 4.2.2. Construction of Model Source Wavelet

A 30-Hz dominant frequency Ricker wavelet served as the model source wavelet to simulate a broadband reflection. This function is the second derivative of the Gaussian error function (the classic bell curve), and is expressed analytically as

$$r(t) = (1 - 2\pi^2 v_M^2 t^2) e^{-\pi^2 v_M^2 t^2}$$

where  $r(t)$  is a Ricker wavelet with a mean (or “dominant”) frequency of  $v_{mean} = (2/\pi^2)v_M$ .

Figure 4.1 (a) shows the time-domain representation of the source wavelet, and Figure 4.1 (b) shows its frequency spectrum. The frequency spectrum shows that the highest amplitudes occur in the 15 to 45Hz range, and that amplitudes taper off more sharply at lower frequencies than higher frequencies. These frequency characteristics are typical for most pre-whitened seismic reflection data.

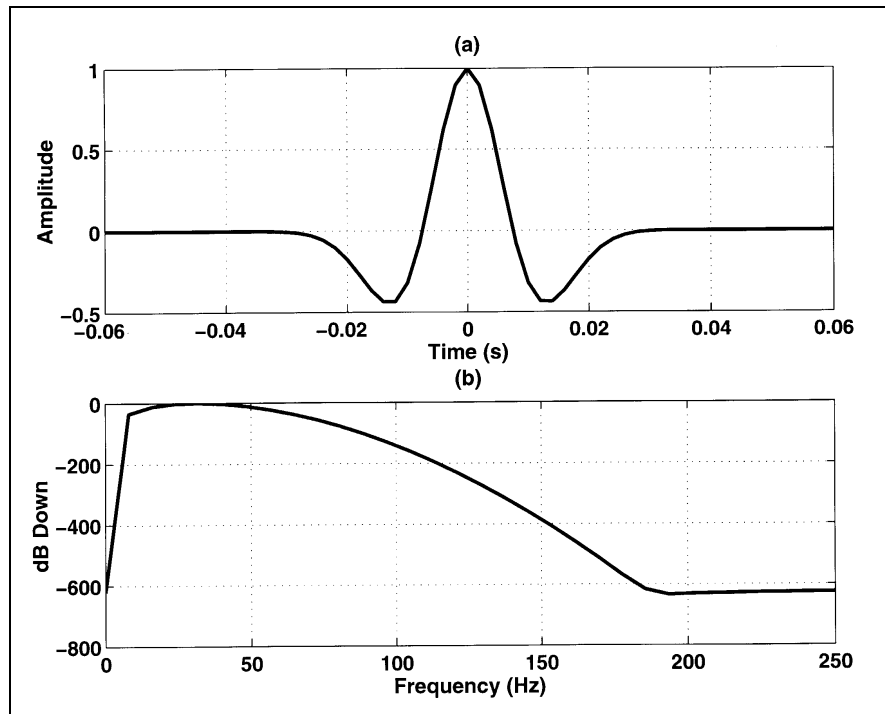


Figure 4.1. The (a) time and (b) frequency domain plots of the model 30Hz Ricker wavelet.

#### 4.2.3. Numerical Simulation of Propagating Wavelet

All simulations were performed with a Matlab function written for this study. The function allows the user to select the dominant frequency of the source Ricker wavelet, the receiver depths at which to look for notches, the time vector over which to “record” data, and the seismic velocities at the depth of the deepest geophone and at surface.

The function first creates the model Ricker wavelet, then steps it through each of the designated receiver depths, from the deepest to the shallowest, using the model velocity gradient. This is the “incident” wave field, which is a plane wave. It then performs the identical procedure, but starts from the shallowest geophone depth and propagates the wavelet downward (practically, the only difference is the presence of a minus sign in the stepping equation), to derive the “reflected” wave field. The phase of the incident and reflected wavelets is identical to simulate a wave that has reflected off a surface with reflection coefficient of -1 as recorded by a velocity-sensitive receiver (the geophones). Though the wave reverses polarity upon reflection, it is traveling in the opposite direction as the incident wave. Since geophones cannot distinguish between a

push from below and a pull from above, the reflected wave will be recorded with the same polarity as the incident wave. The total wave field recorded is found by summing the incident and reflected wave fields. Note that this situation is distinct from a hydrophone response; a hydrophone would record the incident and reflected wavelet as having opposite polarity, as it detects changes in pressure, which is a scalar (non-directional) quantity.

#### **4.2.3.1. Example**

The Matlab function plots the incident, reflected and total wave fields as wiggle traces. Figure 4.2 (a) shows an example of a 30-Hz Ricker wavelet propagating vertically upwards through the top 18m of a near-surface layer whose velocity decreases linearly from 3100m/s to 300m/s. The near surface model represents an extreme situation of glacial till containing the water table overlying relatively unweathered sandstone. This simulation is a common shot gather consisting of 76 buried geophones buried in the top 18 m of the near surface layer, at a depth increment of 0.25 m. At depths below 9m or so, velocities are still high and the wavelet appears to arrive at each geophone nearly simultaneously. At shallower depths, the wavelet arrives at each geophone with a successively greater lag time. This plot represents the incident wave field. Figure 4.2 (b) shows the same wavelet, having reflected off the free surface at 0 meters, propagating to greater depths. This represents the reflected wave field. Figure 4.2 (c) shows the sum of the incident and reflected wave fields. This is the total wave field.

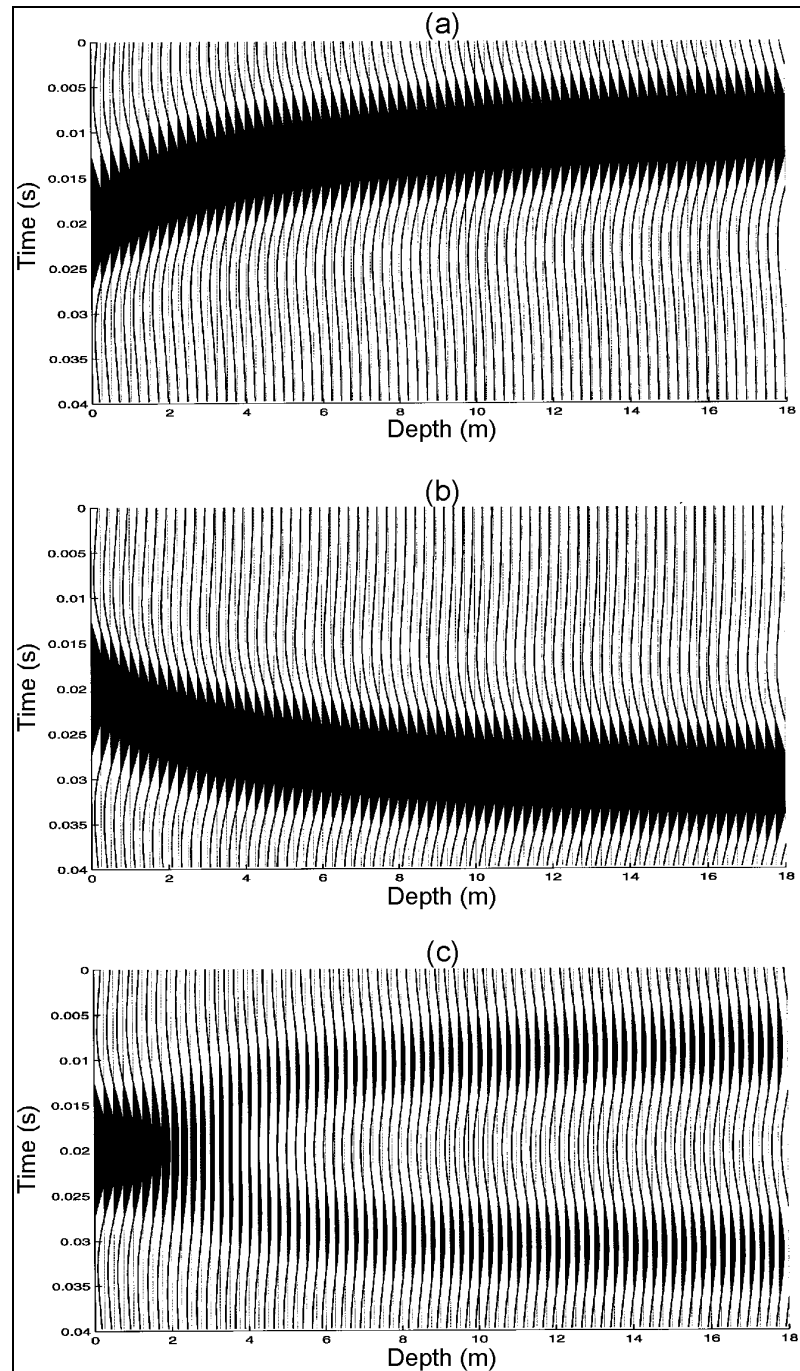


Figure 4.2. (a) Incident model 30-Hz Ricker wavelet in a linear  $V(z)$  medium, (b) reflected wavelet, (c) total wavefield (incident + reflected), which is detected by the geophones.

The shape of the incident, reflected and total wave field for a given time can be viewed in the depth domain. Figure 4.3 shows a “snapshot” of what each field looks like

just before the Ricker wavelet peak reaches the surface ( $t=0.018s$ ). Because of the high velocity gradient, the incident and reflected wavelets are stretched greatly at depths below about 6m, and do not resemble the Ricker wavelet as recorded in the (linear) time domain (Figure 4.3 (a)). The total wave field is twice the amplitude of the incident at the surface, due to the free surface effect. At depths between about 2 and 17m, the absolute amplitude of the total wave field is less than that of either the incident or reflected wave fields, and is zero at about 7m depth. This indicates that destructive interference is occurring, which suggests that geophones buried at depths between 2 and 17m could be expected to have poorer signal-to-noise ratios than geophones at other depths. Note also that the shape of the total wave field is different from both the incident and reflected wavelet, indicating that wavelet distortion has occurred.

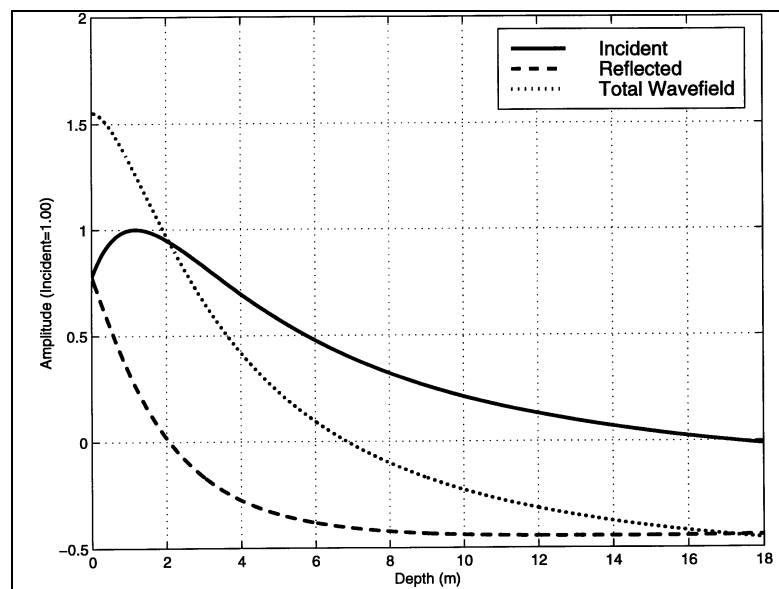


Figure 4.3. Incident, reflected and total wave fields in the depth domain for a 30-Hz dominant frequency Ricker wavelet at  $t=0.018s$ . Near-surface velocity is linear:  $V_0=300m/s$ ,  $V_{18}=3100$ . Interference is constructive to a depth of 2 meters, and mostly destructive at greater depths.

#### 4.2.4. Receiver Notching

Depth-dependent receiver notches were investigated by taking the Fourier spectrum at each depth of the total wavefield. The patterns of receiver notches were rather intricate, and did not exhibit well on a two-dimensional line plot. To display the

data in all three dimensions of depth, frequency and amplitude, the data were plotted as colour contours. Figure 4.4 is an example of such a plot for a constant velocity medium ( $V = 900\text{m/s}$ ), which represents the average velocity of the top 18m of the surface layer in the Blackfoot III area as determined from vertical interval velocities (Chapter 3.6). The plot shows a 100-Hz receiver notch emerging at a depth of about 3m below surface. With increasing depth, the notch rapidly moves to lower frequencies, reaching about 12Hz at 18m depth. Three additional harmonics of the first notch appear at depths below 7m and follow the same pattern. This plot indicates that a geophone located between 4m and 18m depth in this medium would have several notches of over 60 dB below maximum in the dominant frequency range of seismic data.

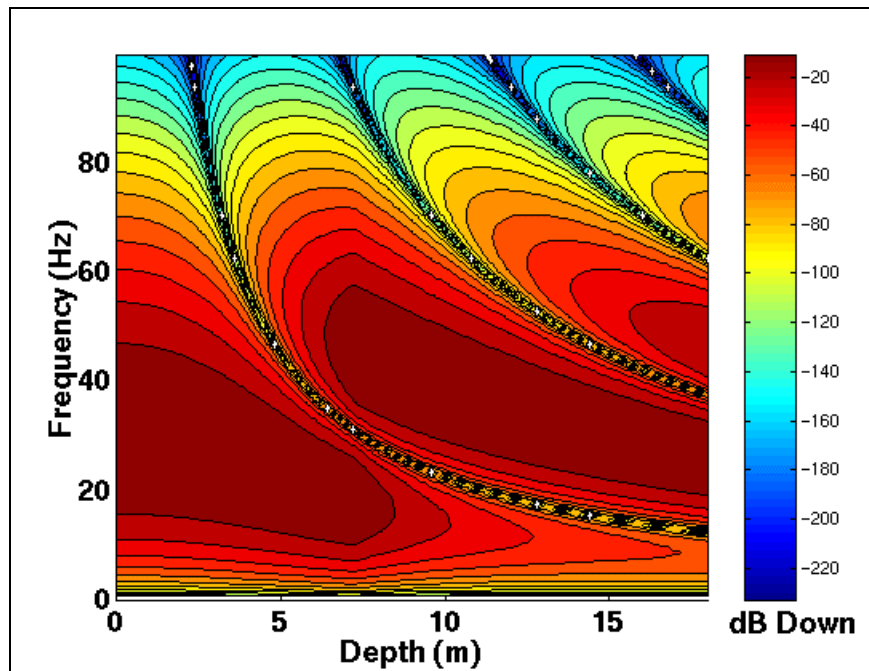


Figure 4.4. Frequency spectrum for a wavelet reflecting in a constant  $V=900\text{m/s}$  medium bounded by a free surface. The contours represent decibels down from the maximum amplitude.

Figure 4.5 shows the same plot for the linear velocity gradient discussed in the previous section. The plot reveals a 100-Hz receiver notch emerging at a depth of 1m below surface. With increasing depth, the notch rapidly moves to lower frequencies, reaching about 27Hz at 18m depth. The first harmonic of this notch emerges at 6m depth and follows the same pattern, declining to about 75Hz at 18m depth.

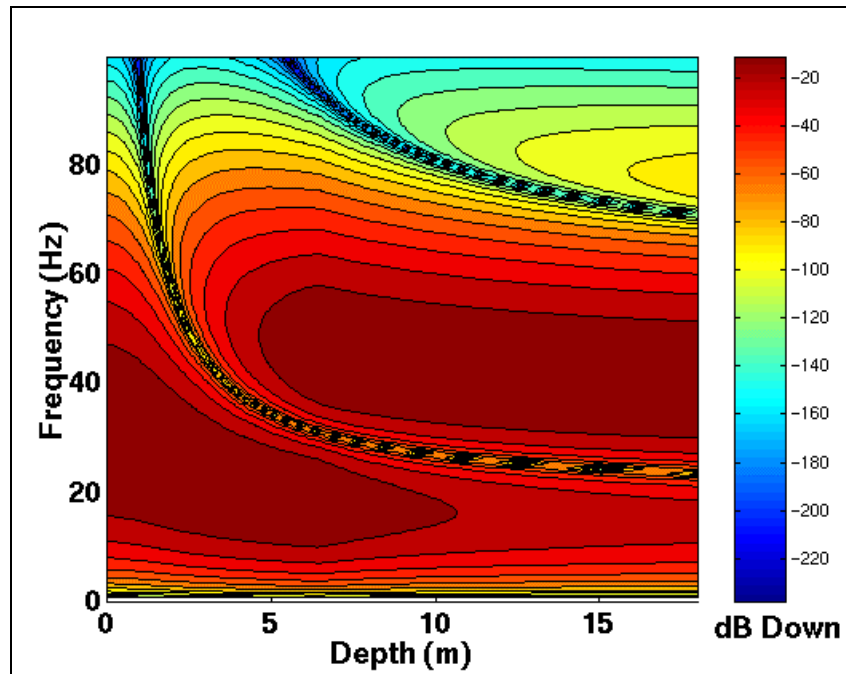


Figure 4.5. Same as Figure 4.4 for a steep-gradient ( $V_0=300\text{m/s}$ ,  $V_{18}=3100\text{m/s}$ ) linear  $V(z)$ .

Figure 4.6 shows the same plot for a shallower ( $V_0 = 300\text{m/s}$ ,  $V_{18} = 2200\text{m/s}$ ) velocity gradient, representing glacial overburden overlying weathered bedrock. These are more typical velocity values for the Blackfoot area. The high-frequency notch appears at 1m depth as before, but declines to 20Hz at 18m depth. Two harmonic notches join the first at depth increases. A medium with an even shallower velocity gradient ( $V_0 = 300\text{m/s}$ ,  $V_{18} = 900\text{m/s}$ ) represents an overburden layer composed entirely of glacial till with a deep water table. Its pattern of expected receiver notches appears in Figure 4.7 At this gradient, 6 notches have appeared at the 18 meter depth, and almost every depth contains one or more notches in the dominant bandwidth of the source Ricker wavelet.

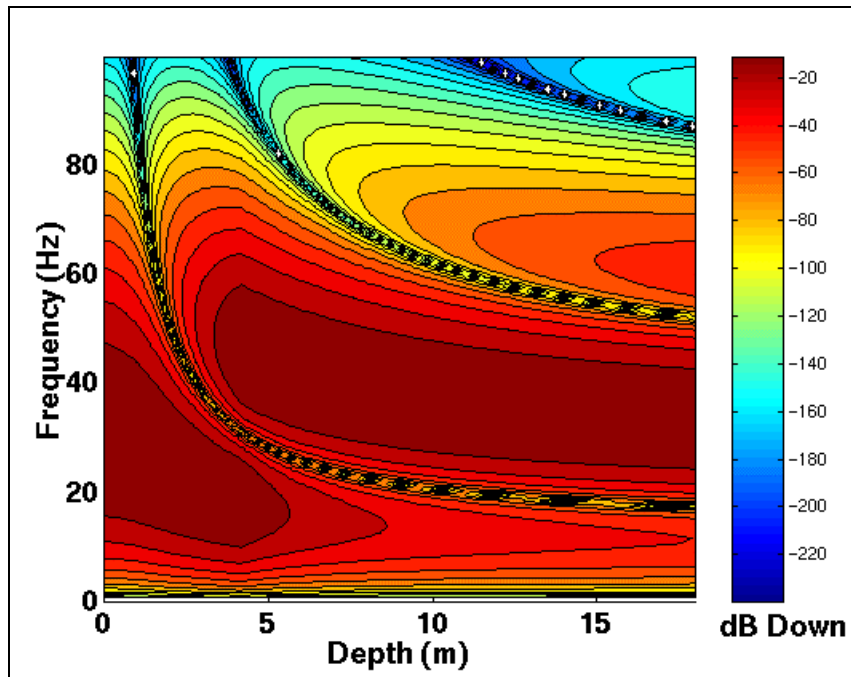


Figure 4.6. Same as Figure 4.5 but for an intermediate velocity gradient ( $V_0=300\text{m/s}$ ,  $V_{18}=2200\text{m/s}$ ).

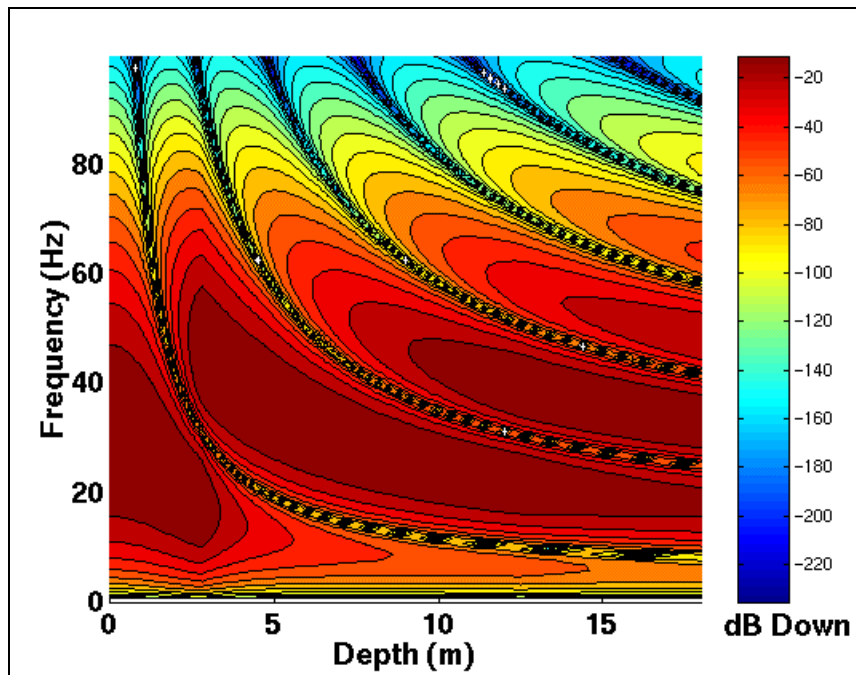


Figure 4.7. Same as Figure 4.5 but for a shallow velocity gradient,  $V_0=300\text{m/s}$ ,  $V_{18}=900\text{m/s}$ .

The contoured plot of Figure 4.8 simulates expected receiver notching patterns for converted waves in a linear  $V(z)$  model. In this plot, the dominant frequency of the Ricker wavelet is 12Hz, and the average velocity and velocity gradient of the medium resemble near-surface shear-wave velocities of the Blackfoot area ( $V_0=150\text{m/s}$ ,  $V_{18}=400\text{m/s}$ ). There are up to six notches in the spectrum for typical converted-wave frequencies, which is more than appear in the compressional-wave simulations.

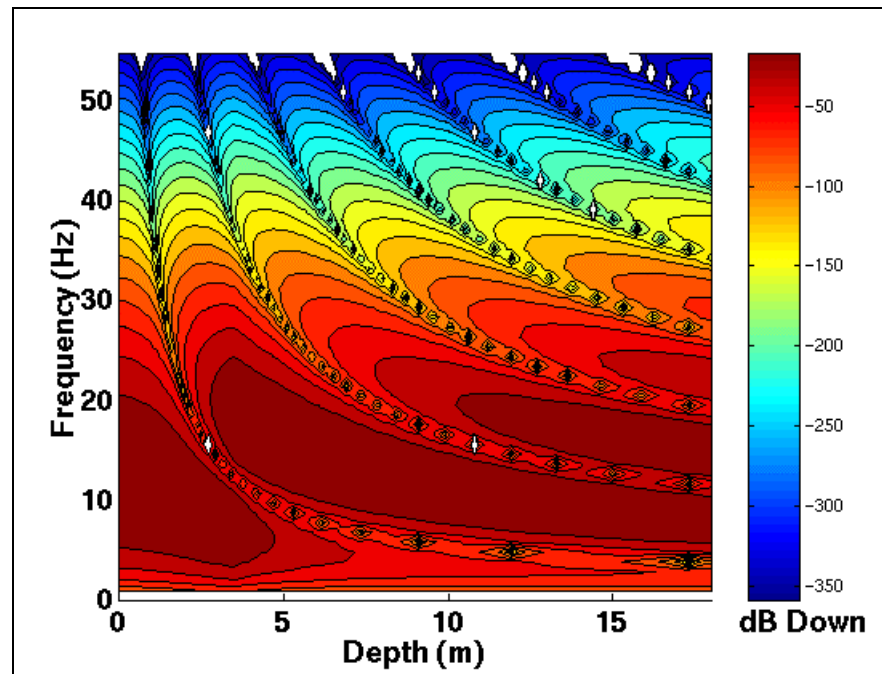


Figure 4.8. Frequency spectrum for a converted-wave velocity gradient,  $V(z)$ :  $V_0=150\text{m/s}$ ,  $V_{18}=400\text{m/s}$ .

The simulations indicate that in a linear  $V(z)$ , receiver notching will occur for depths greater than one meter in the dominant frequency bandwidth of seismic data. The notches asymptotically approach zero frequency at a rate that is inversely proportional to the average velocity and velocity gradient of the near-surface. The simulations also indicate that more notches emerge for slower near-surface velocities.

#### 4.2.4.1. Comparison to Blackfoot III Data

Data from the Blackfoot III buried geophone experiment contained numerous noise sources (e.g. ground roll, refractions, 60Hz contamination) that were not included in

the synthetic simulations. Therefore, to properly compare the real data to the simulations, they were passed through the f-k filter described in Chapter 3.5 that was designed to reject ground roll and refracted energy. The filter effectively isolated the reflected data that were used for analysis. The filtering was performed in ProMax and then the data were imported into Matlab for analysis. The time windows for frequency and amplitude analysis were 900-2000ms for the vertical channel data and 1400-2400ms for the radial channel, as these time intervals contained the zone of interest and other clear reflections.

The f-k filtered data from several buried geophone stations were analyzed for frequency content using Matlab software (Margrave, 1999). Figure 4.9 shows an example of the frequency spectra for *P-S* reflections for all depths for buried geophone station number 226. The spectra are rather noisy despite the f-k filtering. Many notches occur in the data that are present at all depths; the causes of these may include source ghosts, interbed multiples, near-surface reverberations and the earth's reflectivity. This complicates the search for receiver notches as it is possible one may occur at a frequency that is already notched from another cause.

There are several notches that appear at one depth but not at the others, indicated with arrows on Figure 4.9. One such notch at about 18Hz is quite pronounced; other notches are more subtle. The frequency spectrum from the 18m depth geophone contains more notches than the spectrum of the 12m geophone, which in turn contains more notches than the spectrum of the 6m geophone. This observation is consistent with the synthetic results. Other buried geophone stations show a similar pattern.

Figure 4.10 shows the amplitude spectra for all geophone depths for *P-P* reflections of receiver station 426. There are fewer depth-dependent notches observable in the spectra (one possible receiver notch is indicated with an arrow) than was the case for the *P-S* reflections. This was observed to be true in general for the buried geophone data. In many cases, no convincing receiver notches could be found, indicating perhaps that in practice the receiver notches are too superimposed with signal and random noise to be readily identifiable.

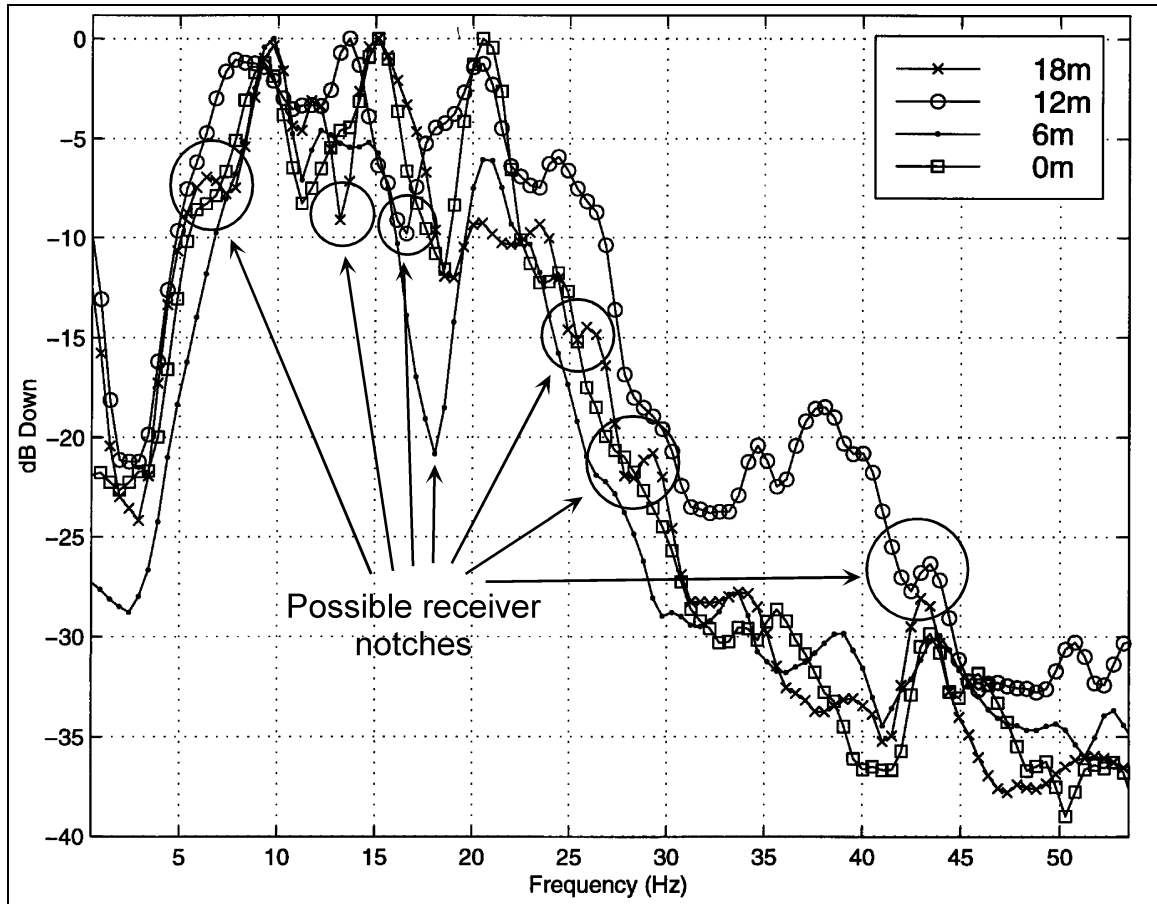


Figure 4.9. Frequency spectra for converted-wave reflections of station 226 from the Blackfoot III buried geophone experiment. Arrows indicate possible receiver notches.

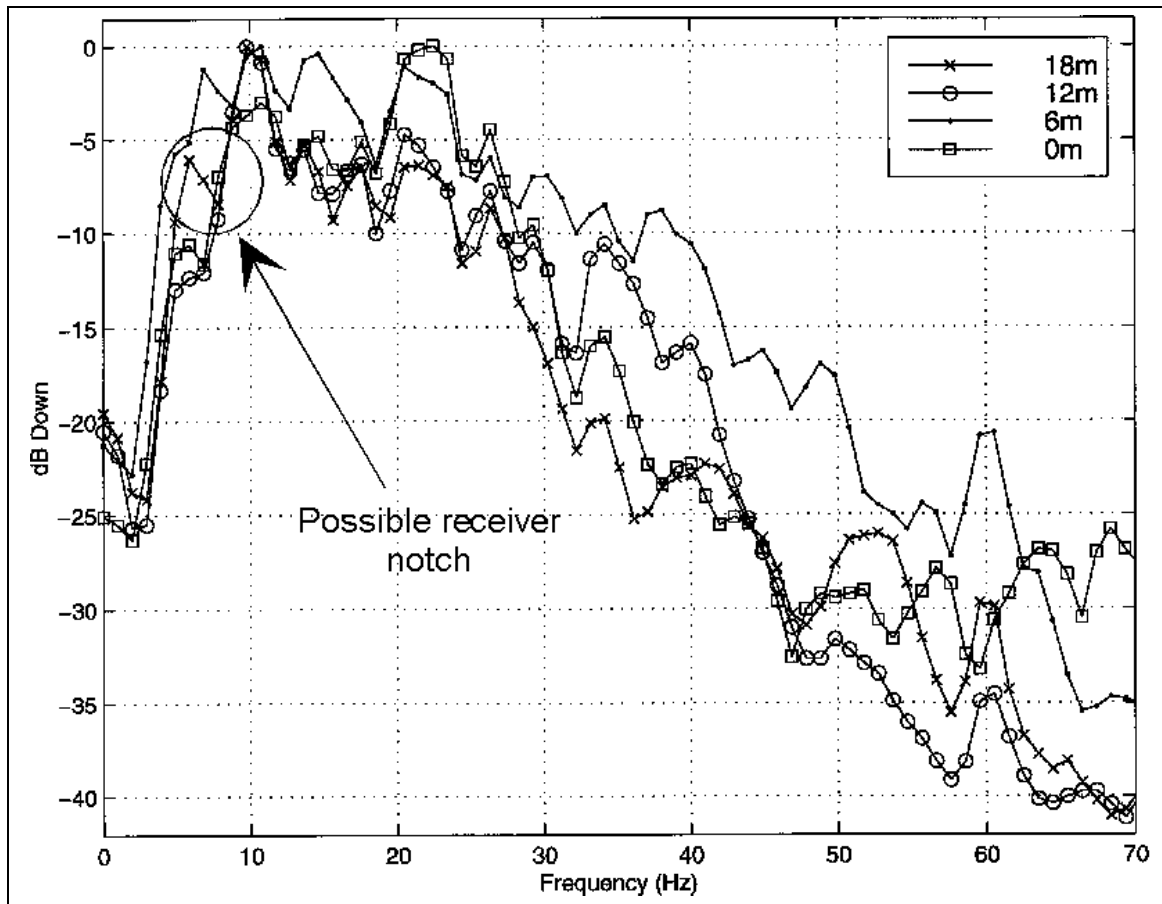


Figure 4.10. Frequency spectra of compressional-wave reflections from station 426 of the Blackfoot III buried geophone experiment. A possible receiver notch is indicated.

As seismic velocities for unconsolidated material are known to be much higher for *P*-waves than *S*-waves, particularly below the water table (Lawton, 1990), the observed notching patterns are consistent with those predicted by the Ricker wavelet simulations.

#### 4.2.5. Wavelet Interference Effects on Amplitude

As demonstrated in Figure 4.3, interference between the incident and reflected wavelets may cause a significant reduction in recorded amplitudes. Figure 4.11 shows the maximum amplitude recorded at each geophone depth for the entire record for four velocity gradients. The data have been normalized so that the maximum amplitude of the incident wavelet is 1.00. Amplitudes at surface are 2.00 due to the free surface effect. In all cases, amplitudes decrease rapidly to about 27% of surface values, at a depth

proportional to velocity gradient and average velocity of the media. At greater depths, amplitudes recover gradually back to those of the incident wavelet at a rate inversely proportional to velocity gradient. For steep gradients and high velocities, amplitudes do not achieve that of the incident wavelet even at a depth of 18 meters.

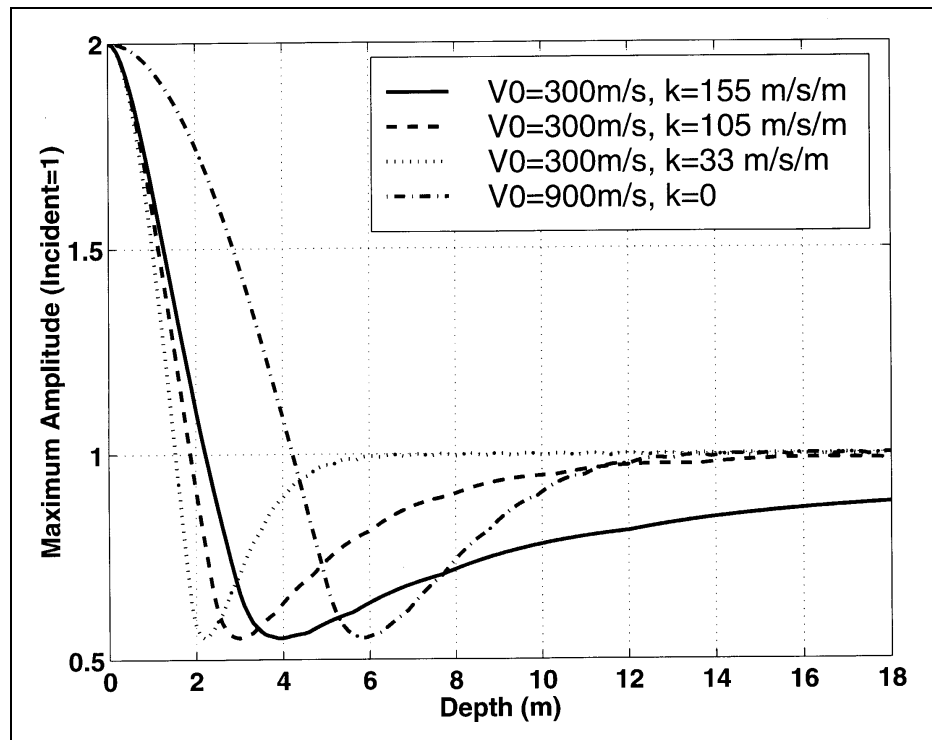


Figure 4.11. Total wavefield maximum amplitude for four velocity gradients.

#### 4.2.6. Near-Surface Impedance Effects on Amplitude

The normal-incidence transmission coefficient  $T$  for a wave traveling from a medium of seismic impedance  $I_1 (=V_1\rho_1)$  to a medium of impedance  $I_2 (=V_2\rho_2)$  is

$$T = \frac{2I_1}{I_2 + I_1}.$$

This is a good approximation for angles of incidence of up to  $15^\circ$  for most geologic materials (Sheriff and Geldart, p. 76). Note that if  $I_2 < I_1$ , then  $T > 1$ ; *i.e.*, the

amplitude of a wave increases when passing into a medium of lower impedance\*. Hence, a reflection should experience increasing amplitude as it approaches the surface. To simulate this, a linear  $V(z)$  model from the receiver notch simulations was multiplied by a linear  $\rho(z)$  model to derive an  $I(z)$  impedance model. The density model is a linear gradient from  $\rho_{18}=2400\text{kg/m}^3$  (plausible for unweathered bedrock) to  $\rho_0=1200\text{kg/m}^3$  (representing weathered clay). The  $I(z)$  impedance model was divided into 18 discrete, equal steps, and the transmission coefficients were calculated at the boundary of each step using the above equation. The amplitude of a wave in a given layer traveling vertically through the model is the product of the transmission coefficients of the boundaries. Doubling the last calculated amplitude simulates the free surface effect.

The absolute amplitudes of the real buried geophone data are essentially arbitrary, so the synthetic amplitudes were multiplied by a constant to match the real data.

#### **4.2.6.1. Comparison to Blackfoot III Data**

Figures 4.12 and 4.13 show semi-log plots of  $P$ - $P$  and  $P$ - $S$  reflection average absolute amplitudes versus depth of f-k filtered receiver gathers, in a certain time window. The reflection amplitudes decrease with depth; the fact that the geophones could not always be placed at the desired depth (Figure 3.4) only shows the relation more clearly. Also plotted are the amplitudes for a simulated wavelet (scaled by a constant) travelling through the  $I(z)$  model as described in the previous section. Though the geophone reflection amplitudes exhibit some scatter, they are in strong agreement to the impedance model amplitudes. No amplitude minimum can be seen in the data as predicted by wavelet interference simulations, although the 6m depth geophones recorded slightly lower  $P$ -wave amplitudes than expected from the impedance model. Whether this disagreement between the real and predicted reflection amplitudes is due to wavelet interference or discrepancies between the model and the true near surface cannot be said at this time. Overall, the agreement between the impedance model and the real data

---

\*Note that the event of transmission always conserves energy, as the transmission coefficient for energy is  $(I_2/I_1)T^2$ , which is one or less for all impedance contrasts (Sheriff and Geldart, 1995).

indicates that reflection amplitudes as recorded by buried geophones are primarily controlled by the impedance gradient of the near surface.

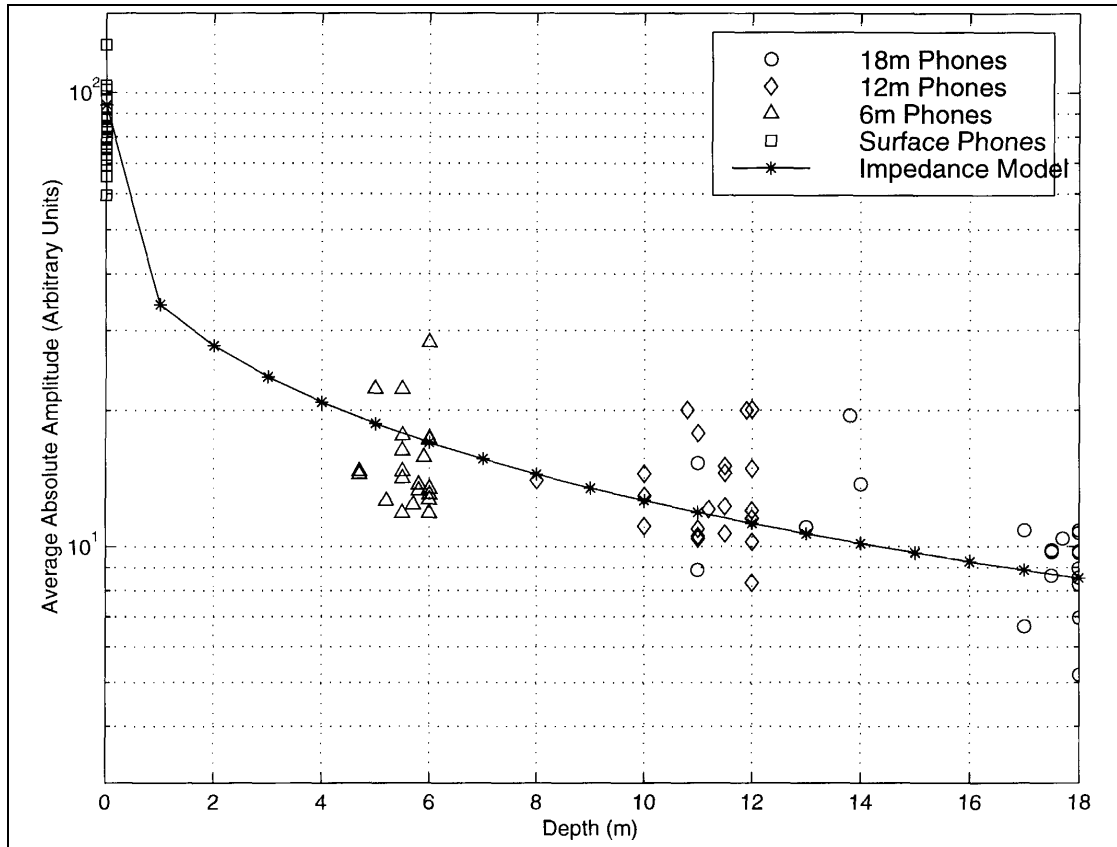


Figure 4.12. Actual and modeled amplitudes for  $P$ -wave reflections as recorded by buried geophones. Actual data points are the absolute amplitudes of  $P$ - $P$  reflections between 900 and 2000ms from the Blackfoot III buried geophone data. Data were  $f$ - $k$  filtered to suppress ground roll and refracted energy prior to amplitude analysis. Modeled amplitudes are from an 18-step  $I(z)$  impedance model where  $I(z)=V(z)\rho(z)$ ;  $V_{18}=3100\text{m/s}$ ,  $V_0=300\text{m/s}$ ,  $\rho_{18}=2400\text{ kg/m}^3$ ,  $\rho_0=1200\text{ kg/m}^3$ .

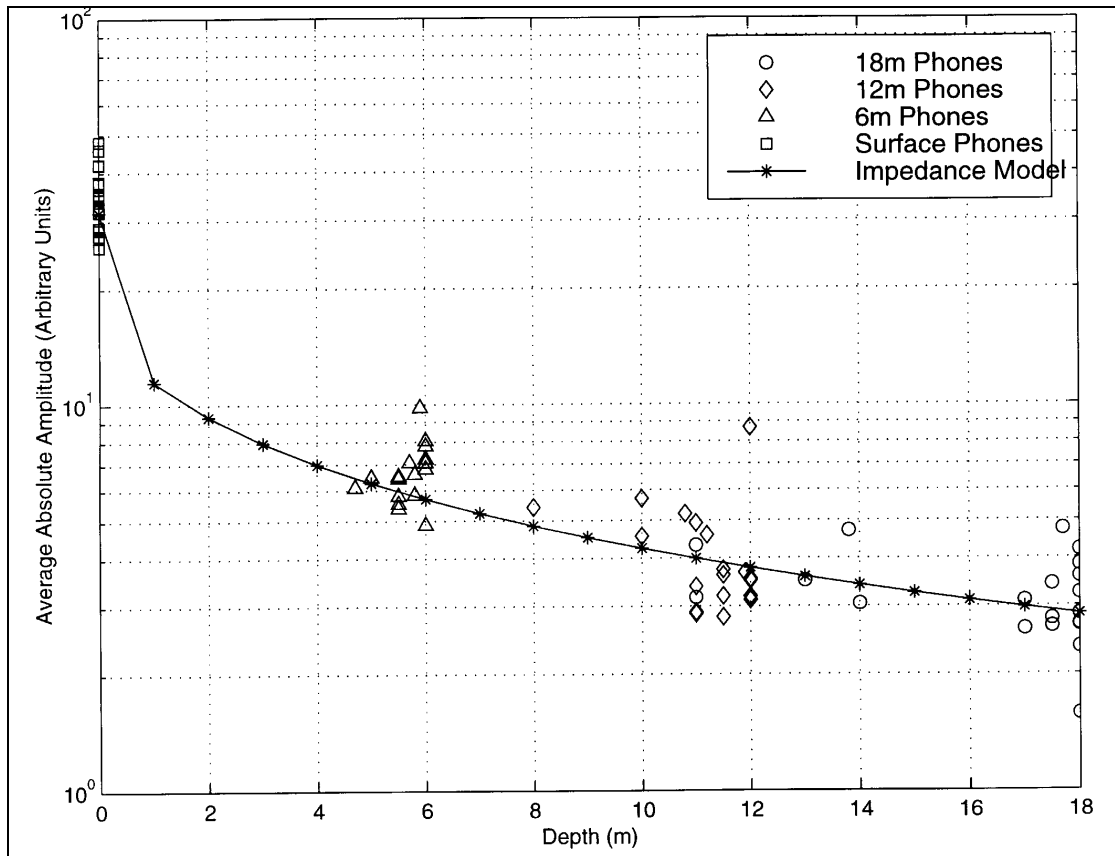


Figure 4.13. Same as Figure 4.12 for  $P$ - $S$  reflections between 1400 and 2400ms. Impedance model is based on linear  $V(z)$  where  $V_{18}=1500\text{m/s}$ ,  $V_0=150\text{m/s}$ , and linear  $\rho(z)$  where  $\rho_{18}=2400\text{ kg/m}^3$ ,  $\rho_0=1200\text{ kg/m}^3$ .

## CHAPTER 5

### BLACKFOOT III INTERPRETATION

There were two important considerations made in the design phase of this experiment in order to assist in interpreting the Blackfoot III seismic data. The first is that the survey was designed so that the fold would be maximum at the mid-point of the producing channel-fill sediments. This was, naturally, to ensure that seismic data quality, in terms of signal-to-noise ratio, was highest across the producing zone. Secondly, the line was situated adjacent to the producing oil well 09-08, for which *P*-wave and *S*-wave sonics, as well as density logs, are available for most of its length (Figure 5.1).

The full sonic and density logs for the 09-08 well are advantageous, because together they can be used to calculate the *P*-wave and *S*-wave impedance of the formations. It is not necessary to make approximations of  $V_s$  from regional  $V_p/V_s$  values or density from a Gardner's relationship, so the resulting synthetic traces generated are expected to be robust.

Interpretation was made on migrated sections from the surface geophones, which had the highest data quality in terms of signal-to-noise ratio.

#### 5.1. Geology and Depositional Environment of the Mannville Group

In the Blackfoot area, the producing Glauconite member is contained within the unconformity-bounded Lower Cretaceous Mannville group (Figure 5.2). Presented here is a review of the geology and depositional environment of all units of the Mannville group that appear in the Blackfoot area. All are interrelated with the development of the reservoir zone in some way, and information of the known geology from well control is important for a credible seismic interpretation.

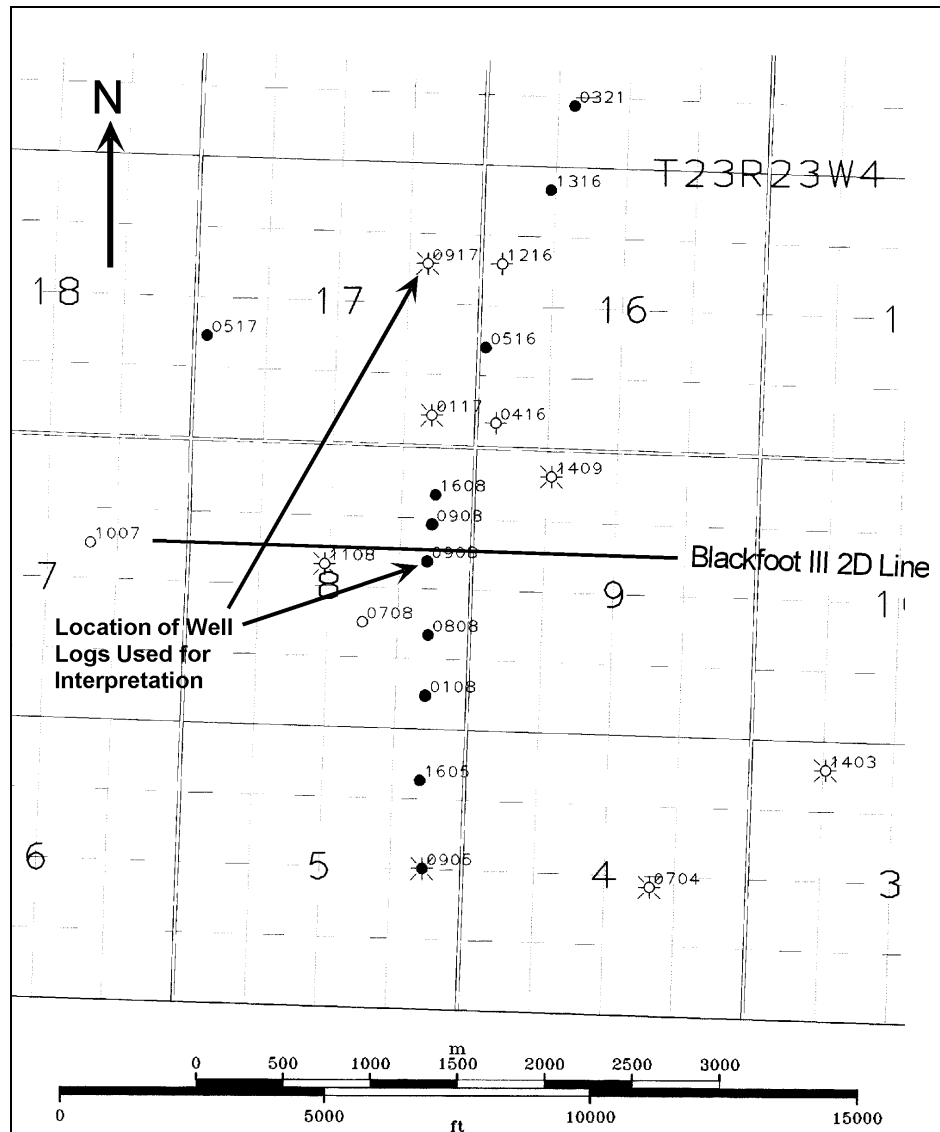


Figure 5.1. Location of well logs used to interpret the Blackfoot III line.

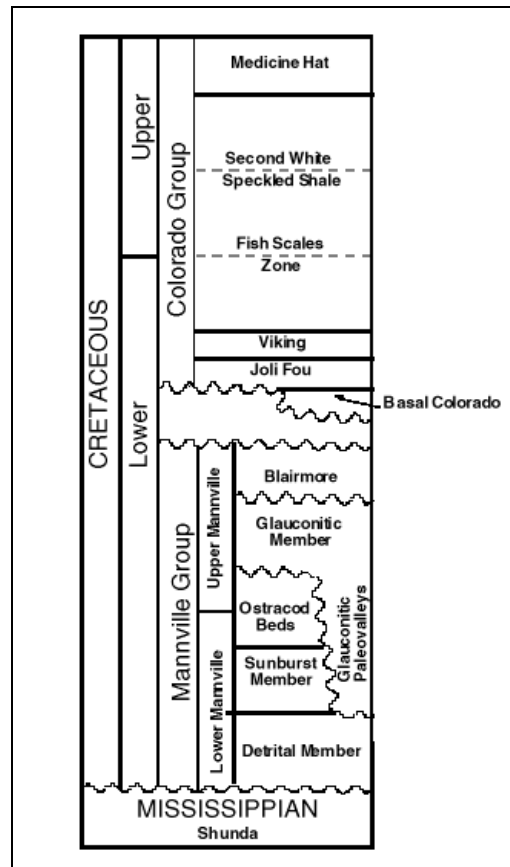


Figure 5.2. Stratigraphic cross-section of the Mannville Group and surrounding formations (from Miller *et al.*, 1995).

In general, the entire Mannville group represents a major transgressive-regressive cycle from the Boreal Sea, superimposed with complex sea-level fluctuations (Wood and Hopkins, 1992). The first member of the Mannville group, the Detrital, was deposited unconformably on the irregular surface of Mississippian carbonates of the Shunda formation in the Blackfoot area (Miller *et al.*, 1995), and almost completely leveled the paleotopography. Its thickness is therefore largely controlled by the surface of the Mississippian that underlies it. The Detrital member has a very variable composition of chert pebbles, lithic sandstone, siltstone and shale. Further transgression of the Boreal sea occurred, and the Sunburst member and Ostracod beds were overlain next in succession. The Sunburst is composed of sub-litharenites and quartzarenites forming ribbon-and-sheet sandstone, while the Ostracod beds are composed of brackish water

shales, argillaceous, fossiliferous limestones and thin quartz sandstone and siltstone layers.

At this point, there occurred the first of a series of marine regressions/transgressions. The regressions were characterized by some erosion and soil development at the top of the subaerially exposed Ostracod beds in places. It was also during the regressions that, crucially, a series of northwest-flowing river systems developed that incised valleys often as far downwards as the Detrital member. The valleys have not been observed to cut completely through the Detrital, so they can be considered to have formed essentially independently of the irregular surface of the Mississippian.

The transgressions were characterized by deposition of the Glauconite member, which is the hydrocarbon-producing unit in the Blackfoot field. As the sea impinged on the channel-cut surface, it deposited estuarine sediments in the valleys first, and then at inter-valley locations with further relative sea-level rise. In the valleys, the Glauconite member forms elongate pods of porous (average 18%) estuarine sand bars up to 35 meters thick in the Blackfoot area, and is composed of fine- to medium-grained quartz sandstone, separated by shales. These shales act as a hydrocarbon seal in the Blackfoot reservoir. The non-reservoir formations on the valley sides can also serve as a barrier to hydrocarbon migration. Between valleys, the Glauconite member forms thin (<6m), discontinuous sandstone sheets.

Complex sea level fluctuations continued, and the cycle of valley incision and infilling repeated several times. This caused the Glauconite member to develop into a series of independent, superimposed major regional channel-fill systems, with accompanying interfluvial deposits. The Blackfoot area contains a channel that has been cut and infilled three times by the Glauconite member. The three infills have been termed the Upper, Lithic and Lower valleys by Dufour *et al.* (1998), though all three infills may not be present everywhere in the channel. The Lithic valley is non-reservoir quality, and can act as a hydrocarbon seal between the producing Upper and Lower valley deposits.

Unconformably overlying the Glauconite are additional channel-cut estuarine and coastal plain sediments, but with a fundamentally different sediment provenance. This is the Blairmore formation in the Blackfoot area, and is the topmost unit of the Mannville

group. It is important because it has a relatively low vertical permeability (.01-10 md), and can act as an updip seal to hydrocarbon migration for the underlying Glauconite member. It also contains several excellent coal markers that correlate between wells and generate distinct seismic signatures; this aids greatly in interpretation.

The Blairmore is the topmost member of the Mannville group, and is overlain unconformably with marine sediments of the Colorado group. Formations above this unconformity are stratigraphically distinct from the formations that contain the Blackfoot reservoir.

## **5.2. Generation of Synthetic Seismograms from Well Log Data**

Converting sonic and density well logs to expected surface seismic expressions was accomplished using software that uses full Zoeppritz equations to determine offset- (*i.e.* angle-) dependent  $P$ - $P$  and  $P$ - $S$  reflectivity (Lawton and Howell, 1992; Margrave and Foltinek, 1995). The reflectivity values at each offset are convolved with a user-specified source wavelet to generate a synthetic offset gather. The traces in the offset gather are then stacked to produce a synthetic common reflection point trace that presumably simulates the seismic response of the formations at the location of the well. It should therefore tie to common reflection point seismic sections at the well location.

The software also converts the formation tops from depth to time, and plots them on the synthetic traces. This makes possible the crucial link between the formation tops and their corresponding peak, trough or zero crossing on the seismic data, which makes data interpretation possible.

The synthetic traces were generated using a 50m receiver interval to a maximum offset of 800m. The near-surface model was calculated automatically by the program, and not specified, to ensure consistency between different synthetic traces. For the  $P$ - $P$  synthetic traces, a zero-phase 5-10-70-80Hz bandpass source wavelet was used, as this most closely matched the bandwidth and phase of the processed section. The  $P$ - $S$  synthetics were generated with a zero-phase 5-10-35-45Hz bandpass wavelet for the same reason. The log integration interval was 2ms for  $P$ - $P$  and 3ms for  $P$ - $S$  reflections, as recommended by Miller *et al.* (1995) for good matching to the data. No spherical spreading, attenuation or transmission losses were included in the modeling as these

effects had been corrected for during data processing. The NMO-stretch was not included, as it was found to have no detectable effect on the synthetic traces.

### **5.3. Log Splicing**

The Blackfoot III line tied to the 09-08 well only, which intersected the Glauconite channel, but did not reach the top of the Mississippian. To interpret off-channel data and the Mississippian, it was necessary to splice the lower portion of the 09-17 log into the 09-08 log to create a “Regional” log (Figure 5.1). The 09-17 well is from a gas-producing well that is slightly off-channel, and so, when spliced into the 09-08 log, simulated off-channel response of the Blackfoot III line. The splice point was the Coal 3b formation top, as this formed a distinctive seismic marker that was common to both wells, and was relatively close to the zone of interest.

The 09-17 sonic and density logs were resampled from a 0.3048 to a 0.1524m depth interval to match the 09-08 log. The resampling was done using a Matlab program that performs smooth data interpolation with a sinc function.

### **5.4. Channel and Regional Synthetic Ties**

Figure 5.3 shows the “Channel” and “Regional” *P-P* synthetic traces inserted into the interpreted *P-P* migrated data for the zone of interest. Selected reflections are interpreted; in general there is good agreement between the “Channel” synthetic traces and the seismic data. The Glauconite channel fill zone corresponds to the last trough on the trace, and a portion of the lower frequency, high-amplitude peak above it. The remainder of the peak corresponds to the Coal 2 and Coal 3 markers, and the trough above that corresponds to the Coal 1 marker (interpreted).

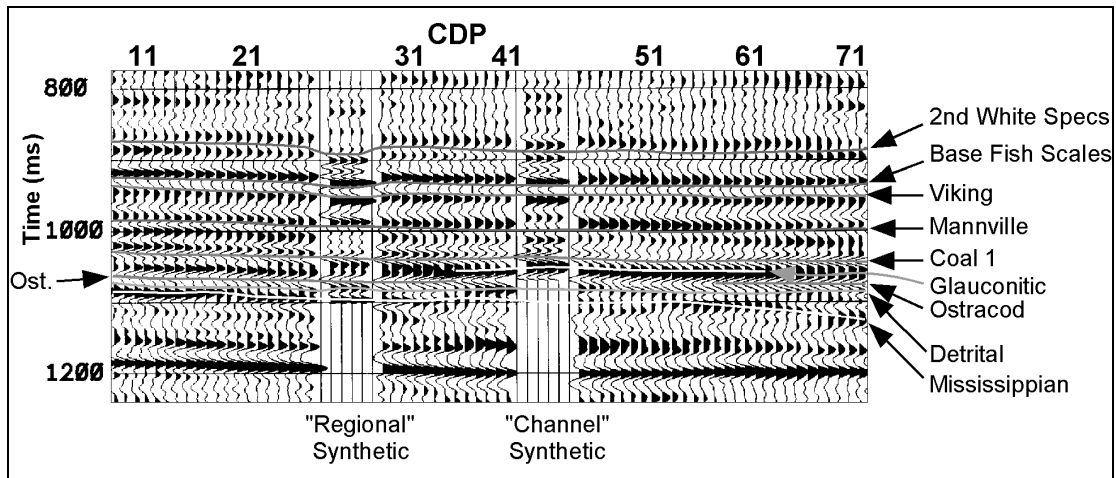


Figure 5.3. Channel (09-08) and regional (09-17 spliced into 09-08) synthetic ties to the  $P$ - $P$  data.

The regional synthetic traces also show good agreement to the data, with some trace stretching for times earlier than 900ms. Trace stretching is a well-known phenomenon caused by short path multiples and frequency dispersion (Stewart *et al.*, 1984). This problem can be reduced if the sonic data are check shot corrected, but these data are not. The peak at the bottom of the regional synthetic trace corresponds to the top of the Mississippian, which appears to form a structural low to the right (west) of the section. The peak above the Mississippian on the regional synthetic traces corresponds to the Detrital member. Its reflection character changes greatly toward the location of the channel as it becomes replaced with the channel-fill sediments, and becomes seismically unresolvable from them at the channel. On the right side of the section, reflections contained in the Detrital formation can be seen to onlap the Mississippian. Above the Detrital, the Sunburst member (not interpreted in Figure 5.3) and Ostracod beds correspond to a trough, which narrows and increases in amplitude as they are replaced with the channel sediments towards the center of the section.

Above the Sunburst and Ostracod formations is a doublet that corresponds to the Coal 2 and Coal 3 formations, which ties to a doublet in the seismic data (only Coal 1 is interpreted in Figure 5.3, that ties to the overlying trough). Over the channel, the doublet turns into a single peak; this change in reflection character is possibly compaction related. For earlier times, the trace is the same as the channel synthetic due to log splicing.

To summarize the observations, the Glauconite channel appears as a high-amplitude trough surrounded (in time) by two single peaks. Towards the regional section, the trough broadens out and decreases in amplitude slightly, and the positive amplitude peaks surrounding it turn into doublets. These results are similar to observations made by Miller *et al.* (1995), for a 2-D line that intersects the channel at a different location. They observed that the Glauconite trough tends to decrease in amplitude and become replaced by the Detrital peak off-channel. The comparison is complicated by the fact that the boundaries between different channel fills resolve seismically in the 1995 survey, which does not appear to be the case for the Blackfoot III survey. The coal markers may change their reflection character from a doublet to single peak due to a compaction relationship with the underlying Glauconite. Using these observations, the location of the channel is interpreted to be between CDPs 36 and 61.

Figure 5.4 shows the interpreted *P-S* migrated sections from the surface geophones, with inserted *P-S* synthetic channel and regional traces, for the zone of interest. The quality of the tie appears to be slightly better than the vertical channel synthetic ties, and there is less trace stretching. The Glauconite channel corresponds to a peak at the end of the channel synthetic, which ties to a peak on the section. Above this is a broad trough, the bottom portion of which correlates to the coal markers.

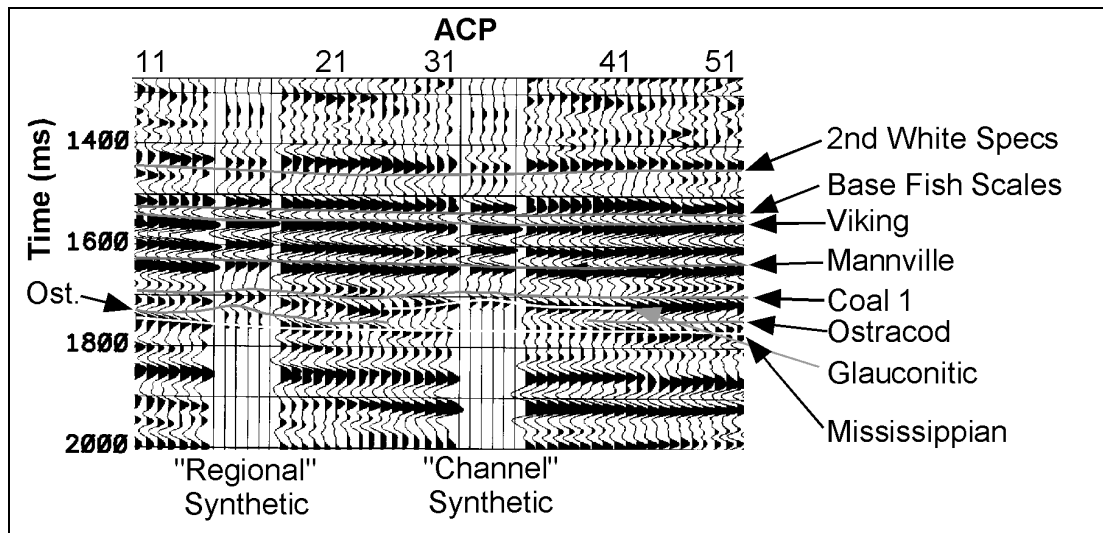


Figure 5.4. Channel and regional *P-S* synthetic ties.

The peak at the end of the regional synthetic traces correlates to the Mississippian, but the Detrital peak above does not correlate to the data, making its interpretation uncertain. The Sunburst (not interpreted) and Ostracod formations correlate to a small trough above this, which broadens out towards channel as they become replaced by the channel-fill Glauconitic sediments. The first zero crossing of the overlying peak corresponds to the coal markers, representing the splice point. In the seismic data, above the Coal 1 reflection there appears a small peak in a larger trough in the off-channel locations, which becomes a single broad trough above the channel. Again, this change in reflection character on- and off-channel may be due to differential compaction due to the underlying formations.

In general, the channel-fill sediments have a *P-S* seismic expression of a broad trough beneath a peak. Towards regional facies, the trough narrows, though the exact location of the channel edge is ambiguous. Formations above the Coal 1 marker change reflection character over the channel, possibly due to differential compaction. Largely due to superior data quality, the channel was more easily interpreted on the vertical than radial sections.

## CHAPTER 6

### CONCLUSIONS AND RECOMMENDATIONS

The buried geophone experiments were successful inasmuch as it was demonstrated that, for the locations studied, no significant improvement in converted-wave bandwidth can be expected by burying geophones up to a depth of 18 meters below surface. Therefore, shear wave attenuation in the top 18m of overburden sediments is not responsible for the reduced bandwidth observed in surface converted wave data for the areas studied.

The other conclusions are:

- The reflections undoubtedly attenuate a certain amount between 18m depth and surface, but this was likely dominated by bandwidth variations due to differences in geophone coupling.
- Mode leakage was observed in about half of the buried geophones in each experiment. The leakage likely occurred as a result of the buried geophones tilting away from vertical and twisting out of alignment with the shot line during emplacement with wooden planting poles. Surface geophones from both experiments, which were hand-planted, did not exhibit mode leakage. Receiver re-orientation techniques were found to be ineffective for most buried geophone data of both experiments.
- Mode leakage contributed to poorer data quality in processed sections from buried geophones than surface geophones. Other contributing factors were inconsistent geophone coupling and lower reflection amplitudes.
- Vertical interval *P*-wave velocities of the top 18m of the Chin Coulee near-surface layer averaged 640m/s, which is about two-thirds the velocity of the Blackfoot III area, for the western two-thirds of the receiver line. Similar observations were made for other intervals. This is probably due to different near-surface composition between the experiment locations, as the Chin Coulee near surface consisted of thick (>50m) recessional moraine tills (Westgate, 1963)

whereas the Blackfoot III receiver line was located in thinner (5-10m) glaciolacustrine sediments (Geiger, 1967; Shetsen, 1987).

- *P*-wave interval velocities indicate a thinning of the near-surface layer at the eastern third of the Blackfoot line, which corresponds to an increase in surface elevations.
- Near-surface *S*-wave interval velocities of the Blackfoot area are about 80% the values of the Chin Coulee area, resulting in interval  $V_p/V_s$  of Blackfoot being almost twice those of Chin Coulee. Differing near-surface composition between the two locations is the most likely explanation for these results.
- Both locations show a sharp increase in *P*-wave velocity at 10-12m depth that probably represents the water table. The *S*-wave velocity does not change greatly at the water table, resulting in very high  $V_p/V_s$  below the water table at both sites.
- Measurements of similarity between the Blackfoot III sections show that random noise level is the chief determinant in the absolute similarity of buried geophone processed sections. Relative similarity of the sections is controlled primarily by the relative depth of the receiver lines and secondarily by their absolute depth. This relation is stronger for the *P-P* sections than the *P-S* sections, probably due to the high random noise levels in the latter. Sections from similar geophone depths tend to be similar as they may have a similar frequency notching pattern. Shallower data has higher raw reflection amplitude, and therefore higher signal-to-incoherent noise levels. This may cause shallower data to be more similar than deeper data.
- Wavelet interference simulations indicate that more receiver notches will occur in lower-velocity media with smaller velocity gradients. The frequency spectra of data from deeper geophones would contain more notches than data from shallower geophones. As predicted, the *P-S* data contained more receiver notches than the *P-P* data. Most vertical channel receiver gathers did not contain clear examples of receiver notches, probably due to random noise and overprinting by notches from other causes.

- Wavelet interference models predicted that amplitudes decrease to some minimum value at depth (proportional to average velocity and gradient) and then increase gradually. This was not observed in the real data. The  $I(z)$  impedance model predicted an overall decrease of reflection amplitude with depth, which matched the real data strongly. This indicates that the near surface naturally amplifies reflections, as a result of its sharp impedance gradient, resulting in higher average absolute amplitudes for shallower geophones.
- On the Blackfoot III  $P$ - $P$  sections, the Glauconite channel appears as a high-amplitude trough surrounded by two peaks. Off-channel, the trough broadens out, decreases in amplitude, and the peaks turn into doublets. The channel is also a broad trough on the  $P$ - $S$  section that narrows slightly off-channel, making its interpretation more ambiguous than the  $P$ - $P$  interpretation.
- It is still not known where or how the converted wave becomes attenuated between bedrock and 18m below surface. This issue may be resolved with a shallow, multi-level VSP survey through the top 100 meters or so of the near surface. VSP surveys allow for more consistent coupling and greater control over geophone leveling and alignment than is possible for buried geophones. This shallow VSP survey could be done as an inexpensive add-on to a conventional, deep VSP survey.
- To study receiver notches further, the  $V(z)$  model should be modified to more closely match the true near surface. For  $P$ -waves, the velocities would increase in two large, discrete steps, representing the water table and the top of the bedrock. There would be only one step for the  $S$ -wave velocity as it is relatively unaffected by the presence of the water table. Velocities at intermediate locations would have a gradual, linear taper.
- It is recommended that the near-surface impedance  $I(z)$  model be extended to an  $I(x,z)$  model. Different impedance gradients between plausible near-surface materials were found to cause variations in reflection amplitude of over a factor of two. Customarily, differences in absolute reflection amplitude between

different geophones in a seismic survey are usually ascribed to “receiver response” and “geophone coupling” (e.g. Sheriff, 1975). They may in fact be partly due to the near-surface impedance gradient, and this should be investigated further.

## CHAPTER 7

### REFERENCES

- Alford, R. M., 1986. Shear data in the presence of azimuthal anisotropy: Dilley, Texas. Society of Exploration Geophysicists 56<sup>th</sup> Annual General Meeting, Expanded Abstracts **86**, Session:S9.6.
- Cary, P.W., and Eaton, D.W.D, 1993. A simple method for resolving large converted-wave (*P-SV*) statics. *Geophysics* **58**, p. 429-433.
- DiSiena, J.P., Gaiser, J.E., and Corrigan, D., 1984. Horizontal components and shear wave analysis of three-component VSP data. In *Vertical Seismic Profiling, Part B: Advanced Concepts*. Toksöz and Stewart (eds.), Geophysical Press, p. 177-188.
- Dufour, J., Squires, J., Edmunds, A, and Shook, I, 1998. Integrated geological and geophysical interpretation of the Blackfoot area, Southern Alberta. Canadian Society of Exploration Geophysicists Annual General Meeting, Technical Abstracts, p. 234-236.
- Fromm, G., Krey, T., and Wiest, B., 1985. Static and dynamic corrections; in Dohr, G., Ed., *Seismic Shear Waves: Handbook of Geophysical Exploration 15a*, Geophysical Press, 191-225.
- Gallant, E.V., Stewart, R.R., Bertram, M.B., and Lawton, D.C., 1995. Acquisition of the Blackfoot broad-band seismic survey. CREWES Research Report **7**, Ch. 36.
- Geiger, K.W., 1967. Bedrock topography of the Gleichen map-area, Alberta. Research Council of Alberta map 67-2A.
- Geis, W.T., Stewart, R.R., Jones, M.J., and Katopodis, P.E., 1990. Processing, correlating, and interpreting converted shear-waves from borehole data in southern Alberta: *Geophysics*, **55**, 660-669.

- Houghton, H.M., 1940. Change of reflection amplitude and character with geophone depth: *Geophysics* **5**, 169-175.
- Kudo, K., and Shima, E., 1970. Attenuation of shear waves in soil. *Bulletin of the Earthquake Research Institute* **48**, p. 145-148.
- Lawton, D.C., 1990. A 9-component refraction seismic experiment: *Canadian Journal of Exploration Geophysics*, **26**, 7-16.
- Lawton, D.C. and Harrison, M.P., 1992. A two-component reflection seismic survey, Springbank, Alberta. *Canadian Journal of Exploration Geophysics* **28**, p. 30-43.
- Lawton, D.C., and Howell, T.C., 1992. *P-P* and *P-SV* synthetic stacks. Society of Exploration Geophysicists 62<sup>st</sup> Annual General Meeting Technical Abstracts, p. 1344-1347.
- Larner, K., Chambers, R., Yand, M., Lynn, W. and Wai, W., 1983. Coherent noise in marine seismic data. *Geophysics* **48**, p. 854-886.
- Margrave, G.F., 1995. Estimates of the signal bandwidth of the Blackfoot broad-band data. *CREWES Research Report* **7**, Ch. 39.
- Margrave, G.F., and Foltinek, D.S., 1995. Synthetic *P-P* and *P-SV* cross sections. *CREWES Research Report* **7**, Ch. 5.
- Margrave, G.F., 1999. Seismic signal band estimation using f-x spectra. *Geophysics* **64**, No. 1 (in press).
- Miller, S.L.M., Aydemir, E.O., and Margrave, G.F., 1995. Preliminary interpretation of *P-P* and *P-S* seismic data from the Blackfoot broad-band survey. *CREWES Research Report* **7**, Ch. 42.
- Meunier, J., and Huguet, F., 1998. Céré-la-Ronde: A laboratory for time-lapse seismic monitoring in the Paris Basin. *The Leading Edge*, October 1998, p. 1388-1394.

- Porter-Hirsche, J. and Hirsche, K., 1998. Repeatability study of land data acquisition and processing for time lapse seismic. Society of Exploration Geophysicists 68<sup>th</sup> Annual General Meeting Technical Abstracts, p. 9-11.
- Pullin, N., Matthews, L., and Hirsche, K., 1987. Techniques applied to obtain very high resolution 3-D seismic imaging at an Athabasca tar sands thermal pilot. The Leading Edge, December 1987, p. 10-15.
- Rice, J.A., Krohn, C.E., and Houston, L.M., 1991. Shallow near-surface effects on seismic waves. Society of Exploration Geophysicists 61<sup>st</sup> Annual General Meeting Technical Abstracts, p. 747-749.
- Sheriff, R.E., 1975. Factors affecting seismic amplitudes. Geophysical Prospecting **23**, p. 125-138.
- Sheriff, R.E. and Geldart, L.P., 1995. *Exploration Seismology*, 2<sup>nd</sup> ed. Cambridge University Press, Cambridge.
- Shetsen, I., 1987. Quaternary geology, southern Alberta. Alberta Research Council Map, Scale 1:500 000.
- Simin, V., Harrison, M.P., and Lorentz, G.A., 1996. Processing the Blackfoot 3C-3D seismic survey. CREWES Research Report **8**, Ch. 39.
- Stewart, R.R., Huddleston, P.D., and Kan, T.K., 1984. Seismic versus sonic velocities: A vertical seismic profiling study. Geophysics **49**, p. 1153-1168.
- Toksöz, M.N, Johnston, D.H., and Timur, A., 1979. Attenuation of seismic waves in dry and saturated rocks: I. Laboratory measurements. Geophysics, **44**, 681-690.
- Westgate, J.A., 1963. Surficial geology of Foremost-Cypress Hills, 1:250000, Research Council of Alberta Bulletin 22.
- Wood, J.M., and Hopkins, J.C., 1992. Traps associated with paleovalleys and interfluves in an unconformity bounded sequence: Lower Cretaceous Glauconitic member,

southern Alberta, Canada. The American Association of Petroleum Geologists Bulletin, **76**, No. 6, 904-926.

Yang, Y.C.G., Lawton, D.C., Stewart, R.R., Miller, S.L.M., Potter, C.C., and Simin, V.  
1996. Interpretation and analysis of the Blackfoot 3C-3D seismic survey.  
CREWES Research Report **8**, Ch. 46.

Zhang, Q., San, Z., Brown, R.J. and Stewart, R.R., 1994. VSP interpretation from Joffre, Alberta. CREWES Research Report **6**, Ch. 33.